Nanoscale surface topographies for structural colors

Clausen, Jeppe Sandvik; Kristensen, Anders; Mortensen, N. Asger

Publication date:
2014

Document Version
Peer reviewed version

DTU Fotonik
Department of Photonics Engineering

Technical University
of Denmark

PhD thesis

Nanoscale surface topographies for structural colors

Jeppe Sandvik Clausen

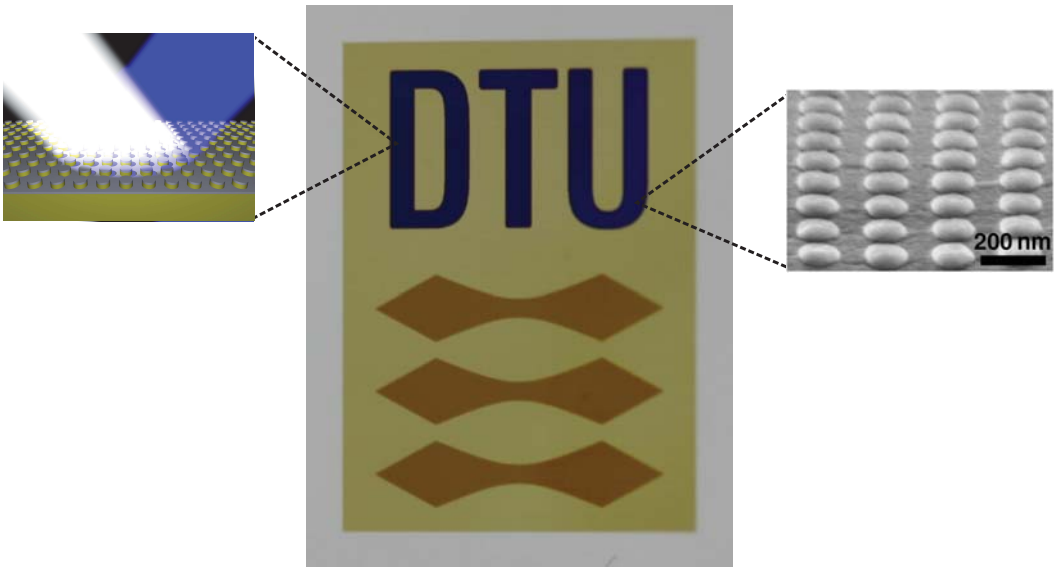

Supervisors:
Professor N. Asger Mortensen, DTU Fotonik
Professor Anders Kristensen, DTU Nanotech

July 31st, 2014

Preface

This thesis has been written as part of the requirements for obtaining the PhD degree from the Technical Universiy of Denmark (DTU). The work has been carried out in the Structured Electromagnetic Materials group (SEM) at DTU Fotonik under the NanoPlast project, which is funded by the Danish National Advanced Technology Foundation. Part of the work has been funded by the European Commission via the FP7MMP Integrated project PLAST4FUTURE. Nanofabrication has been performed in the cleanroom facilities of DTU Danchip and the optical characterization has been carried out in the laboratories of the Optofluidics group at DTU Nanotech.

The PhD project has been supervised by Prof. N. Asger Mortensen, who I would like to thank for his encouragements and guidance during the project. I have learned a lot about academic work by working within a group performing such high level research. The project has been co-supervised by Prof. Anders Kristensen, who I would also like to thank for his supervision and help.

I would like to thank the colleagues within the NanoPlast project, especially fellow PhD students Alexander B. Christiansen and Emil Højlund-Nielsen with whom I have had many interesting discussions on the details of the project. Also great thanks to the industrial partners, who have pushed for results and challenged our ideas. Also for the interesting visits at the industrial facilities, which have given a valuable input on the challenges of large-scale production. Thanks to Prof. Ole Sigmund and the members of his group, who were also in the WP2 work package of NanoPlast.

Great thanks to the SEM group, especially my office mates Søren Raza, Thomas Christensen and Xiaolong Zhu for creating a great work environment and for dealing with all my questions learning about plasmonics and other topics within optics. Also to Nicolas Stenger for the many discussions over lunch.

Thanks to the members of the Optofluidics group, who have shared their expertise within nanofabrication and optical characterization and to the Danchip staff for always being helpful in the cleanroom.

I would also like to thank Prof. Uriel Levy and Meir Grajower for hosting me during my visit at the Hebrew University of Jerusalem. Also thanks to Hesham Taha, Nanonics for assisting during NSOM measurements. Thanks to The Danish Agency for Science, Technology and Innovation foundation for funding this visit.

Finally, thanks to my wife Cecilie, who have supported me throughout my studies and with whom I can't wait to begin the next chapter.

Jeppe Sandvik Clausen
Lyngby July 31st, 2014

Abstract

The thesis describes and demonstrates the possibilities for utilization of structural colors in mass fabricated plastic products as replacement for or in combination with pigments and inks. The motivation is the possible advantages related to re-cycling and re-use of plastic by limiting the number of materials in a given plastic part. Also, the reduction of process steps and materials leads to a reduction of the fabrication costs. In the thesis only surfaces, which may be fabricated using replication based methods, such as injection molding, are considered.

Nanostructures with sizes comparable to the wavelength of visible light are theoretically and experimentally investigated. These structures interact with light such that the appearance of a surface is modified.

It is shown how sufficiently small tapered nanostructures lead to an anti-reflective effect were the reflection of light at the air-polymer interface is suppressed. This improves the ability to see through a clear plastic in the presence of specular reflection. The tapered nanostructures are also utilized to enhance the chroma of pigmented polymers.

Larger tapered structures fabricated in a similar manor are shown to work as color filters. Through an experimental study is the color of the transmitted light linked directly to the random topography of the surface by use of diffraction theory.

The color effects from periodic structures and how these might be employed to create bright colors are investigated. This is done both for opaque samples and transparent foils. In the latter case the specific sample geometry may be utilized to create a zero order reflectance, which is significantly higher than what may be achieved by a single interface.

When the design limitations are relaxed and a small amount of post processing of the nanostructured plastic is done, more possibilities arise. A surface utilizing the concept of localized surface plasmon resonances (LSPR) is produced, when an ultra-thin layer of aluminum is deposited on a suitable nanostructured plastic surface.

The choice of aluminum as active plasmonic material is based on cost and abundance aspects, but also advantages within robustness and optical properties compared to other metals commonly used for plasmonic applications.

Hybridization theory is used to describe the behavior of the surface and a parameter space is identified where it by proper choice of vertical geometrical parameters is possible to create a plurality of bright colors by varying the lateral parameters only.

It is shown how diffraction effects and excitation of surface plasmon polaritons constitute the main limitations on the angular sensitivity of the surface.

Resume

Afhandlingen beskriver og demonstrerer mulighederne for udnyttelse af strukturelle farver i massefabrikerede plastikprodukter som erstatning for, eller i kombination med, pigmenter og maling. Motivationen er de mulige fordele relateret til genanvendelse og genbrug af plastik, der opnås ved at begrænse antallet af materialer i et givet plastikprodukt. Derudover medfører reduktionen af procestrin og materialer en reduktion i fabrikationsomkostningerne. I afhandlingen beskrives kun overflader der kan fremstilles ved hjælp replikationsbaserede metoder såsom sprøjtestøbning. Nanostrukturer med størrelser der er sammenlignelige med bølgelængden af det synlige lys er teoretisk og eksperimentelt undersøgt. Disse strukturer interagerer med lyset så overfladens udseende ændres.

Det demonstreres hvorledes tilpas små tilspidsede nanostrukturer fører til en antireflektiv effekt, hvor reflektionen fra luft-polymer overfladen undertrykkes. Dette forbedrer evnen til at se gennem klar plastik i tilfælde af overfladereflektioner. Disse strukturer er også blevet brugt til at forøge chroma af pigmenterede polymerer. Det vises hvorledes større strukturer fabrikeret med en tilsvarende metode kan fungere som farvefiltre. Gennem et eksperimentelt studie og ved brug af diffraktionsteori vises det hvordan farven af det transmitterede lys kan relateres direkte til den tilfældige overfladestruktur.

Det er undersøgt hvordan periodiske strukturer kan anvendes så klare farver opstår. Dette gælder både for ugennemsigtige prøver og klare folier. For klare folier vises det hvordan den specifikke geometri fører til betydelig forøgelse af det spekulært reflekterede lys sammenlignet med en enkelt overflade.

Når designbegrænsningerne ophæves og en smule efterbehandling tillades opstår der nye muligheder. En overflade der udnytter lokaliserede overfladeplasmoner er blevet fabrikeret ved hjælp af pådampning af et ultra tyndt lag aluminum på en nanostruktureret overflade.

Valget af aluminium som plasmonisk materiale skyldes lave omkostninger og at det forekommer i store mængder. Derudover er der også fordele i forhold til robusthed optiske egenskaber sammenlignet med andre relevante metaller der benyttes til plasmoniske anvendelser.

Hybridiseringsteori benyttes til at beskrive hvordan overfladen opfører sig og et parameterrum identificeres, hvor man med det rigtige valg er vertikale parametre kan skabe et væld af farver ved kun at variere de horisontale parametre. Det vises hvorledes diffraktionseffekter og kobling til propagerende overfladeplasmoner udgør hovedbegræsningerne i forhold til overfladens vinkelafhængighed.

List of publications

The following has been published during the PhD work.

Journal papers included in this thesis

Paper A — J. Clausen, A.B. Christiansen, J. Garnaes, N.A. Mortensen, and A. Kristensen, "Color effects from scattering on random surfaces structures in dielectrics", *Opt. Express* **20**, 4376 (2012).

Paper B — A. B. Christiansen, J. Clausen, N.A. Mortensen, and A. Kristensen, "Minimizing scattering from antireflective surfaces replicated from low-aspect-ratio black silicon", *Appl. Phys. Lett.* **101**, 131902 (2012).

Paper C — J.S. Clausen, A.B. Christiansen, A. Kristensen, and N.A. Mortensen, "Enhancing the chroma of pigmented polymers using antireflective surface structures", *Appl. Optics* **52**, 7832 (2013).

Paper D — J.S. Clausen, E. Højlund-Nielsen, A.B. Christiansen, S. Yaszdi, M. Grajower, H. Taha, U. Levy, A. Kristensen, and N.A. Mortensen, "Plasmonic metasurfaces for coloration of plastic consumer products", *Nano Lett.* **14**, in press (2014)

Conference proceedings

Paper E — A.B. Christiansen, E. Højlund-Nielsen, J. Clausen, G.P. Caringal, N.A. Mortensen, and A. Kristensen, "Imprinted and injection moulded nano structured optical surfaces", *Proc. SPIE* **8818**, 881803 (2013).

Other journal papers

A. Christiansen, J.S. Clausen, N.A. Mortensen, and A. Kristensen, "Injection molding antireflective nanostructures", *Microelectronic Eng.* **121**, 47 (2014).

Conference and workshop contributions

J. Clausen, A.B. Cristiansen, E. Højlund-Nielsen, N.A. Mortensen, and A. Kristensen. "Large area structural color decorations", poster presented at Micro and Nano Engineering conference (MNE) 2011, Berlin.

J. Clausen, A.B. Cristiansen, J. Garnaes, N.A. Mortensen, and A. Kristensen. "Large area color effects in polymer replication of black silicon", Invited talk at Acapoly workshop, Lausanne 2012.

J. Clausen, A.B. Cristiansen, N.A. Mortensen, and A. Kristensen. "Chroma enhancement of pigmented polymers by use of anti-reflection surface structures", Oral presentation at Polymer Replication at the Nanoscale conference (PRN) 2014, Copenhagen.

Patent applications

J.S. Clausen, N.A. Mortensen, A. Kristensen, E. Højlund- Nielsen, A. B. Christiansen, and C. Jeppesen , "Confidential title", EP Patent Appl. No. 13182666.1. Not published yet.

Contents

Chapter 1

Introduction

1.1 Background

Since the development of industrial scale synthesis of polymers in the 1930s and the emerging of very useful engineering plastics in the following decades, these materials have taken up an increasingly larger part of our surroundings and daily life [1]. With desirable properties such as low cost, low weight, high strength, and durability [2] plastics have for many applications replaced metals, wood, glass and fabric as preferred material within construction, toys, electronic packaging, cars and a large number of other consumer industries.

With the large impact on modern society follows a number of concerns. About 8% of the worlds production of oil and gas goes into the production of various types of polymers. Here one half is raw materials for the synthesis and the other half is for the energy going into the fabrication processes [3]. Thereby the production of plastic contributes to the depletion of non-renewable resources and it is evident how dependent the plastic industries are on access to cheap and plenty oil and gas deliveries. A possible future shortage on these resources would be very costly and problematic for manufacturers of plastic products.

Another major concern is the plastic debris accumulating in the nature. Due to its durability plastic will survive for centuries in oceans and soil either as macroscopic objects and as microscopic fragments and the full impact on wild life is still to be determined [4]. To solve this problem the re-collection and re-cycling of plastic must be improved and a switch to biodegradable plastics for short lifetime products such as packaging would be beneficial.

The project NanoPlast, under which this PhD work has been carried out, have been initiated to address some of these issues. The overall goal has been to develop and demonstrate value-adding functionalities for use in plastic products, where the properties arise from topographical effects rather than chemical additives. Such effects are e.g. anti-stiction properties for the inside of food containers or effects related to the appearance of the plastic objects, the latter being the topic of this thesis.

By limiting the number of additives the perspectives for re-use and re-cycling are better. For the specific case of coloration, limitations on pigments and inks used in the fabrication of plastic products will ease the integration in new products after re-cycling. The ideal case would be the situation where the clean polymer, when shaped into a product e.g. as packaging adapts certain appearance characteristics

due to the surface topography. This could be a company logo printed in the surface or other decorations. When re-cycled, the clean polymer is re-shaped into a new product which may adapt completely new appearance properties by employing a new type of surface topography and so on. As will be evident from this thesis the structural color effects obtainable with pure plastic is limited and the re-cycling example just described will only be relevant for certain specific applications. Besides describing some of the possible effects which can be made purely in plastic there will also be focus on how little modification of the pure plastic is necessary to create the desired optical effects such as angle insensitive coloration.

To illustrate what the structural effects should replace and be incorporated in the following is a short description of the plastic production and decoration technologies of today's industry.

The production technology chosen in NanoPlast is injection molding. This is the most wide spread technique to produce free form plastic objects in large numbers. The method is based on a steel mold comprising a cavity in the shape of the desired plastic part. Liquid polymer is injected into the cavity under high temperature and pressure and after a certain cooling time the mold is opened and the plastic part can be removed. The process is then repeated and with cycle times on the order of seconds large quantities of identical plastic parts can be fabricated.

For colored objects the injected polymer is typically colored with pigments making the final part opaque reflecting light with the desired color diffusely. Surface decoration are printed onto the surface of the part with ink using printing methods such as Pad Printing [5].

The idea of NanoPlast is to integrate the functional nanostructures in the mold thereby enabling a transfer of the desired surface characteristics e.g. decoration in the injection molding step. When the plastic part leaves the mold it is already functionalized and the subsequent printing step can be avoided. This saves a production step and there is no mixing of colorants. The basic idea of NanoPlast is build around a concept of replication-based nano-structuring where possibly expensive nanolithography only has to be carried out once, namely in the production of the mold. This is advantageous since detailed nano-structuring based on for example Electron Beam Lithography (EBL) is very expensive and time consuming and by no means compatible with large volume production. Other replication based fabrication processes which are relevant for this project are embossing, nano imprint lithography,

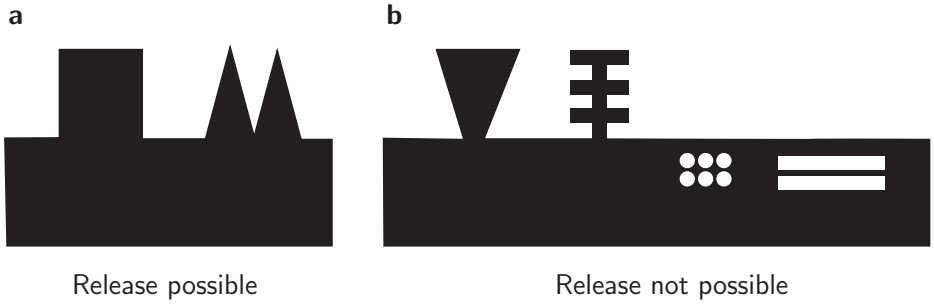

Figure 1.1: Replication constraint. a) Examples of allowed structure geometries with vertical or positive sloped side walls. **b)** Examples of disallowed geometries such as negative slopes, overhang and air filled voids.

and roll-2-roll replication, the latter being very useful for large area production of plastic foils. Common to all the replication-based fabrication techniques is the demand for structures which allow for release after the formation of the desired surface structures. This puts some quite restrictive limitations on allowed geometries. No structures are allowed to have a negative slope and air-filled cavities are also disallowed. This constraint on geometry will be referred to as the replication constraint in the thesis. Figure 1.1 show some examples of allowed and disallowed structure geometries. The consequences of this replication constraint will be described in the thesis.

1.2 Structural colors and anti-reflective effects

The engineering of surface topography with the goal of modifying the reflectance properties to achieve either colors or very little reflection have historically found inspiration in the wide range of structural optical effects found in nature. Since the invention of the electron microscope the topographical origin of some of natures bright colors have become evident. Below follows a short description of some of these naturally occurring coloration techniques, which have evolved in nature for the purpose of protection against predators, appeal to the opposite sex, and communication with other individuals [6].

The eye of a wide range of moth and some butterfly species are build up with a lens structure as illustrated in Fig. 1.2a, where one of the faceted lenses is shown. On the surface of these lenses a dense pattern of rounded cones is present, which has an anti-reflective effect. This property was discovered by Bernhard in 1967 [9] and latar reproduced using interference lithography [10, 11]. The effect is discussed in Section 3.1.4. The moth utilize the AR effect to be less visible to predators at night as reflections from the eyes would give away its position. Besides use for appearance purposes, this effect has for example been utilized within photovoltaics to improve efficiencies of solar cells [12, 13] and light emitting diodes [14].

The metallic green color of the buprestid beetle is due to a layered structure in the surface of the scales [6]. The alternating layers of different materials, shown in Fig. 1.2b, lead to multilayer reflectance phenomena, where the reflectance of certain wavelengths are highly enhanced over others. The conditions for high reflectance is a phase shift of 2π for the light in a round-trip of the unit cell For the particular structure this is the case for wavelengths in the region around 500 nm leading to the green color.

In many animals colors based on pigments are combined with iridescent effects arising from structures. This is the case for the nitidulidae beetle, where the scales are colored by a brown-red pigment, while colored orders appear due to 2D periodic modulations of the surface, as seen in Fig. 1.2c.

One of the most well known examples of structural color is within the family of Morpho butterflies. In Fig. 1.2d a Morpho Didius is seen with it blue color, which arise due to the very complex scale structure seen in the SEM images. On the scales are parallel ridges, which have a layered geometry in the vertical direction. As for the buprestid beetle this gives rise to multilayer reflectance, but in this case the ridges are individually shifted in height so an extra diffraction effect allows for observation of the color in a large angle interval [15].

It is evident that of the presented examples are only the ones shown in Fig. 1.2a and Fig. 1.2c compatible with the replication constraint of Fig. 1.1 and it is therefore

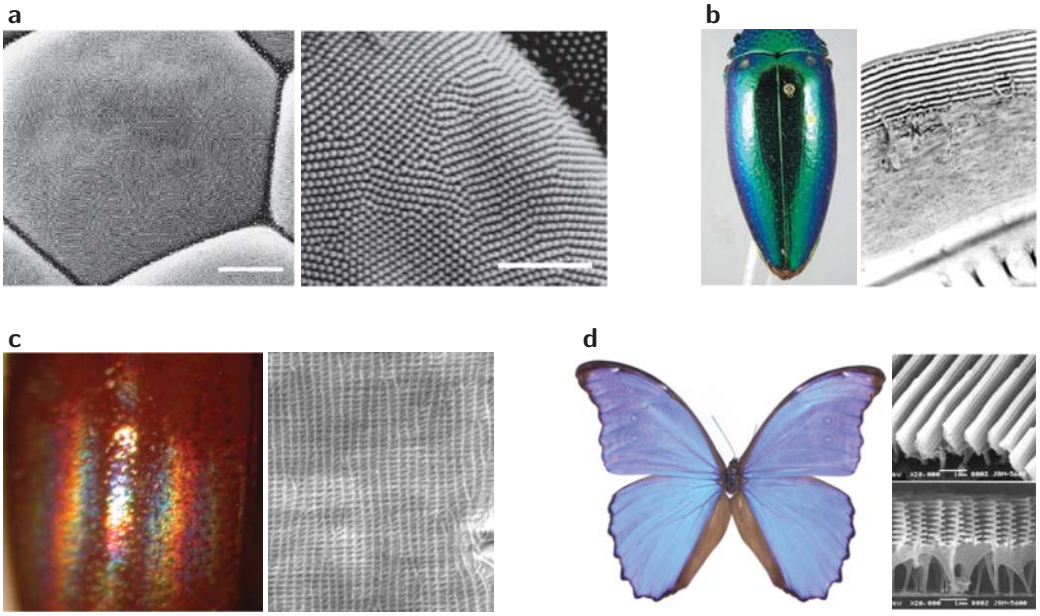

Figure 1.2: Examples from nature. a) Eye of a nympholid butterfly at two different zooms. One of the lenses covered with AR structure is revealed in SEM. The scalebars are 5 µm and 2 µm respectively. From Stavenga *et al.* [7]. **b)** The buprestid beetle which have a very metallic green appearance which arise from the layered structure in the surface as seen from the transmission electron microscope image. From Seago *et al.* [6]. **c)** Nitidulidae beetle, which has brown base color, but with diffraction gratings in the surface. This gives rise to iridescent color reflections from the scales. From Seago *et al.* [6]. **d)** Morpho Didius with its blue color due to the layered wing structure. The wings consist of scales which have these structures in the surface. From Kinoshita *et al.* [8].

not possible to copy all the effects directly.

A very different type of what could be described as structural color is found in some ancient glass for use as decorations. Two examples are shown in Fig.1.3. One is the Lycurgus cup from the fourth century A.D. displayed at the British museum [16, 17], which is a glass cup displaying remarkable appearance behavior. In the reflected scattered light it appears green, while in the direct transmitted light it looks red. This behavior is due to sub-100 nm particles made of gold-silver alloys, which are contained in the glass and which most likely were formed in the heat treatment during the forming of the glass. In ancient time the physical behavior was not understood, but it has surely been discovered how certain types of glass showed these properties, when treated in a certain way. The other example is window decorations in the church of Sainte Chapelle in Paris, where some of the colors are due to metallic nanoparticles. Upon sunset the colors change due to changing illumination angle, while other parts stained using traditional methods stay constant [18]. This makes the image evolve as the sun moves. The physical explanation of these effects are explained in Sec. 4.1.2.

Figure 1.3: Colors from ancient glass with metallic nanoparticles. Lycurgus cup displayed at the British museum. The colors arise due to metallic nanoparticles in the glass. Pictures from `www.britishmuseum.org`.

1.3 Quantifying color appearance

Already at this point it has been demonstrated that it is not possible to simply attribute a particular color to an object without taking into account the circumstance under which the object is seen, as with the diffraction grating of the nitidulidae beetle and the color difference depending on illumination with the Lycurgus cup. In addition to this the descriptions, blue or green, are not unique and may be used to describe many different shades.

In order for humans to see an object having a certain color three things must be present: A light source, the colored object and the human visual system. The light source could for example be the sun, which emits light at wavelengths through out the visible spectrum from just below 400 nm to around 750 nm. Radiation in other wavelengths regimes is also emitted, but it is not important in this context. The light interacts with the colored object and reflected, transmitted or absorbed depending on the mechanisms involved. This gives rise to light in the direction of the observer, which in this case is the human eye. Here it is focused on the back of the eye where it is detected by dedicated receptor cells, denoted rods and cones due to their shape. The rods detect light intensity, while the three different types of cones are sensitive in different parts of the spectrum allowing for color vision [19].

In order to isolate the object properties from the full system a color coordinate system has been developed, where standard illuminants and standard observers are used. The standard illuminants, $S(\lambda)$ simulate typical lighting conditions. In this work the D65 standard has been used in color calculations, which simulates middle daylight [19].

The standard observers have been defined from a series of color matching experiments, where the color of monocromatic light was compared with a mix of three primary colors by test persons. In this way it was possible to extract the weight-function of the primaries, the color matching functions $\bar{x}(\lambda)$, $\bar{y}(\lambda)$, and $\bar{z}(\lambda)$. There exist two main set of standard observers based on different experiments, the 2 degrees CIE 1931 observer and the 10 degrees CIE 1964 observer. The angles indicate the full angle of the light cones used in the experiments. This influences which receptor cells are activated and therefore also the result. In this work the 10

degree observer is used in Sec. 3.3.1, while the 2 degree observer has been used for all other purposes. Which one to choose depends on the cone angles with which the light is expected to reach the eye.

The CIE tristrimulus values may now be calculated as [19]

$$X = k \sum_i S(\lambda_i) R(\lambda_i) \bar{x}(\lambda_i) \Delta\lambda \tag{1.1}$$

$$Y = k \sum_i S(\lambda_i) R(\lambda_i) \bar{y}(\lambda_i) \Delta\lambda \tag{1.2}$$

$$Z = k \sum_i S(\lambda_i) R(\lambda_i) \bar{z}(\lambda_i) \Delta\lambda, \tag{1.3}$$

where the reflectance, R, is sampled at wavelengths λ_i with a spacing of $\Delta\lambda$. For cases of transmitted light R is replace by the transmittance. The constant k is determined such that Y is 100 for the illuminant itself. The color matching function, $\bar{y}(\lambda)$, corresponds well to the light sensitivity of the human eye and the value Y is therefore often referred to as the lightness of a color. Often the color system xyY is used, where x and y are chromaticity coordinates given by

$$x = \frac{X}{X + Y + Z} \tag{1.4}$$

$$y = \frac{Y}{X + Y + Z}. \tag{1.5}$$

In the xyY system the values of x and y contain the information of the chroma and hue, while the Y gives the lightness. This system may be represented in the chromaticity diagram shown in Fig. 1.4a, where the colors observable by the human eye is represented in the plot. The arc in the plot represent the monochromatic colors, while all other colors are composed of many wavelengths.

Another system which is often used is the CIELAB system introduced in 1976, where the color values L^*, a^*, and b^* are used. These are given from the XYZ-values and the empirical formulas for calculating these values may be found elsewhere [19]. In this system is the lightness, a^* is the red-to-green contribution and b^* is the yellow-to-blue contribution. The a^*b^*-plane for constant L^* is seen in Fig. 1.4b. In this system it is possible to use cylindrical coordinates, which describe more general properties of the colors, namely the chroma C^*_{ab} and the hue angle h^*_{ab}. The chroma is the distance to the center in the a^*b^*-plane and indicates how pure or clear a color is. The hue angle is the angle from the positive a^*-axis and gives the hue. The lightness L^* is still used to indicate the lightness.

When comparing colors in the CIELAB system the total color difference ΔE^*_{ab} is simply given by the geometrical distance in the space

$$\Delta E^*_{ab} = \sqrt{(\Delta L^*)^2 + (\Delta a^*)^2 + (\Delta b^*)^2} = \sqrt{(\Delta L^*)^2 + (\Delta C^*_{ab})^2 + (\Delta H^*_{ab})^2}, \tag{1.6}$$

where all the difference in coordinates are given by subtraction of the given coordinate of the two colors, except ΔH^*_{ab} which is calculated from the difference in hue angle and the chroma coordinates. A color difference of approximately 2.3 corresponds to a just noticeable difference, however this varies across the color space, which is not visually uniform [20].

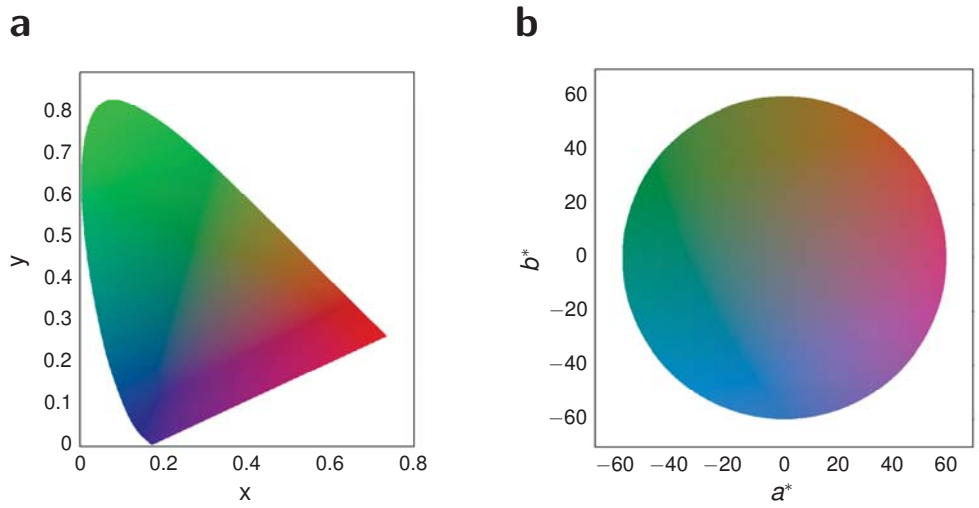

Figure 1.4: Chromaticity diagrams. a) The CIE 1931 chromaticity coordinates xy with constant Y-coordinate. **b)** CIELAB chromaticity coordinates with constant lightness, L^*. Both diagrams are drawn with the build-in color convertion tool in MATLAB via conversion to sRGB.

1.4 Thesis outline

The thesis is structured in chapters of different topics:

Chapter 2

A description of the experimental methods used throughout the work. Both nanofabrication techniques and optical characterization are described.

Chapter 3

The chapter contains the work done on structural colors in plastic surfaces. After an introduction to the relevant physics are examples of the fabricated structural colors within the limits of the replication criterion demonstrated.

Chapter 4

The design criteria are relaxed and it is investigated what may be achieved with a polymer surface on which a thin layer of metal is deposited. The new possibilities provided by optical properties of metals are described followed by an introduction to the proposed design principle. Numerical simulations and experimental work are shown.

Chapter 5

The main conclusions of the work.

Chapter 2

Experimental techniques

Prototyping and experimental realization of the structural colors constitutes a major part of the work in this thesis. Many of the fabrication techniques which have been used for different applications are the same as well are the methods for optical characterization. This chapter introduces the techniques which have been used the most and will be referenced in the following chapters, when it comes to the specific structures and their optical effects. Some techniques, where the method is in very close relation to the results are omitted here and only explained in the relevant context. This is for example the case for the characterization using Near-Field Scanning Optical Microscope (NSOM).

2.1 Micro and nano fabrication

The basic premise of functional structured surfaces, which may be fabricated using replication methods has influenced the fabrication of the prototypes. All structures demonstrated here are based on the same general fabrication scheme. First a master mold has been fabricated in silicon, then this mold is used in one or more replications steps to produce the final dielectric surfaces.

The nanostructuring of the silicon master mold has been carried out using two main techniques: electron-beam lithography followed by dry etching or direct etching in silicon using random masking leading to random tapered structures.

2.1.1 Electron beam lithography and dry etch

In electron beam lithography (EBL) a focused electron beam is scanned across a resist coated sample in order to either cross link (negative resist) or cut (positive resist) the polymer chains of the resist. This allows for selective removal of the resist in the development process which follows. In this work positive zep520a resist (Zeon Chemicals L.P.) has been used. The process flow for mold fabrication using EBL followed by dry etching is shown in Fig. 2.1.

First the zep520a diluted 1:1 in anisole is spin-coated on bare silicon wafers. The resist thickness depends on the spinning speed. Thicknesses of 120-150 nm have been used in this work. The resist is baked for 2 minutes at 180 °C after the spin-coating to drive out the solvent. The samples are exposed in a JBX-9500FS vector scanning system (JEOL) using an acceleration voltage of 100 kV. After exposure areas which have been exposed to a sufficiently high electron dose are dissolved in the development

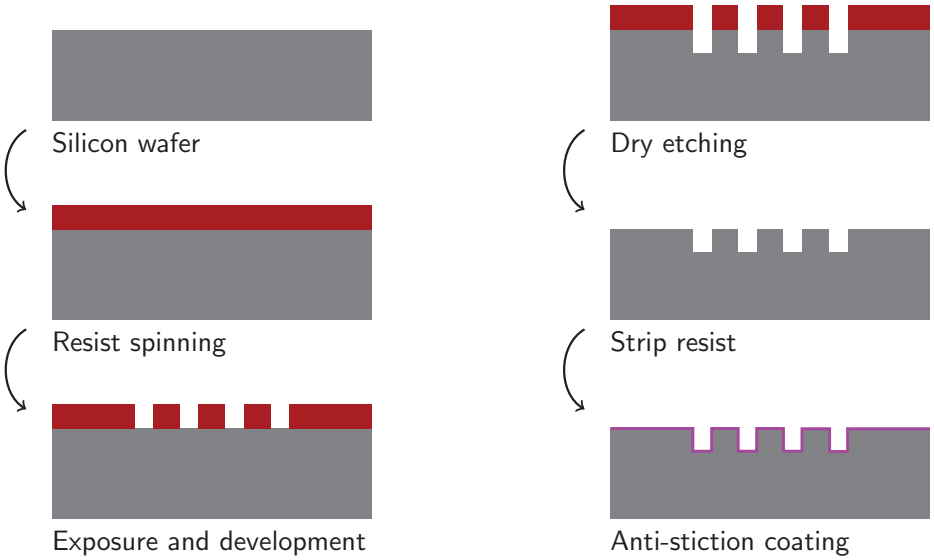

Figure 2.1: EBL process flow. The fabrication of molds using EBL starts from a bare silicon wafer which is coated with EBL resist followed by exposure and development. The pattern is transferred using dry etching before the resist is stripped. The final the mold is anti-stiction coated with FDTS.

process. This is done in ZED-N50 (Zeon Chemicals L.P.) for 2 minutes followed by rinsing in isopropyl alcohol (IPA) for 30 s and blow drying using nitrogen. The developed wafer is then etched to the desired thickness using a plasma etcher in an anisotropic process (detailed description below). After etch the resist is stripped with Microposit Remover 1165 (Shipley) for 15 minutes followed by rinse in IPA and blow drying. Finally the structured silicon wafer is anti-stiction coated with 1H,1H,2H,2H-perflourodecyltrichlorosilane (FDTS) using molecular vapor deposition (MVD 100, Applied Microstructures Inc.) to improve release in later replication steps.

In the positive EBL process it is chain scission, which leads to a lower molecular weight and therefore higher solubility in the developer compared to the unexposed areas. The electron dose needed to provide enough chain scission for the resist to be completely removed in the development step is denoted the clearing dose. Both electrons from the primary Gaussian shaped beam and backscattered electrons from exposure at nearby positions contribute. The traditional way of operating an EBL system is to place a number of overlapping shots next to each other with a pitch, g, significantly smaller than the feature size. This is illustrated in Fig. 2.2a. The delivered electron dose at each position, Q, is then adjusted such that the total dose (including backscattering) inside the structure is higher than the clearing dose and lower outside. Here, Q is denoted the nominal dose, which indicates that it is the dose which the machine is programmed to deliver assuming uniform electron distribution within each square of area g^2. The time the machine spends on each shot is

$$t_{shot} = \frac{Qg^2}{I}, \tag{2.1}$$

where I is the current. Current and shot pitch should be chosen such that $1/t < f_{max}$,

where f_{max} is the maximum scanning frequency at which the machines operates. For the JBX-9500FS this is 100 MHz. In the exposure process there are different contributions to the total time [21]. The first contribution is the beam time, t_{beam} which is the time it takes to deliver the desired dose. This can be calculated from the area of the structures, A, the current, I, and the nominal dose

$$t_{beam} = \frac{QA}{I}. \tag{2.2}$$

Often this contribution is considered the most important.

In addition to this, the machine use some time to move between each individual feature, a time which is on the order of micro seconds per movement for the machine. This contribution t_{move} is proportional to the number of elements, and is often negligible. However, for the applications demonstrated in this work where large areas of 2D gratings consisting of dense nanostructures t_{move} may easily exceed $3\,\mathrm{h/cm^2}$.

The written area is split into smaller writing fields, within which only the electron beam is scanned and the sample is held in fixed position. The maximum writing field area is $1 \times 1\,\mathrm{mm^2}$ for the used machine. Each main writing field is split into sub-writing fields ($4 \times 4\,\mu\mathrm{m^2}$ as default) where a sub deflector secures the precise and fast scanning. Every time a writing field is finished the stage has to move and this total stage movement time, t_{stage} is determined by how many fields are written. For standard EBL this is negligible.

The last contribution is calibration time, t_{cal}. Depending on the settings the beam is calibrated in certain time intervals during the exposure. This is needed to maintain stable conditions during the full exposure.

Adding up these contributions the writing time of a 2D periodic array of holes with period $\Lambda = 200\,\mathrm{nm}$ and a filling fraction $f = 0.20$ is approximately $10\,\mathrm{h/cm^2}$.

Another method which allows for much higher writing speed is used in order to write significant areas. The method, here denoted as fast EBL, utilizes the 2D Gaussian electron beam profile to create circular holes in a 2D periodic pattern [21, 22]. In this method the shot pitch is set to the grating period, Λ, and each hole is made by a single shot by the electron beam. This has several advantages which leads to improvement in writing speeds by orders of magnitude. First of all it allows

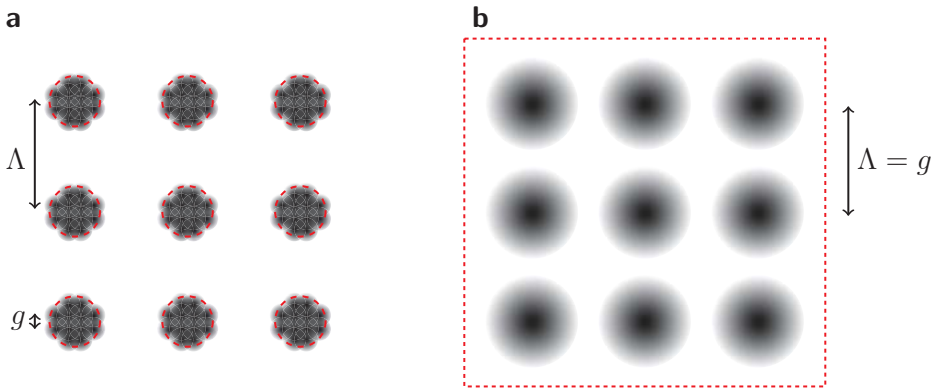

Figure 2.2: Illustration of conventional versus fast EBL. a) Conventional EBL where the shot pitch, g is much smaller than the feature size. **b)** Fast EBL where the shot pitch equals the period of the desired structure.

for a significantly higher current, since the charge delivered at each shot position is much higher than for conventional EBL which. Therefore one can increase the current without exceeding the maximum frequency of the scanners. Another reason is the fact that a square filled with nanostructures is simply drawn as a square in the layout and the movement time between individual structures is therefore effectively zero. This is illustrated by the red dashed line of Fig. 2.2b.

The method have some drawbacks which should be considered. It is only possible to create circular features due to the shape of the beam. Furthermore they must be arranged in a periodic pattern since it is the machines distribution of shots which leads to the position of the features. Here only quadratic patterns are used, but it is also possible to make for example hexagonal patterns. Due to the fact that a feature is defined from a single shot makes it very dependent on the quality of the electron beam. Any distortions in the beam is directly transferred to the feature. For this reason it has been seen that small writing fields are needed, since the quality of the beam is better in the center of a writing field. When using fast EBL writing fields with side lengths of 200 µm have been used. The method is very sensitive to degradation of the filament of the machines. A completely new sharp filament will produce a different spot than an older, one which have been rounded during use. This leads to challenges in the reproducibility when applying this method.

The dry etch for pattern transfer was carried out in a plasma asher (DRIE Pegasus, SPTS). The process was un-cycled and was based on SF_6 (38 sccm) and C_4H_8 (75 sccm) gases. The pressure was 4 mTorr. The coil power for plasma generation was 800 W, while the platen power was 40 W. The etch combines silicon etching using fluorine radicals with simultaneous passivisation of sidewall due to the C_4H_8 in order to achieve vertical side walls of the etched structures. The etch rate in the silicon was measured to be 168 nm/min for typical structures with a selectivity over the zep520a of approximately 2.5.

2.1.2 Black silicon formation

The formation of nanostructures on large areas without the use of EBL is attractive. Therefore other methods have been investigated. One of the methods is a dry etching technique known as the black silicon method [23, 24], where it is possible to create semi-random nanotexturing in the surface of a full silicon wafer using very little processing time. The process development of this type of etch was mainly carried out by another PhD student and the concept is therefore only briefly introduced.

The method is basically a normal dry etch as described above, where the balance between sidewall passivisation and silicon etching is shifted such that uneven textures in the surface are enlarged to form for example spikes. In the present work all black silicon etches are with a mixture of SF_6 and O_2 gases, and the passivisation formed on the sidewalls is $Si_xO_yF_z$.

The process starts by penetration of the native oxide present on the silicon surface. This oxide is not uniform and is removed unevenly. Depending on the plasma densities and the physical component of the etch this increasing roughness results in dense spikes, tapered protrusions with moderate slopes or other geometries.

As shown in Paper A and Paper B the resulting textures may possess very different optical properties.

Since the process is inherently unstable, very small changes in conditions lead to large changes in geometry. It is demanding to achieve the same structure all

over the wafer due to uneven loading near the wafer edges and other non-uniform parameters such as the temperature. The temperature influences the rate at which the passivation is removed and therefore how the structures look.

2.1.3 Replication techniques

After fabrication of a mold the next step is replication into plastic or for the purpose of demonstrators, materials which simulate the optical properties of plastic. Both thermal replication techniques as well as UV casting have been used and for both techniques both bulk samples and thin films on a glass carrier have been used. These different approaches are illustrated schematically in Fig. 2.3. In UV-replication techniques a liquid UV sensitive resin is used. In this work the organic-inorganic hybrid polymer Ormocomp (Microresist Gmbh) is used, which is within the category of Ormocers [25]. Upon illumination with UV-light the Ormocomp cures and becomes a transparent material with refractive index of 1.518 (@ 635 nm). This resembles the properties of the thermoplastics in the desired end-products well. The very liquid resin has a very good ability to replicate very small features with high accuracy, even without applied pressure. There is no solvent and the shrinkage is therefore minimal. In the case of the fabrication of bulk Ormocomp samples (Fig. 2.3a) the resin is poured onto the mold followed by placement of a dummy sheet of PMMA (1 mm) on top for creation of a flat backside. Spacers placed at the edges of the mold and the PMMA sheet may be used if a particular thickness of the final samples is desired. The sample is cured through the PMMA sheet and finally it is removed from mold and PMMA.

In a similar process it is possible to have the Ormocomp on a carrier glass substrate in order to secure flat and stiff samples (Fig. 2.3b). This is done by spin coating of the Ormocomp prior to imprinting. The Ormocomp is cured through the glass and adheres to the glass when the mold is removed.

The other main technique is thermal embossing. For the creation of bulk polymer samples a flat sample is placed in between the structured mold and a flat mold, typically an FDTS coated flat silicon wafer (Fig. 2.3c). In a parallel press or with a hydrostatic pressure is the stack heated to above the glass transition temperature (T_g) of the polymer and the pressure is applied. The polymer deform to the shape of the mold and after a specific amount of time, the temperature is lowered to below T_g, while maintaining the pressure. Finally the pressure is released and the stack is separated.

For the case of thermal imprinting in thinner film on a glass carrier the process is not much different. Here, however the thermoplast is first spin-coated from solution onto a glass wafer. In this work a 75K PMMA was disolved in anisol (25 wt%) and spin coated onto the glass wafers (Borofloat, Boro33), which were pre-baked to drive out water and thereby improved adhesion. The PMMA was spin coated at 2000 rpm for 60 s and baked for 5 minutes at 100 °C to drive out the solvent. This process resulted in 4 µm thick PMMA films. The imprinting process itself is similar to that of bulk samples.

Which technique is used is indicated in the individual sections.

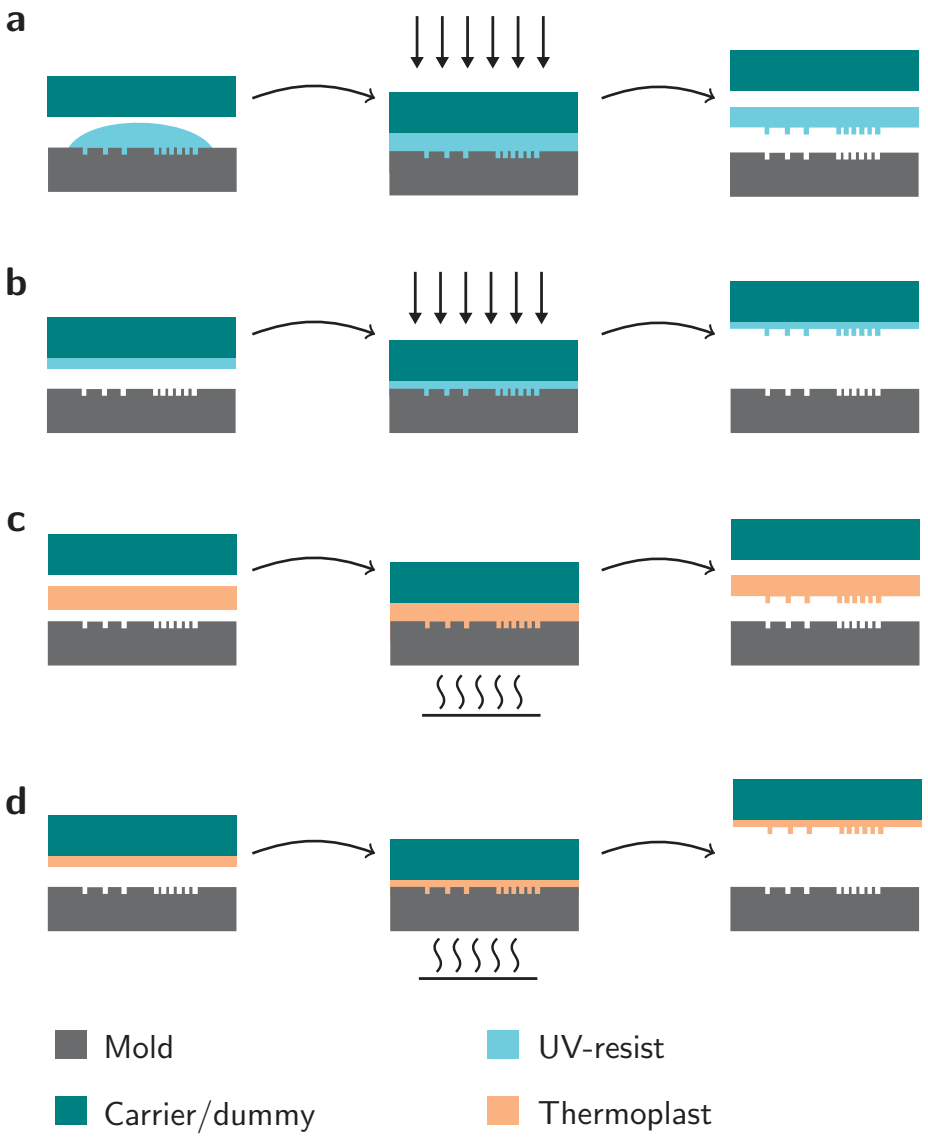

Figure 2.3: UV and thermal replication techniques. **a)** UV-casting for creation of bulk samples. **b)** UV-casting of thin film on glass carrier. **c)** Thermal embossing in bulk samples between a mold and a flat silicon wafer. **d)** Thermal embossing in film on glass carrier.

2.1.4 Metallization

In Chapter 4 nanostructured polymer is coated with aluminum to obtain plasmonic effects. For the optical effect to be present in the given case it is needed to have un-coated sidewalls. In order to obtain this property it was chosen to do the metal deposition using an electron beam evaporation system (SCM600 Alcatel). In this case the metal target is heated by an electron beam inside a vacuum chamber with very high vacuum ($< 2 \times 10^{-6}$ mToor) [26]. The result is a flux of evaporated atoms which hit the wafer with substantially no scattering taking place. This leads to line-of-sight depositions, where only horizontal surfaces are covered. In addition to

this the method has a very high sticking coefficient close to one, which indicates that almost all atoms stay where they land in the first place. This leads to no re-deposition on side-walls.

Another choice would have been sputtering [26], which is more commonly used in industry. In this method an Argon plasma is used to sputter of metal atoms from the target. The atoms land on the surface, but in order to maintain the plasma the process is operated at a much lower pressure than evaporation. This leads to gas phase collisions and therefore a wide angle distribution of the incident atoms. This contributes to side-wall deposition as well does the possible re-deposition due to the more energetic particles arriving at the surface.

The thickness and rate of the deposited metal was monitored using quartz crystal microbalance [26].

2.2 Optical characterization

Three main methods of optical characterization have been employed, each of which are described below. In all cases the spectral intensity information was recorded using a grating based spectrometer for detection (Jaz, Ocean Optics), which has a 2048 pixel silicon photodiode. The spectrometer covers a range from $\lambda = 250\,\text{nm}$ to $\lambda = 800\,\text{nm}$ and has an optical resolution of 1 nm.

2.2.1 Optical microscope for small areas

Due to the cost related to EBL, it has been necessary to fabricate small areas for situations were multiple parameters has been varied. In these cases the normal incidence reflectance has been measured using a microscope setup.

The used microscope was a Nikon Eclipse Ti-U inverted microscope, where the samples were illuminated with a halogen lamp (LHS-H100C-1, Nikon). A schematic sketch is shown in Fig. 2.4a. A 50/50 beam splitter allowed for illumination and detection using the same objective. A 4×-objective with low numerical aperture was chosen in order to only include small incident angles. With a numerical aperture of NA = 0.13 light with an angle of up to 7.5 degrees with respect to normal was included in the measurements. With an aperture and the chosen objective the focused spot size was approximately 500 µm in diameter.

The reflected light was via the beam splitter collected with a fiber collimator and via an optical fiber send to the spectrometer.

The sample was positioned prior to a measurement by sending the reflected light to the microscope eye piece instead of the spectrometer.

An aluminum mirror (300 nm on silicon) was used as reference for absolute reflectance measurements.

2.2.2 Automated angle-resolved setup

For measurement of the angular reflectance properties an automated setup was used. The setup is illustrated in Fig. 2.4b.

The sample is placed vertically in a sample holder position on a rotational stage. With this stage it was possible to vary the angle of the surface normal with respect to the incident light θ_{inc}. The detection was done by an optical fiber placed on an arm which could move independently with respect to the sample due to another

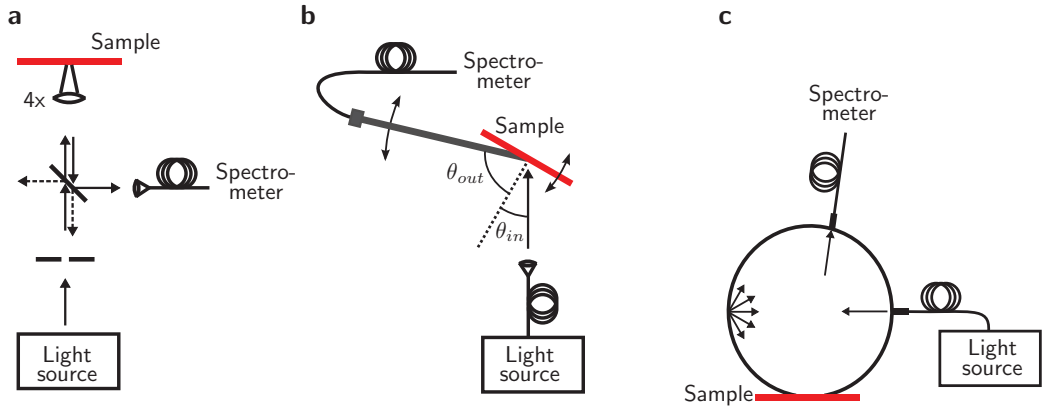

Figure 2.4: Schematics of optical characterization setups. a) Microscope setup for characterization of normal incidence reflectance for small samples. A beam-splitter allows for illumination and collection using the same objective. **b)** Angle resolved setup, where sample and detector may be rotated independently to achieved incident angle θ_{in} and detection angle θ_{out} with respect to the surface normal. **c)** Integrating sphere for diffuse illumination of sample and directional detection. May also be used in a configuration with directional illumination and detection of diffuse reflectance.

rotational stage. The angle of the detector arm relative to the sample normal is denoted θ_{out}. The fiber was directly attached to the spectrometer.

The light source was a Xenon lamp (HPX-2000, Ocean Optics), which via a fiber and collimator was collimated onto the sample. Reference measurements for absolute reflectance measurement were made by placing the detector fiber in the spot without any sample. The full setup was controlled using a PC with LabView.

The setup enables measurements where either incidence angle, observation angle or both are varied automatically. Typical measurements are the angle dependent specular reflectance measurement, where $\theta_{in} = \theta_{out}$ or scattering measurements where only θ_{out} is varied.

2.2.3 Integrating sphere

The integrating sphere used in this work is a ISP-50-8-R-GT (Ocean Optics). It is a sphere coated with material very high diffuse reflectance and with a small opening in the bottom as illustrated in Fig. 2.4c. The diameter of the sphere was 50 mm and the sample port was 8 mm. Two fiber couplings allows for for illumination and detection at either 8° with respect to sample normal or at 90°. In the case of direct illumination the light hits the sample at 8° and the total reflectance is detected in the other port. For the opposite configuration the sample is illuminated diffusely and light leaving the sample at 8° relative to normal, is detected. The two configuration are denoted (8:d) and (d:8) respectively [19]. The diffuse-direct configuration (d:8) is used in Sec. 3.3.1 to simulate diffuse lighting conditions and observation near to normal. The light source used with the integrating sphere is the same Xenon lamp as for the angle-resolved setup and a white reflectance standard (WS-1) is used in reference measurements.

Chapter 3

All-polymer nanostructured surfaces

The assumption of replication based fabrication in it's most strict form with no post processing, implies components made in a single material (pure or pigmented polymer) and structures which allow for release from the mold. This chapter describes such surfaces and the corresponding optical effects. As will become evident the ultimate goal of significant angle-independent colors is not obtainable with these restrictions, however it is possible to obtain surfaces, which under certain circumstances alter the appearance significantly.

The chapter introduces the basic theory needed to understand the observed effects and describes various structures and their optical functionality. Random subwavelength structures and their anti-reflective effect applied to clear and pigmented polymers is described. This is followed by larger self-masked structures, which work as transmission color filters due to scattering. Finally it is discussed which kind of color effects are obtainable with periodic diffraction gratings.

3.1 Background

3.1.1 Governing equations

The starting point for the theoretical treatment of interaction between light and matter is the Maxwell's equations. Simulations and calculations in this work have been performed in the frequency domain and the equations are therefore stated for monochromatic waves, which are harmonic in time with angular frequency ω. The electric field is $\mathcal{E}(t) = \mathrm{Re}\left[\mathbf{E}\exp(-i\omega t)\right]$, where $\mathbf{E}$ is the complex amplitude. The magnetic field $\mathcal{H}(t)$ has a similar form with complex amplitude $\mathbf{H}$. Here it is implicit that the complex amplitude and therefore also the fields are functions of position in space. For a source-free and non-conducting medium these fields are related through Maxwell's equations as [27]

$$\nabla \times \mathbf{H} = -i\omega\mathbf{D} \tag{3.1}$$

$$\nabla \times \mathbf{E} = i\omega\mathbf{B} \tag{3.2}$$

$$\nabla \cdot \mathbf{D} = 0 \tag{3.3}$$

$$\nabla \cdot \mathbf{B} = 0, \tag{3.4}$$

where $\mathbf{D}$ and $\mathbf{B}$ are the complex amplitudes of the electric and magnetic flux densities, which are given by

$$\mathbf{D} = \epsilon_0 \mathbf{E} + \mathbf{P} \tag{3.5}$$

$$\mathbf{B} = \mu_0 \mathbf{H} + \mu_0 \mathbf{M}, \tag{3.6}$$

where $\mathbf{P}$ is the polarization density and $\mathbf{M}$ is the magnetization density. In this work all materials are assumed to be linear, homogenious, isotropic and non-magnetic in which case

$$\mathbf{D} = \epsilon_0 \epsilon_r \mathbf{E} \tag{3.7}$$

$$\mathbf{B} = \mu_0 \mathbf{H}, \tag{3.8}$$

where ϵ_r is the relative permittivity, which in this work also is denoted the dielectric constant and which in general is dependent on frequency. The dielectric constant describes the material response to an applied electric field and light propagation properties such as the speed of light and loss are given, when the dielectric constant is known. For conductive materials, which will be used in Chapter 4 a current density, $\mathbf{J}$ must be included in Eq. (3.1). For materials with linear conductivity, σ, Ohms law applies such that

$$\mathbf{J} = \sigma \mathbf{E}. \tag{3.9}$$

In this case the current density may be included in Maxwell's equations through a complex dielectric constant $\epsilon_r = \epsilon' + i\epsilon''$ [27].

Often, the refractive index $\tilde{n} = n + i\kappa$ is used instead of the dielectric constant. The real part of the refractive index n is the ratio between the speed of light in vacuum and in the material and the imaginary part κ is the extinction coefficient related to the loss. The refractive index and the dielectric constant are related by the simple relation

$$\tilde{n} = \sqrt{\epsilon_r} \tag{3.10}$$

At the boundaries between two different materials (1 and 2), the fields are related with the following boundary conditions

$$D_1{}^{\perp} = D_2{}^{\perp} \tag{3.11}$$

$$B_1{}^{\perp} = B_2{}^{\perp} \tag{3.12}$$

$$E_1{}^{||} = E_2{}^{||} \tag{3.13}$$

$$H_1{}^{||} = H_2{}^{||}. \tag{3.14}$$

For components of the fields normal to the interface it is the electric and magnetic flux densities, which are continuous, while for the parallel components it is the electric and magnetic fields which are continuous. These boundary conditions are used when solving Maxwell's equations in rigorously coupled wave analysis (RCWA) in this chapter and in finite element simulations in Chapter 4.

It can be shown that in order to fulfill Maxwell's equations all components of the electric and magnetic fields must satisfy the wave equation

$$\nabla^2 U(\mathbf{r}, t) = \left(\frac{n}{c_0}\right)^2 \frac{\partial^2}{\partial t^2} U(\mathbf{r}, t) \tag{3.15}$$

where the wavefunction $U(\mathbf{r}, t)$ represent each of the vector components. As above it is assumed that the wavefunction is harmonic in time such that

$$U(\mathbf{r}, t) = U(\mathbf{r}) \exp(-i\omega t). \tag{3.16}$$

If this is inserted in Eq. (3.15) the Helmholtz equation emerges, which is purely concerned with the spatial component of the wavefunction.

$$\nabla^2 U(\mathbf{r}) + k^2 U(\mathbf{r}) = 0, \tag{3.17}$$

where $k = 2\pi\tilde{n}/\lambda_0$ is the wavenumber.

3.1.2 Optical properties of polymers

Most polymers in their pure form do not facilitate significant absorption in the visible wavelength range. Therefore they are either transparent or translucent depending on the micro-structure. Amorphous polymers where the polymer chains are randomly entangled are transparent, whereas semi-crystaline polymers are translucent due to scattering on the grain boundaries.

Unless anything else is stated in the following the polymers will be assumed to be transparent with real refractive index. The absorption is assumed to be negligible. For most polymers the refractive index is approximately $n = 1.5$ and weakly dispersive. For flat surfaces the TE and TM reflection coefficients are given by the Fresnel coefficients, which may be derived from Eqs. (3.11)-(3.14) [28]

$$r_{TE} = \frac{\cos\theta_i - \sqrt{{n_r}^2 - \sin^2\theta_i}}{\cos\theta_i + \sqrt{{n_r}^2 - \sin^2\theta_i}} \tag{3.18}$$

$$r_{TM} = \frac{-{n_r}^2 \cos\theta_i + \sqrt{{n_r}^2 - \sin^2\theta_i}}{{n_r}^2 \cos\theta_i + \sqrt{{n_r}^2 - \sin^2\theta_i}}, \tag{3.19}$$

where θ_i is the angle of incidence, $n_r = n_2/n_1$ is the ratio between the refractive indices of the medium from where the light reaches the interface (n_1) and the medium where the transmitted light leaves the interface (n_2). The reflection coefficients give the magnitude and phase shift of the reflected electric field with respect to the incident field. The surface reflectance is given by the absolute square of the reflection coefficients, and is plotted in Fig. 3.1 for both external ($n_2 > n_1$) and internal ($n_1 > n_2$) reflection.

First we examine the case of most direct interest, namely external reflectance, which is the case if we have light incident from air onto a polymer surface. For typical lighting conditions the reflectance of unpolarized light (dashed line) is of greatest interest and it is found as the average between TE and TM reflectance [28]. In a very large angle interval from normal incidence to above 60 degrees the reflectance of unpolarized light is below 10 %. In fact for normal incidence the reflectance is as low as 4 %. If we assume the replication condition of non-negative sidewall slopes it may be shown that one cannot produce a structure, which leads to higher reflectance than that of a flat surface [29]. This means that no matter in which way the polymer surface is modulated, it is not possible to increase the total reflectance from a single interface to values higher than 4 % for normal incidence. The implications of this

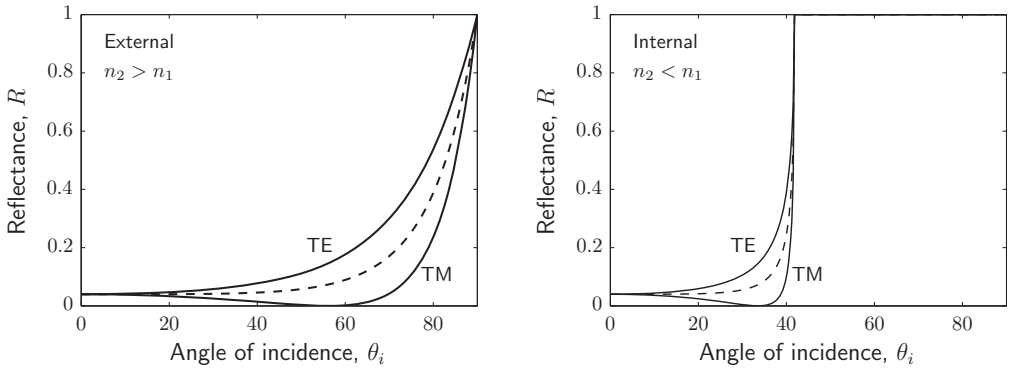

Figure 3.1: Fresnel reflectance The reflectance of a flat interface between air and polymer with a refractive index of 1.5 for both the external (air-to-polymer) and the internal case (polymer-to-air). The reflectance depends on the polarization. For unpolarized light the reflectance is the average of that of TE and TM as indicated by the dashed lines.

is that the amount of light available for re-distribution by an engineered surface topography in order to create color effects is very limited. For higher angles the reflectance increases towards unity at incidence along the surface horizon. Therefore the total reflectance for diffuse incident light amounts to 9.2 % which is found by integration over all angles of the hemisphere.

For the internal case the situation is different as seen in Fig. 3.1. While the normal incidence reflectance is the same as for the external case it increases to unity much faster with increasing angle. Above the critical angle all light is reflected via total internal reflection. This may be utilized when assuming certain polymer geometries such as the thick polymer foil which is described below in Sec. 3.3.3.

3.1.3 Diffraction theory

When light is either reflected from or transmitted trough a surface with a modulated topography the wavefront is modulated accordingly. Due to diffraction this alters the light propagation to the far field, where the effect of the surface modulation may be observed as diffraction patterns. This could for example be the colored orders arising when white light interacts with a periodic grating. The following introduces the basic diffraction theory needed to understand the work carried out in this thesis.

First scalar theory is introduced. Here it is assumed that the light may be described using a single scalar wave function, which must fulfill the wave equation in Eq. (3.15) and the Helmholtz equation in Eq. (3.17). The coupling between the vector components from Eqs. (3.1) - (3.4) and the boundary condition of Eqs. (3.11) - (3.14) are neglected. This approximation can be applied in the cases, where the structural feature sizes are larger than the wavelength [30]. As will be demonstrated in Sec. 3.3.2 it is possible to successfully apply this approximation for diffraction from structures with vertical and lateral sizes of 2-3 wavelengths.

Let the focus be on a situation as shown in Fig. 3.2. A wave is incident onto a surface with a given surface topography at $z = 0$. Right after propagation through the surface the wavefunction is $U(x, y, 0) = U'(x', y')$. Here all quantities related to the interface are marked with an apostrophe. For the case of transmission through a

structured polymer surface will $U'(x', y')$ differ from the incident wavefunction due to the phase modulation at the surface. For the case of reflection from a structured surface the principles are the same except the way the phase modulation due to the surface are calculated. If the propagation from the surface is modeled using spherical wave propagation from each point on the wavefront (Huygen wavelets), the wavefunction in a point (x,y,z) away from the surface may now be written as [31]

$$U(x, y, z) = \frac{1}{2\pi} \int_{-\infty}^{\infty} \int_{-\infty}^{\infty} U'(x', y') \frac{z}{r} \left(ik + \frac{1}{r} \right) \frac{\exp(-ikr)}{r} dx' dy', \tag{3.20}$$

where

$$r = \sqrt{(x - x')^2 + (y - y')^2 + z^2}. \tag{3.21}$$

Eq. (3.20) is denoted the Rayleigh-Sommerfeld integral and it can be shown that this integral form of $U(x, y, z)$ fulfills the Helmholtz equation, Eq. (3.17).

Different levels of assumptions may be applied to the Rayleigh-Sommerfeld integral to solve specific cases. For example for the propagation to a plane far away from the surface is the Fraunhofer approximation applied where the result expressed in terms of the intensity at the plane is

$$\frac{I(x, y, z)}{I_{inc}} = \frac{1}{\lambda^2 z^2} \left| \mathcal{F} \left\{ U'(x', y') \right\}_{\frac{x}{\lambda z}, \frac{y}{\lambda z}} \right|^2, \tag{3.22}$$

where $\mathcal{F} \{U'(x', y')\}_{\frac{x}{\lambda z}, \frac{y}{\lambda z}}$ is the Fourier Transform of $U'(x', y')$ evaluated at the spatial frequencies $\nu_x = \frac{x}{\lambda z}$ and $\nu_y = \frac{y}{\lambda z}$.

Harvey et al.[32] showed that for a hemispherical observation space, as probed by the angular resolved measurement setup used in this work (see Sec. 2.2.2) the proper quantity to relate to is the radiance, L, and that it is given by

$$L(\alpha, \beta) = \frac{\lambda^2}{A_s} \left| \mathcal{F} \left\{ U_0'(\hat{x}', \hat{y}') \right\} \right|^2, \tag{3.23}$$

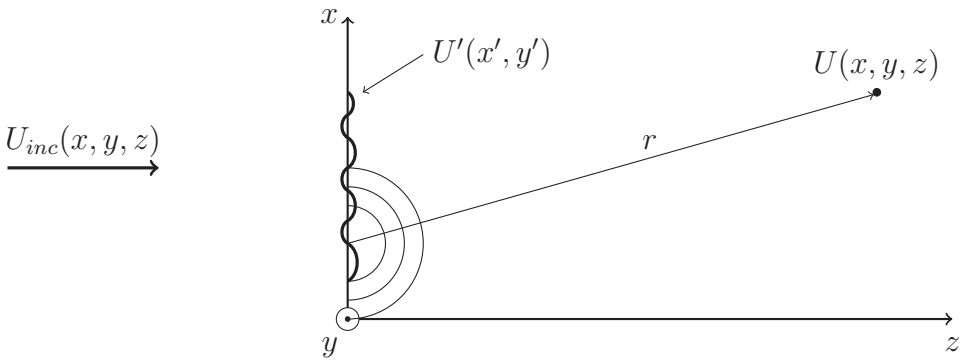

Figure 3.2: Sketch of diffraction. An incident wave (e.g. a plane wave) is incident onto a surface which alters the wavefront resulting in the wavefunction $U'(x', y')$ right after the aperture. Each point of the wavefront propagates through a spherical wave to the point (x,y,z) where the total wavefunction may be found from integration over all contributions arriving from the aperture.

where $\alpha = x/R$ and $\beta = y/R$ are the direction cosines if R is the hemisphere radius and $\hat{x}' = x'/\lambda$ and $\hat{y}' = y'/\lambda$ are coordinates normalized to the wavelength. In the original work of Harvey [33] the function U_0' is denoted as a generalized pupil function which includes higher order effects due to the finite thickness and lateral extent of the aperture. Consistent with the measurement geometry (small spot compared to R) and application to shallow gratings we will however only include the phase modulation $\Delta\phi(\hat{x}', \hat{y}')$ due to the surface topography while assuming it to be infinite thin, such that no diffraction takes place within the structured region. This gives

$$U_0'(\hat{x}', \hat{y}') = U'(\hat{x}', \hat{y}') = U_{inc} \exp(-i\Delta\phi(\hat{x}', \hat{y}')). \tag{3.24}$$

The expression for $\Delta\phi$ will be written in detail, when applying the theory on randomly structured surfaces in Sec. 3.3.2.

Now we go to diffraction gratings where the modulation of the incident light is periodic with period Λ. Due to the single spatial frequency $1/\Lambda$ contained in the grating and the fact that the far field diffraction pattern is found from the Fourier transform of the phase modulation we have for an incident plane wave that the diffraction pattern is discrete directions of propagating light, known as orders. The diffraction equation is a result of this here for a periodic modulation in one direction

$$n_{out} \sin\theta_m - n_{in} \sin\theta_{in} = \frac{m\lambda}{\Lambda}, \qquad m = 0, \pm 1, \pm 2, ... \tag{3.25}$$

where n_{in} and n_{out} is the refractive indices of the incident and outgoing media respectively and θ_{in} is the incident angle. The order number is denoted m and the m'th order is propagating in the direction θ_m.

The scalar diffraction theory as presented above will not provide information on the absolute values on the transmittance and reflectance. To obtain this information it is necessary to solve Maxwells equations. For periodic structures this is possible using a method know as rigorously coupled wave analysis (RCWA) [34], which have been the preferred method for determination of diffraction efficiencies of dielectric gratings throughout this work.

In the method of RCWA the structure is partitioned into a number of horizontal layers each of which are periodic in the lateral directions and constant in the vertical direction. For a binary grating it is therefore only necessary to have one layer, while a sloped profile is approximated with multiple layers. The more layers, the better approximation to the sloped profile. The multilayer system is solved by expressing the permittivity in each layer as a Fourier series and then matching the fields at the layer boundaries using the standard boundary conditions including the multilayer reflections in the structure. The result is a system of linear equations which may be solved. The number of terms contained in this series expansion of the permittivity determine the accuracy of the method. In this work a commercial available implementation for MATLAB (GD-Calc [35]) has been used. The number of terms in the series was set to 15 for calculations with few diffraction orders. This was sufficient for the results to converge.

3.1.4 Anti-reflecting surfaces

The reflectance of light at air-polymer interfaces was described above in Sec. 3.1.2. As mentioned it is not possible to increase the overall reflectance by topographies

which comply with the injection molding criterion. It is however possible to lower the reflectance, which is useful for reduction of glare in products such as displays or glasses. The conventional technique, employed in glasses and camera lenses, is to apply a hard coating consisting of one or more thin films of dielectric materials. This method works by destructive interference in the backward direction and it can be shown that zero reflectance may be achieved by use of a single thin film with quarter wave thickness $t = \lambda_0 n_{coat}/4$ and refractive index $n_{coat} = \sqrt{n_{sub}}$, where n_{sub} is the refractive index of the underlying substrate [27]. This method is very robust, but suffers from high cost due to the need for vacuum deposition of the film.

The thin films may be replaced by surface structures which give similar functionality. There are two overall strategies, when designing these. The first method is to mimic the functionality of the single thin film. This is done by subwavelength structures with a binary height profile. This could for example be pillars arranged in a periodic grid as seen in Fig. 3.3a. Due to the subwavelength nature of the structures the structured region can with good approximation be seen as a thin film with an effective refractive index, n_{eff} [36]. Based on the refractive indices of the substrate (polymer) and the superstrate (air) and the polymer filling volume fraction f, the effective refractive index may be calculated from an effective medium theory. For the specific case of air and polymer, where the refractive indices are real and close in value, a simple weighted average of the refractive index is a good approximation. There exists other approaches within effective medium theory, such as the Maxwell-Garnett model and the Bruggerman approximation [36]. The weighted average, which is used here has the following form

$$n_{eff} = (1 - f)n_{air} + (1 - f)n_{polymer} = n_{air} + f(n_{polymer} - n_{air}). \tag{3.26}$$

In order to avoid diffraction effects, the period Λ must be kept small. This is given by the diffraction equation, Eq. (3.25), which may be rearranged to define to criterion for pure zero order reflection and transmission

$$\Lambda < \frac{\lambda_{min}}{n_{polymer} + n_{air} \sin \theta_{inc}}, \tag{3.27}$$

where θ_{inc} is the angle of incidence and λ_{min} is the smallest wavelength of relevance. For this criterion to be fulfilled in the visible spectrum for all incident angles the period must be smaller than 160 nm.

In Fig. 3.3a are the reflectance at normal incidence of three binary polymer gratings shown, each with a height of $h = 100$ nm, but with different filling fractions, f. For reference is the reflectance of a flat interface included. The reflectance has been calculated using effective medium theory and transfer matrices [27]. This method was shown to agree very well with full RCWA calculations with less than 0.001 absolute difference in the calculated reflectance values. The optimal filling fraction is $f = 0.45$, which fulfills the $n_{eff} = \sqrt{n_{sub}}$ criterion. For this structure the reflectance goes to zero around $\lambda = 500$ nm and increases slightly away from this point. It is seen that when the filling fraction changes the effect is reduced since it is no longer possible to obtain the π-phase shift between the light reflected at the top and bottom of the structured layer, which leads to the to total extinction in the backward direction. The surfaces do however still reflect less than half of that of a flat surface.

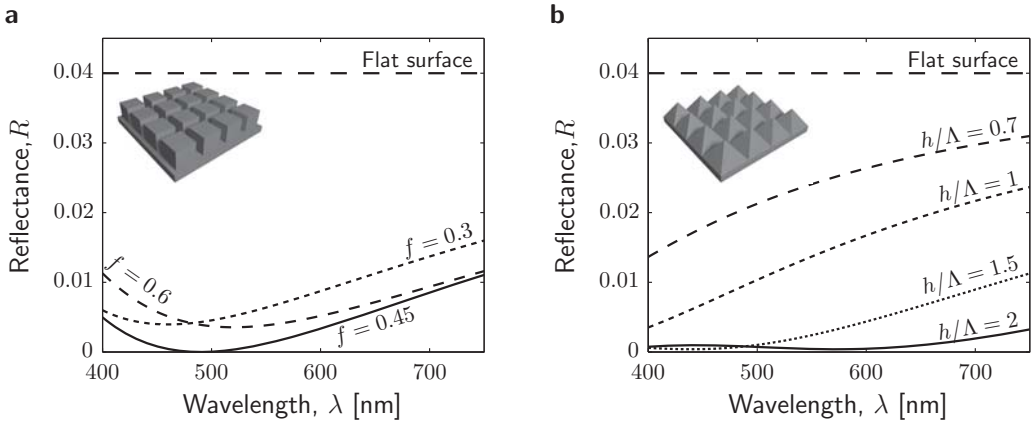

Figure 3.3: Calculated AR effect. a) Effect of binary structures modelled using effective medium theory. Structures are 100 nm high with filling fraction f. The inset shows an example of $f = 0.45$. **b)** Effect of pyramid shaped structures for different aspect ratios h/Λ. The inset show the situation for $h/\Lambda = 0.7$.

A second strategy is to use tapered subwavelength surface structures which in the effective medium picture creates a gradient in the effective refractive index. An example could be pyramid structures protruding from the surface as illustrated in Fig. 3.3b, where the calculated reflectance of such pyramid shaped surface structures are shown for different aspect ratios h/Λ. The smallest aspect ratio of 0.7 corresponds to what may be obtained if a mold was made by anisotropic KOH etch of a (100) silicon surface [37]. Again the effective medium theory and transfer matrices are used in the calculation, by splitting the tapered region into a high number of horizontal layers with each their effective refractive index. The period is in all cases $\Lambda = 150$ nm and the aspect ratio is increased by using higher pyramids. It is seen that the structure become more effective as the aspect ratio is increased and for $h/\Lambda = 2$ the reflectance is lowered by more than 90% over the entire wavelength interval compared to the flat surface. It should be noted that the exact refractive index profile plays a role and other air-to-polymer transitions than the 4-sided pyramid lead to slightly different results, however with the same trend as the aspect ratio increases.

For simplicity the treatment here has been for periodic structures. Lithography techniques which leads to non-periodic may be employed with success to create structures over large areas. Below in Sec. 3.3.1, AR structures which are fabricated by the black silicon method described in Sec. 2.1.2 are used. These structures are not placed in a grating and it is not possible to apply the condition on the lateral dimension of Eq. (3.27) directly. The effective medium description and the gradient mechanism described here are however still applicable to explain the observed effect.

3.1.5 Diffuse scattering from pigmented polymers

Pigmented polymers constitutes a large portion of the used polymers for e.g. toys where the bulk plastic is desired to have a certain color. The pigment is typically absorption colorants, which due to wavelength selective absorption results in a colored appearance. Often the pigments consist of small particles of compounds with the desired absorption properties. Examples of pigments are titanium oxide for

purely scattering (white), carbon black for high absorption (black) or various metal oxides for different wavelength ranges of absorption [19]. The light paths of light interacting with a pigmented polymer is illustrated in Fig. 3.4. Incident light will be reflected and transmitted in accordance with the Fresnel coefficients and Snell's law. The transmitted light interacts with the pigment in a series of scattering and absorption events. For a finite slab of pigmented polymer the light is either absorbed, transmitted, or reflected. In the following the focus will be on semi-infinite substrates by assumption of very thick samples or high pigment concentration leading to a negligible amount of light which will reach the backside a given sample.

To treat the scattering in the substrate the theory of radiative transfer is applied. Developed by Chandrasekhar [38] for applications within astronomy this theory describes the result of multiple scattering in homogenous scattering atmospheres (slabs with scattering particles). The radiative transfer equation is central in this theory and for the case of isotropic scattering it has the form

$$\mu \frac{dL(\tau,\mu)}{d\tau} = L(\tau,\mu) - \frac{\rho}{2}\int_{-1}^{1} L(\tau,\mu')d\mu', \tag{3.28}$$

where $L(\tau,\mu)$ is the radiance at optical thickness τ in direction μ where $\mu = \cos\theta$ is the direction cosine, with θ defined from the z-axis as illustrated in Fig.3.4. This means $\mu = -1$ is forward propagation and $\mu = 1$ is backward propagation. The wavelength dependent single scattering albedo, ρ, describes the amount of scattered light compared to the total interaction with the pigment particles. It is given by

$$\rho = \frac{S}{S+K}, \tag{3.29}$$

where S is a scattering coefficient and K an absorption coefficient. For $\rho = 0$ only absorption takes place, while $\rho = 1$ describes pure scattering. The radiative transfer equation is an integro-differential equation, which Chandrasekhar solved by use of Gaussian quadrature on the integral. The resulting system of differential equation may be solved and the bi-directional reflectance distribution function, f_r, for an

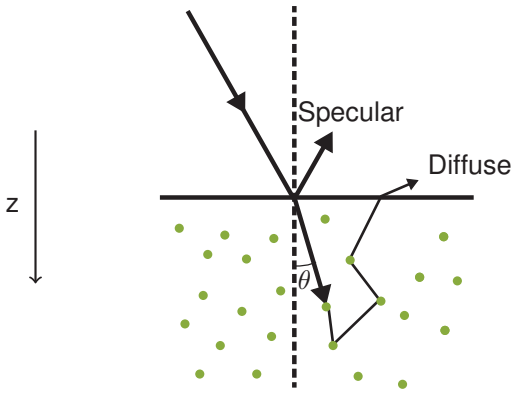

Figure 3.4: Specular and diffuse reflectance. Incident light is specular reflected at the surface of the polymer. The transmitted light interacts with the pigment in a scattering process resulting in a colored diffuse flux. Here only one ray path of the diffuse light is shown.

infinite slab is [38]

$$f_r = \frac{\mathrm{d}L_r}{\mathrm{d}E_i} = \frac{\mathrm{d}L_r}{L_i \cos(\theta_i)\mathrm{d}\omega} = \frac{\rho}{4\pi}\frac{1}{\mu_i + \mu_r} H(\mu_i)H(\mu_r) \tag{3.30}$$

where ρ is the single scattering albedo and the N'th order approximation to the function $H(\mu)$ is given in terms of the N positive zeros μ_j of the Legendre polynomial of degree $2N$

$$H(\mu) = \frac{1}{\mu_1 ... \mu_N} \frac{\prod_{j=1}^{N}(\mu + \mu_j)}{\prod_{\alpha=1}^{N}(1 + \kappa_\alpha \mu)}. \tag{3.31}$$

Here κ_α are the solutions to the characteristic equation

$$1 = \sum_{j=1}^{N} \frac{w_j \rho}{1 - \kappa^2 \mu_j} \tag{3.32}$$

where w_j are the weights corresponding to the zeros μ_j of the Legendre polynomium. The bi-directional reflectance distribution function describes the reflected radiance in the direction μ_r for a given incident irradiance in the direction μ_i.

This result is for the case, where the refractive index does not vary inside and outside the scattering atmosphere, however Wolff [39] included a refractive index change at the surface leading to both external and internal reflections and derived a close form expression for high single scattering albedo. Below, in Sec. 3.3.1 his approach is used to describe the effect of anti-reflective structures in the surface of pigmented polymers, however with inclusion of low scattering albedos (high absorption) by use of numerical evaluation of Eqs. (3.31) and (3.32). In this work a high order approximation to the H-function was used such that the result did not depend on N. The used value was $N = 30$.

Another and somewhat simpler model often used to describe light interaction with pigmented materials is the Kubelka-Munk theory, which assumes purely diffuse fluxes inside the material. This model is described elsewhere[19].

3.2 Previous work

Below are examples of state-of-the-art of engineered structural color effects and anti-reflective effects in dielectric materials shown.

3.2.1 Anti-reflection

There has been a large interest in the recent years to explore the concepts of anti-reflection described above in Sec. 3.1.4. Here the examples are limited to applications in polymers for appearance purposes.

There are many different approaches to achieve tapered structures in the sub-wavelength regime. In Fig. 3.5 are structures and their effects of three different approaches shown. Direct plasma etching in the surface of the polymer [40] is shown

in Fig. 3.5a. Here the polymer (PMMA) surface is etched using an oxygen plasma and an argon ion bombardment to achieve tapered nanostructures. The resulting structures show significant enhancement of the transmitted light compared to that of a planar surface, also for high incidence angles. Yanagishita *et al.* [41] demonstrated high performance of anti-reflective structures fabricated in the surface of microlenses. The structures were formed directly in an aluminum mold by creation of porous anodized alumina in the surface. This is illustrated in Fig. 3.5b, where both alumina mold and the resulting structures are shown. The major advantage of this method is that free form surfaces may be covered with nanostructures even at very high slopes. In this case are the lenses fabricated using mechanical deformation of the aluminum and the surface structures subsequently formed in an electro-chemical process. The replication in polymer was done using a UV-casting process.

The third method is also a replication process. In this case very tall and narrow surface structures are first formed in silicon in a plasma etch and then, via an electro plated Ni-Co mold, replicated in PMMA using hot embossing [42]. The resulting surface show a reduction of the glare as shown in Fig. 3.5c, where the underlying text easier is read through the structured PMMA.

3.2.2 Structural colors in dielectric materials

Within color effects which work under the replication constraint the main focus is on effect surfaces such as grating based holograms, which leads to colorful logos and text. The gratings are typically arranged with a macroscopic layout leading to a colorful display of the geometry, when observed under bright light. An example of such an effect is seen in Fig. 3.6a where such gratings are replicated in dark

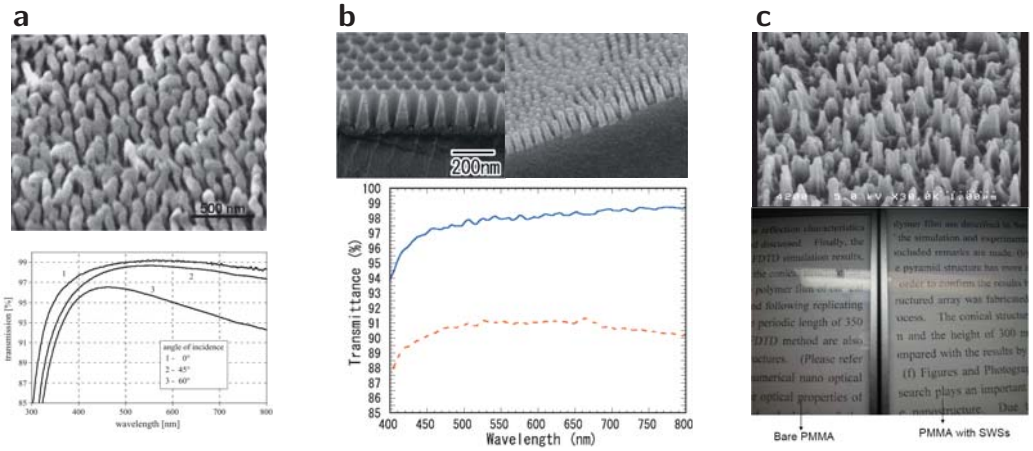

Figure 3.5: Anti-reflective effects in polymers. a) AR structures formed by direct plasma etchning in PMMA showing AR effect for high angles of incidence. From Kaless *et. al* [40]. **b)** AR structures formed in the surface of lenses from porous anodized alumina. Dashed line show transmittance without the structures and full line the transmittance with the structures. From Yanagishita *et al.* [41]. **c)** Replication of tapered structures into PMMA from Ni-Co mold made from electroplating of plasma etched silicon surface. The PMMA show reduced glare with the structures. From Ting *et al.* [42].

chocolate. Recently a company [43] has specialized in production of chocolate molds with hologram structures, which are then transferred to the chocolate in the production. Similar effects are seen for security applications in bank notes and stickers for protection against unauthorized replication. In these are the gratings often coated with a metal to enhance the reflectance. Otherwise the field is highly dominated by concepts which utilize processes and materials which are not part of the basic idea of NanoPlast. Two examples, which are directly inspired by the Morpho butterflies are shown in Fig. 3.6b-c, where multilayers are deposited on a structured substrate.

Saito *et al.* [15, 44] did this by deposition of alternating layers of SiO_2 and TiO_2 on an imprinted semi-random structure. The thickness of the layers determine the color of the reflected light and the random underlying structure secures scattering in direction different from the specular direction. Another example is by Chung *et al.* who did this by deposition of the multilayer stack on top of a layer of differently sized silica spheres (200-400 nm) [45, 47]. The resulting structure may be embedded in elastomer to create flexible foils with the distinct color depending on the thickness of the deposited layers. The angular properties are very nice, with diffuse reflectance arising from the disorder of the structure.

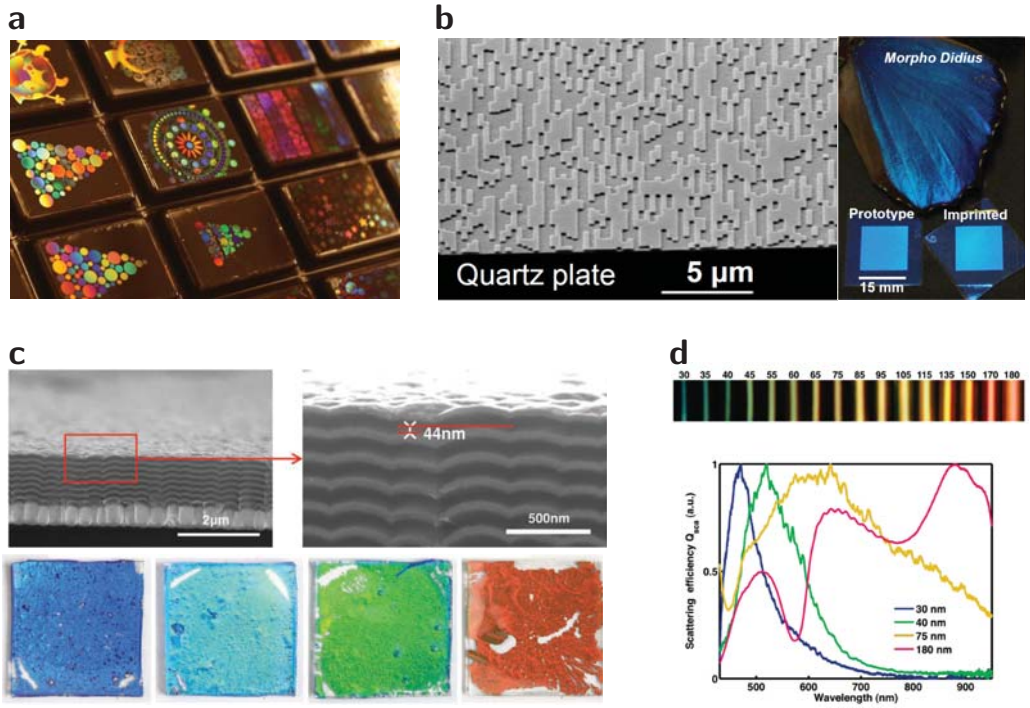

Figure 3.6: Structural color effects in dielectric materials a) Holographic chocolate displaying bright colors arising from diffraction gratings in the surface. From Morphotonix [43]. **b)** Semi-randomly structured substrate on which a multilayer stack is deposited. The disorder from the substrate leads to scattering of the light, thereby mimicking the effects of the Morpho butterflies. From Saito *et al.* [44]. **c)** Multilayer stack deposited on a monolayer of differently sized silica sphere. The color is determined by the layer thicknesses. From Chung *et al.* [45]. **d)** Silicon nanowires which possess resonance based on their size. From Cao *et al.* [46]

Within the field of silicon photonics there are also several demonstrations of color effects arising from nanostructures, one is by Cao *et al.* [46] as shown in Fig. 3.6d, where silicon nanowires possess resonances in the scattered light leading to change in color with changing size of the nanowire. Other examples are silicon gratings as demonstrated by Walia *et al.* [48] or Højlund-Nielsen *et al.* [49], which work in reflection or by Kanamori *et al.* [50], which work in transmission.

3.3 Demonstrated structural color effects

In the following are three different experimental realizations of structural colors in polymers described and explained.

3.3.1 Chroma enhancement of pigmented polymers using AR structures

The theoretical obtainable effects of anti-reflective structure in the surface of a polymer was described in Sec. 3.1.4. Here it is studied how a modification in the surface reflectance at the air-polymer interface affects the color appearance of a pigmented polymer. A simple model is derived to predict the behavior and a small experimental study demonstrates the effect in practice. The basic principles in the theoretical treatment is the same as by Wolff [39]. The results are presented in Paper C.

In the following a semi-infinite slab geometry is assumed with pigment particles in the polymer slab. The medium above the polymer is assumed to be air. All quantities above the surface are marked with an apostrophe and the subscripts i and r denotes quantities related to incident or reflected light. This is illustrated in Fig. 3.7, where θ_i' is the incident angle above the surface and θ_i is the corresponding angle under the surface related to θ_i' through Snell's law.

It will be assumed that the surface is illuminated with diffuse light characterized by constant radiance L_i' as illustrated in Fig. 3.7b. At the surface a certain amount of the light is reflected due to the change in refractive index. For a flat surfaces this reflectance is the Fresnel reflectance shown in Fig. 3.1, however here the goal is to modify this and observe the effect. It is therefore assumed that the reflectance is lowered by a factor α compared to the Fresnel reflectance.

$$R'(\theta_i') = \alpha R_f'(\theta_i') \tag{3.33}$$

where R_f' is the external Fresnel reflectance for unpolarized light at the corresponding flat interface. Here it is assumed that α is independent of both wavelength and angle of incidence. This may be a very crude assumption depending on the AR structures in question.

For the internal case it is assumed that the structures are truly subwavelength with no diffraction orders. This means that the total internal reflection is maintained. This gives

$$R(\theta_r) = \begin{cases} \alpha R_f(\theta_r) & \text{for } \theta_r \leq \theta_c \\ 1 & \text{for } \theta_r > \theta_c, \end{cases} \tag{3.34}$$

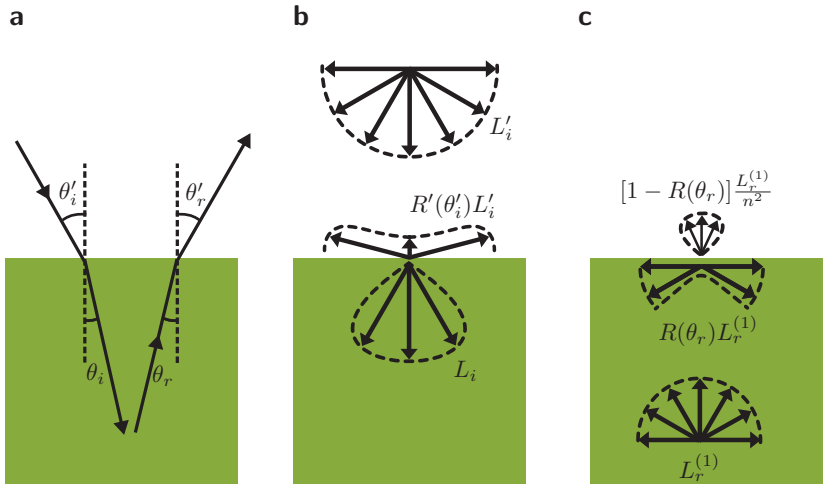

Figure 3.7: Sketch of theoretical treatment a) The relevant angles and notation used in the model. **b)** Diffuse incident light is reflected and transmitted through the polymer surface. The resulting backward and forward fluxes are shown. **c)** The transmitted light from panel b, is reflected diffusively from the bulk. This reflected flux $L_r^{(1)}$ is partly escaping the polymer through the surface and partly reflected back into the polymer.

where θ_c is the critical angle. For $\alpha < 1$ this leads to a discontinuity right at the critical angle, which is not physical and which is explained by the fact that α will indeed have some angular dependence, especially close to the critical angle.

The radiance of the specular reflected light is therefore $R'(\theta_i')L_i'$. Below the surface the incident light takes the form of angle-dependent diffuse light with radiance

$$L_i(\theta_i) = \begin{cases} [1 - R'(\theta_i')]\, n^2 L_i' & \theta_i \leq \theta_c \\ 0 & \theta_i > \theta_c \end{cases}, \tag{3.35}$$

which arise due to Snell's law and the angle dependent transmittance $[1 - R'(\theta_i')]$. This light now interacts with the pigment giving rise to a diffuse reflected flux which is denoted $L_r^{(1)}$, where the index 1 indicates that the light has undergone 1 diffuse reflection from the bulk. Semi-infinite sample and isotropic scattering are assumed in which case the bi-directional reflectance distribution function, f_r of Eq. (3.30) can be applied. For the first diffuse reflected flux this gives

$$\mathrm{d}L_r^{(1)} = f_r\left(\cos\theta_i, \cos\theta_r\right) \mathrm{d}E_i = f_r\left(\cos\theta_i, \cos\theta_r\right) L_i \, \cos\theta_i \, \mathrm{d}\omega_i \tag{3.36}$$

$$L_r^{(1)} = 2\pi \int_0^{\frac{\pi}{2}} f_r\left(\cos\theta_i, \cos\theta_r\right) L_i \cos\theta_i \, \sin\theta_i \, \mathrm{d}\theta_i. \tag{3.37}$$

The diffusely reflected light with angle dependent radiance $L_r^{(1)}$ interacts with the surface according to Eq. (3.34) and a fraction $[1 - R(\theta_r)]\, L_r^{(1)}$ escapes the polymer, while a fraction $R(\theta_r)L_r^{(1)}$ is reflected and become the new incident flux. In this way the second diffusely reflected flux becomes

$$L_r^{(2)} = 2\pi \int_0^{\frac{\pi}{2}} f_r\left(\cos\theta_i, \cos\theta_r\right) R(\theta_i) L_r^{(1)} \cos\theta_i \, \sin\theta_i \, \mathrm{d}\theta_i. \tag{3.38}$$

Similarly the j'th reflected radiance from the bulk is

$$L_r^{(j)} = 2\pi \int_0^{\frac{\pi}{2}} f_r\left(\cos\theta_i, \cos\theta_r\right) R(\theta_i) L_r^{(j-1)} \cos\theta_i \, \sin\theta_i \, \mathrm{d}\theta_i. \tag{3.39}$$

The total reflected radiance is therefore given by

$$L_r' = R'(\theta_r') \, L_i' + \sum_{j=1}^{\infty} [1 - R(\theta_r)] \frac{L_r^{(j)}}{n^2}, \tag{3.40}$$

where the first term is the specular reflected radiance and the sum describes the contributions from the bulk.

In practice the sum is evaluated until a certain amount of light has either escaped the surface or been absorbed by the pigment. Here this value has been set to 99.99%. With this model it is possible to determine the effect of a reduction in the surface reflectance for a given pigment if the wavelength dependent single scattering albedo is known.

Before proceeding with the results of the model first a short introduction to the experimental approach. The model is applied to three different pigments, a blue, green and red pigment for use together with the widely used thermoplastic acrylonitrile butadiene styrene (ABS). Flat samples (5 cm in diameter, 2 mm in thickness) were injection molded with each of the three pigments. In order to ensure completely flat surfaces on flat reference samples they were embossed with FDTS coated flat Si-wafers as stamp. Simultaneously with the embossing, two samples were bonded to create thicker samples to better meet the semi-infinte sample assumption. The embossing was done in a parallel plate press at a temperature of 120° and a constant force of 2.5 kN. The pressure was held for 10 minutes followed by cooling to 80° and release of pressure.

The samples with AR structures were made in an identical process, but with a nano-structured stamp comprising large area AR structures. These AR structures were of the gradient type described in Sec. 3.1.4, fabricated using the black silicon method (see Sec. 2.1.2). The specific structures were described in paper B, where they are denoted Type A. In the paper are the transmission properties including

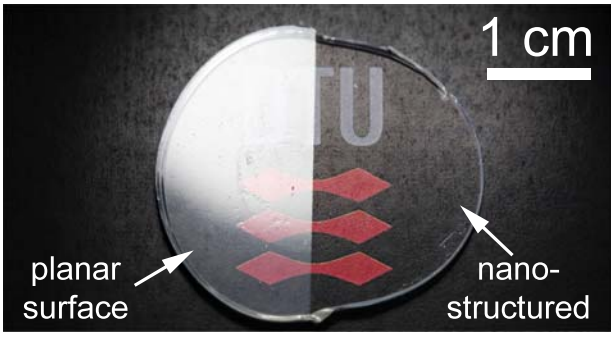

Figure 3.8: AR structures in clear polymer Transparent Ormocomp sample with AR structures on both front and back of the right side, while no structures are present on the left side. The sample is placed on a printed DTU logo and the improved ability to read the underlying text in the structured side is evident.

scattering of this and four other types investigated and related to the dominating lateral spatial frequency of the surfaces. By Fourier analysis it was shown that the dominating period of this specific structure was 180 nm, but with components of higher periods also. This will inherently lead to a small amount of scattering from the structures, which in Paper B is observed as a drop in the specular transmitted light. It is however important to note that the total transmittance is increased. In Paper B the optical effect of the structures in clear polymeric material was demonstrated and compared to a surface without structures. This is shown in Fig. 3.8, where it is apparent that the structures have a significant effect in the suppression of the reflection at the surface and that the small amount of scattering does not disturb the effect for this type of application.

As described above the transfer of AR structures into the colored ABS is done by embossing in this study. Top and side view images of the stamp and top view of the resulting ABS surface is shown in Fig. 3.9. In another study [51] it was shown that it is possible to fabricate these structures using injection molding in an industrial setting and to reduce the reflectance to approximately half its value in another widely used thermoplastic, poly-propylene (PP).

Returning to the result of the model in Eq. (3.40) it is with the flat reference samples possible to extract the single scattering albedo for each of the three pigments, by measurement of the diffuse-direct (d:8) reflectance measured using integrating sphere (see Sec. 2.2.3) and comparing this to the model setting $\alpha = 1$ corresponding to simple Fresnel reflection at the surface. These measured spectra are shown in Fig. 3.10a, where they are denoted as $\alpha = 1$. By using the calculated single scattering albedo for each pigment and changing α it is seen how the spectra changes as illustrated for the example of half the reflectance ($\alpha = 0.5$) and for complete removal of surface reflection ($\alpha = 0$). It is seen that at the wavelengths with high absorption and therefore low reflectance the reflectance is lowered even more, when α decreases. Where there is high initial reflectance no significant change is predicted.

When looking at the absolute values of the color changes it is seen that it is not a dramatic change. The increase in chroma for the green and red pigment is approximately 10 times the just noticeable difference of 2.3 (see Sec. 1.3). The

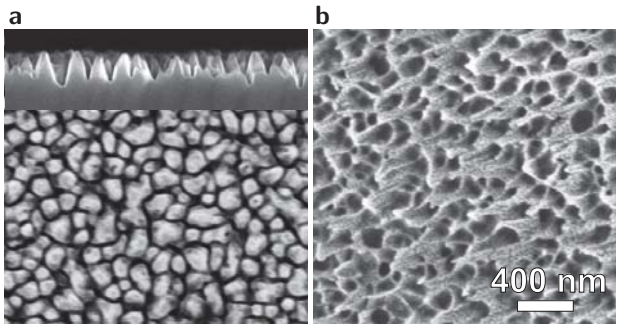

Figure 3.9: AR structures used for chroma enhancement a) Top and side view SEM images of the Si master comprising random tapered AR-structures. **b)** Top view SEM image of ABS surface after embossing. A thin layer of gold is sputtered on the surface prior to imaging to avoid charging. The scalebar applies to both panels a and b.

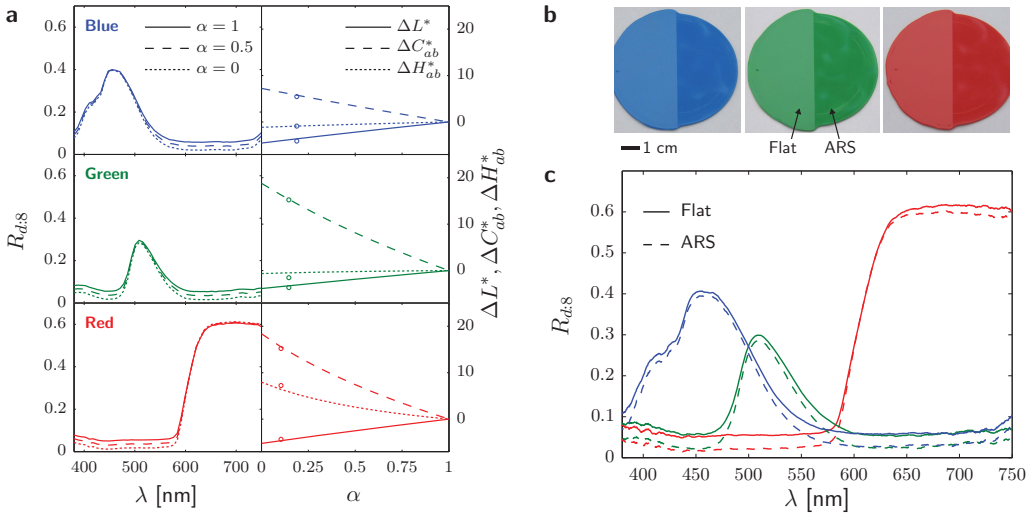

Figure 3.10: Theoretical and experimental results for color change a) Experimentally extracted single scattering albedos are used to model the effect of AR structure by lowering α. The spectral changes are seen to the left and the corresponding color changes are seen to the right. **b)** Fabricated ABS samples with AR structures on only the right side. **c)** Experimentally obtained reflectance spectra for flat and structured surfaces.

calculated spectra have been converted to color values using the cylindrical coordinates of the CIELAB color system, described in Sec. 1.3. These coordinates are chosen to be able to comment on general trends introduced by the surface structure without dependence on the color of the pigment. The color values have been compared to the values of a flat surface and the changes in color coordinates, ΔL^*, ΔC^*_{ab}, and ΔH^*_{ab}, are seen in Fig. 3.10a as function of α. As one would expect there is an increasing color change with decreasing value of α. It is noticeable that the overall change in color for all pigments is mainly manifested as an increase in chroma. This is due to the increase in reflectance ratio between the high and low reflectance regions of the spectra, which is expected to give a more pure color appearance.

The actual appearance change of the realized surfaces is illustrated in Fig. 3.10b. Here imprints are shown which were made using a master where only half of it was covered with nanostructures. The pictures were taken in a photo box with diffusive light and with the camera placed near to normal to mimic the measured and simulated conditions. In Fig. 3.10c are the experimental spectral changes seen where the (d:8)-reflectance has been measured for both the flat surface and the surface with AR-structures. The calculated color change due to the structures is marked in Fig. 3.10a as small circles positioned at the value of α which has the best fit compared to the numerical model. The α-values are seen to lie between 0.1 and 0.2 for the three cases. Ideally it should be the same value, since it is the same structure in all cases. In conclusion both the simple theoretical model and the experiments show an increase in chroma if anti-reflective structures are fabricated in the surface of pigmented ABS. The change is moderate, but is clearly seen in real life.

3.3.2 Scattering on random surface structures

Random tapered nanostructures have been described above, which have been used to lower the surface reflectance with only a small amount of scattering. This is due to the subwavelength nature of these structures. In the study presented here, which was published in Paper A, it is shown how a random texture, formed in a similar way, but with structures of a different length scale may be used for production of transmission color filters, where the color of the transmitted light is given by the specific texture. It is shown how the transmission spectra can be explained by scalar diffraction theory.

The structures in this study were formed in a self-masking process, as described in Sec. 2.1.2, using a RIE-STS Cluster System C004 with gas flows of SF_6 (15 sccm) and O_2 (22.5 sccm). The wafers were etched for 10 minutes at a pressure of 300 mTorr and a platen power of 200 W. The given etch produced silicon wafers with tapered structures across the wafer. As described in Sec. 2.1.2 variations in etch load may course radial dependence on the etch behavior and due to the unstable nature of the black silicon etch, this can course significant structural variations. For this given etch this is indeed the case and the structures used here represents the behavior of structures positioned at different locations in the radial direction.

Three types of silicon structures were identified on the wafers etched with the given recipe and the cross sectional images of these are seen in Fig. 3.11a. The structure denoted type 1 is found on the major central part of the wafer and consists of dense structures with moderate slope connected in a network. The structures are approximately 1 µm high and with similar lateral footprint. The structures of type 2 are significantly higher (2-3 µm) and are still connected in a network. These are

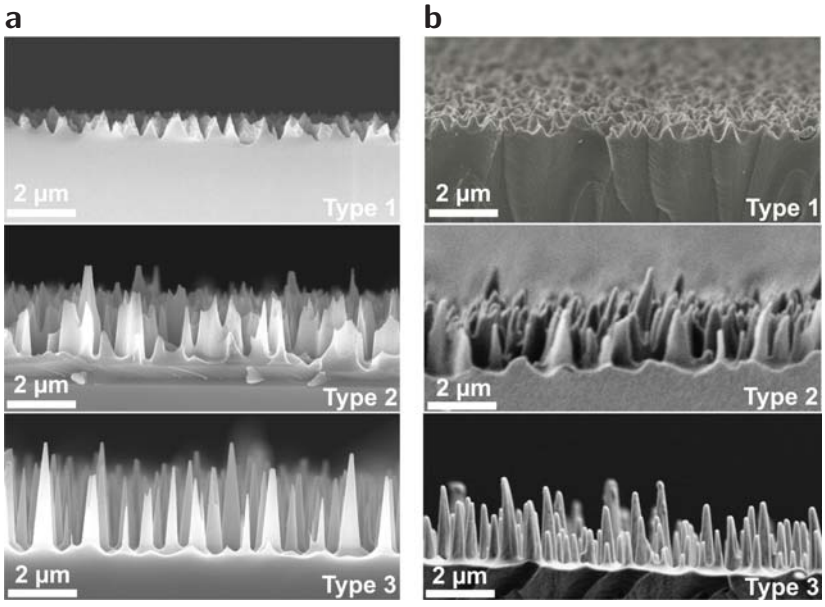

Figure 3.11: SEM cross sections of master and replica. a) Three types of structures in the silicon master as seen with SEM cross section. **b)** Ormocomp replications of the same three types of structures. The replica are made using an intermediate PDMS stamp and UV-NIL.

found 10 mm from the wafer edge. The structures of type 3 take the form of very high isolated spikes (4 µm) and are found 4 mm from the wafer edge.

In Fig. 3.11b are the corresponding replica seen. They are made in a thick (approximately 50 µm) Ormocomp film on a glass substrate using an intermediate PDMS stamp in a UV-NIL replication step. The PDMS stamps were made in a casting procedure, where uncured PDMS was poured onto the FDTS coated silicon masters and cured in an oven for 3 h at 60 °C. The imprint procedure was carried out in an Obducat NIL at 10 bar hydrostatic pressure for 10 minutes at room temperature. The Ormocomp was cured through the glass using UV-light followed by removal of the PDMS stamp. This replication procedure leads to some rounding of sharp structural features present in the master, but the overall characteristics such as height and spacing are maintained in the replica.

The three types of surfaces scatter the light differently, which leads to different color in the transmitted light. This filtering effect is seen in Fig. 3.12a where both a picture of the directly transmitted light through one of the samples and the measured transmittance spectra are shown. The white lines in the colored image were made in the silicon master by scratching and used for navigation on the sample. The structures of type 1 have highest transmittance in the longer wavelengths, type 2 has a broad peak centered around 560 nm and type 3 has highest specular transmittance in the short wavelengths. The three spectra leads to an orange, green and blue color respectively.

In order to illustrate the possible use of this technique, a master was fabricated

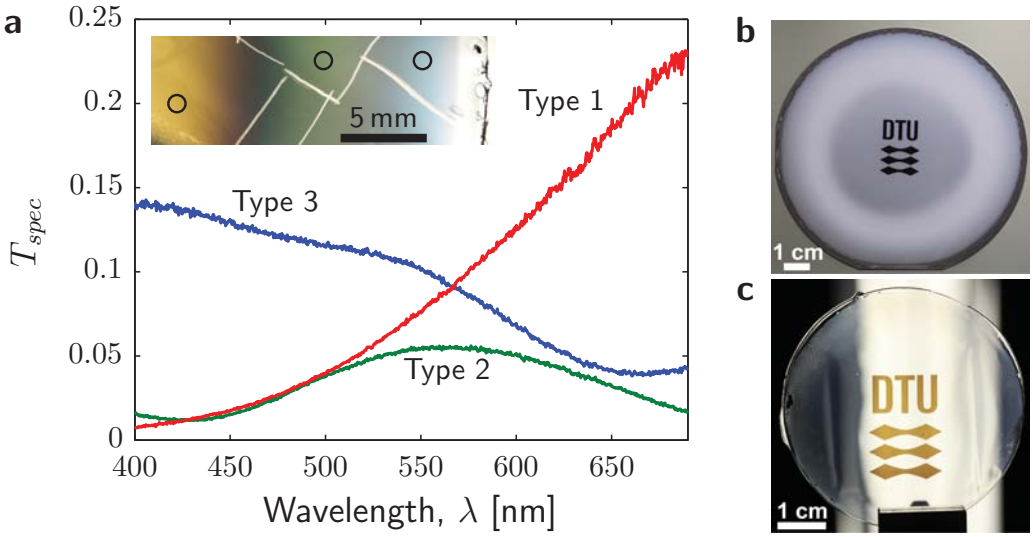

Figure 3.12: Transmittance spectra. **a)** Specular transmittance measured for the three types of replicated surface seen in Fig. 3.11b. Different scattering characteristics results in different colors in the specular transmitted light.**b)**Silicon master where the black silicon structures are removed outside the DTU logo using a isotropic dry etch and photolithography. **c)** Replica in ormocomp on glass as seen against a white light source. The colors only appears where there is structures in the surface.

where the structures after etching were removed using photo lithography and isotropic dry etching of the surface. In regions where the structures weren't protected by resist they were etched away again leaving an almost flat silicon surface. This master is seen in Fig. 3.12b. It is noteworthy how the structure, while scattering still behaves anti-reflective leading to the dark color of the DTU logo. In Fig. 3.12c is the replica seen against a white light source and the DTU logo becomes orange, while the flat part of the surface remains uncolored.

The effects were expected to be due to diffraction arising from the phase modulations of the wavefront as the light passes through the surface. In order to experimentally verify this, the structures of type 1 were investigated in more detail. Angle resolved measurements were performed and the surface topography was characterized with a high aspect ratio AFM-tip in order to compare the scattering results with predictions from topography and scalar diffraction. This is similar to what is done by Domine *et al.* [52].

An AFM image as used in the calculations is shown in Fig. 3.12a. The scanned area is $20 \times 20\,\mu m^2$ area with a resolution of 512×512 pixels. The data was recorded in tapping mode with a high aspect ratio tip with a full cone angle less than 10 degrees and a radius of curvature less than 10 nm. The surface plot illustrates how the topography consist of partly connected structures of sizes around 1 µm. The height profile $h(x, y)$ is used to calculate the phase shift $\Delta\phi(x, y) = \phi_{out} - \phi_{in}$ trough the surface region with total thickness $t = h_{max} - h_{min}$. Here it is assumed that the light enter from the polymer region which was the case in the measurements

$$\Delta\phi(x,y) = \frac{2\pi n}{\lambda_0} h(x,y) + \frac{2\pi}{\lambda_0}(t - h(x,y)) \quad = \frac{2\pi t}{\lambda_0} + \frac{2\pi(n-1)}{\lambda_0} h(x,y). \tag{3.41}$$

When inserted in Eq. (3.23) and (3.24) we get that the diffracted radiance is

$$L(\alpha,\beta) = \frac{{\lambda_0}^2}{A_s} \left| \mathcal{F}\left\{ \exp\left[\frac{2\pi(n-1)}{\lambda_0} h(\hat{x}', \hat{y}') \right] \right\} \right|^2, \tag{3.42}$$

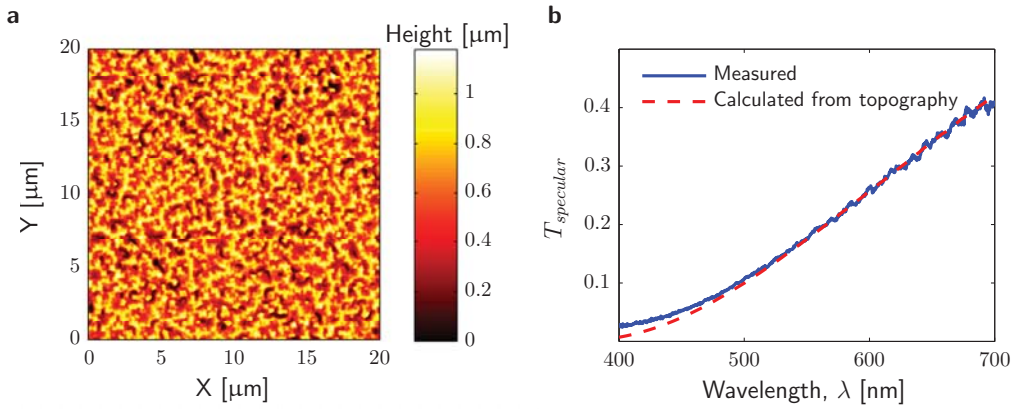

Figure 3.13: Specular transmittance from topography. a) AFM image used as input in diffraction calculations to calculated the scattering properties of the surface. The image is $20 \times 20\,\mu m^2$ and recorded with 512×512 pixels using a high aspect ratio tip in tapping mode. **b)** Comparison between experimentally measured specular transmittance and the calculated spectrum obtained from diffraction theory and surface topography.

where the constant term of the phase factor has been neglected since it has unity modulus. The Fourier transform was performed using the numerical `fft2` function in MATLAB, which computes the two dimensional discrete Fourier transform. In the discrete Fourier transform the resolution on the direction cosines axis is proportional to the side length of the scanned area with the AFM. The scan area of $20 \times 20\,\mu m^2$ was chosen in order to achieve proper resolution on both direction cosines in the Fourier space and on the topography in the real space.

The radiance is calculated for a number of wavelengths in the visible spectrum and for each wavelength the result is a map showing the diffraction pattern. The pixel with $\alpha = 0$ and $\beta = 0$ corresponds to the unscattered light, and is the specular transmitted light. In order to compare the value of the 'specular' pixel to the measured specular transmittance it should be normalized to the sum of all the pixels within the unit circle in the $\alpha\beta$-space. These corresponds to all the modes which propagate to the farfield while modes outside the unit circle corresponds to evanescent modes. This gives

$$T_{\text{spec}} = \frac{L(0,0)}{\sum\limits_{\alpha^2+\beta^2<1} L(\alpha,\beta)}. \tag{3.43}$$

This value gives the unscattered light relative to all transmitted light. In Fig. 3.13b this value, corrected for Fresnel reflection at the flat interface of the sample, is compared to the experimentally measured specular transmittance. The two are seen to correspond very well with a slight deviation at the lower wavelengths.

In the angle resolved scattering measurements the measured quantity is the intensity, so in order to compare the radiance should be scaled with $\cos\theta$. Again the strength of the modes are normalized to the sum of propagating modes which yields the two-dimensional normalized scattered intensity, which is also referred to as the angle resolved scattering, $\text{ARS}(\theta,\phi)$ [52, 53]

$$\text{ARS}(\theta,\phi) = \cos\theta \frac{L(\alpha,\beta)}{\sum_{\alpha^2+\beta^2<1} L(\alpha,\beta)}. \tag{3.44}$$

Consistent with the random nature of our structures we assume isotropic scattering. By averaging over the azimuthal angle ϕ, the full two-dimensional $\text{ARS}(\theta,\phi)$ can then conveniently be converted to a one-dimensional $\text{ARS}(\theta)$ which is comparable to the measured ARS.

In Fig. 3.14 have the experimentally obtained scattering data and the data calculated from the surface topography been plotted as a scattering probability, which gives the probability of light is scattered to the given angle. The data are normalized such that integrating over all scattering angles equals the transmission haze, H_T, where $H_T = 1 - T_{spec}$. The surface plots in Fig. 3.14a and Fig. 3.14b resembles each other very well. In Fig. 3.14c the scattering probabilities are compared for specific wavelengths.

It has been seen that the effect may be described well by simple diffraction theory. Also it has been illustrated that color filters of different colors may be produced based on random texturing using self-masked dry etching. Despite the ability to define e.g. a DTU logo the design freedom is limited as more process development is needed in order to achieve the different colors over full wafers at will. Here only the orange color was produced in large areas and it was chosen not to proceed on developing processes, which produce the other colors on full wafers.

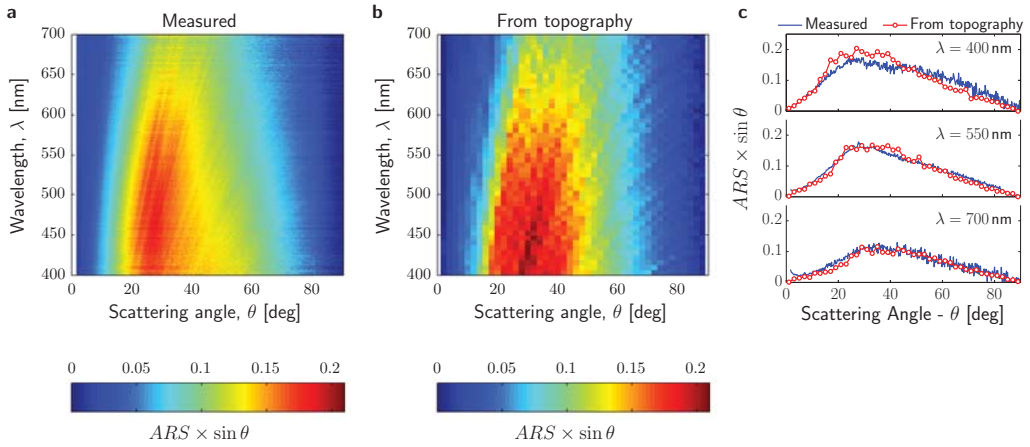

Figure 3.14: Angle resolved scattering. a) Experimentally measured scattering probabilities for transmitted light using the setup described in Sec. 2.2.2 with normal incident light. **b)** Scattering probability calculated from surface topography measured with AFM. Calculated using scalar diffraction theory. **c)** Selected wavelengths where the experimental and calculated scattering probabilities are compared.

3.3.3 Diffraction gratings on surfaces and foils

As shown above in Sec. 3.2 diffraction gratings, often with a metallic coating to enhance the effect, may be used as colorful elements which change color upon change in illumination or observation angle as given by the diffraction equation, Eq.(3.25).

Despite the low reflectance of polymers it is possible to obtain clear color effects with standard diffraction gratings if other sources of light from the sample towards the observer is limited. This is the case if the gratings are defined in black base polymer, where there is very limited diffuse reflectance from the bulk and no transmitted light from the back. In the opposite case of white pigment the reflections from the gratings are competing with the large diffuse reflectance from the bulk. The argument is the same for the dark chocolate of Fig.3.6. With the limited contributions from elsewhere, a grating with diffraction efficiency of for example 1% in one of the reflected 1st orders for a given wavelength can lead to a bright color experience. This is due to the fact that light reflected in the specific direction of the observer has a very narrow spectral distribution and in combination with the black pigment this leads to very chromatic colors, which are experienced as clear and pure by the human brain.

This was utilized in a demonstrator pattern, which had the purpose of demonstrating the full value chain within the NanoPlast project, from design to hand-over to industrial partners, who fabricated master molds in steel and conducted injection molding at industrial facilities. The basic idea was to create a structure which would function as glitter in the surface of the black polymer no matter the observation angle. This was obtained by combining diffraction gratings of different periods and orientations and combining them in a pixel pattern. The periods were chosen to obtain few orders with high diffraction efficiencies ($\Lambda = 600 - 1400\,\text{nm}$). The same argument led to the choice of 1D gratings over 2D gratings. The simple design criterion for high efficiency for a binary grating is that a π-phase shift between light reflected on the bottom and top surfaces of the grating. For normal incidence this is achieved with a height of $\lambda_0/4$. This can of course not be fulfilled in the full visible

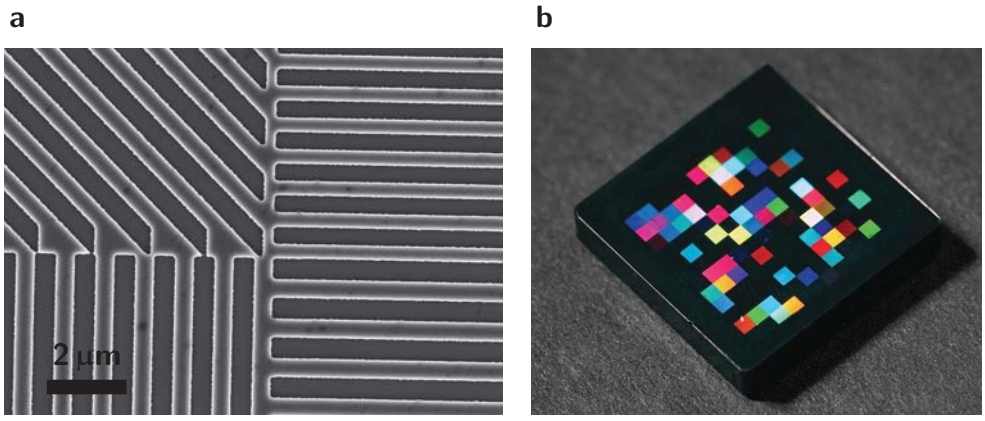

Figure 3.15: Glitter effect from diffraction gratings. a) SEM image of the intersection between four pixels with gratings of different periods and orientation. **b)** Diffraction gratings with different periods and orientations utilized to create a glitter effect in one of the NanoPlast demonstrators. The individual pixels change color and "turns" on and off when seen under changing angles.

spectrum and for all angles at the same time, but with a grating height of 135 nm and a filling fraction of 50%, it was found from RCWA calculations, that the gratings are efficient for many different viewing geometries and wavelengths.

In Fig. 3.15a is the intersection between four different pixels of the silicon master of the first small scale demonstrator shown. The line gratings were in this case written using standard EBL at high current (20 nA) and shot pitch (11 nm), which is the explanation for the rough edges. After verification of the optical effect a design for a DUV-stepper reticle was handed over to the industrial partners, who conducted the following processing to reach the injection molded demonstrator shown in Fig.3.15b.

While the scientific progress related to this type of structure is limited, it has had great value for the participants of the project. It also demonstrates the limitation of surface structures which comply with the replication criterion. The colors are only clear due to fact that other wavelength are redirected to other angles making the structure appear differently from different angles. Or stated differently; it is not possible to create angle-intensive colors using these gratings. The following is an attempt to get close to obtaining colors which look the same no matter the observation angle. This is done by utilizing more than just the front surface reflection. The work is reported in Paper E.

The work concerns gratings in the top surface of thick transparent foils. Here foil refers to a slab of polymer with parallel front and back surfaces and thick refers to the foil thickness relative to the coherence length of the light. If the thickness is much longer than the coherence length of the light, interference between reflections from front and back can be neglected and what happens on each interface may be treated separately. The thickness condition is fulfilled for most white light sources and foils which are thick enough for handling.

The basic idea is to utilize the total internal reflection on the backside of the foil to achieve high overall reflectance for some wavelengths. A numerical model is setup with the assumptions stated above. The interactions of the light with the grating in the front side of the foil are calculated using RCWA, while the interactions with

the backside is calculated using the Fresnel coefficients. The foil is assumed to be transparent so no absorption or scattering take place. As mentioned the light is treated as rays between the surfaces with directions given by the diffraction equation. Light is send in from the front side (here at normal incidence) and is reflected back and forth until escaping the foil either as reflected or transmitted light. In the presented calculations the grating is assumed to have a filling fraction of 50% and a height which is half the period, $h = \Lambda/2$ and is furthermore assumed to cover a large area.

In Fig. 3.16a the result of a calculation where the reflectance as function of the normalized wavelength, λ/Λ and the angle of observation is shown. In Fig. 3.16b is the zero order reflectance shown separately. Like the case of standard reflectance gratings there are multiple discrete orders in the reflected light. For wavelength longer than the period there is only zero'th order, while $\pm 1^{st}$ and $\pm 2^{nd}$ orders show up for shorter wavelengths. What is special is the absolute values of the reflectance which for the zero'th order peaks with a value just below 0.4 for wavelengths just higher than the period. This is approximately 10 times the reflectance of a single interface at normal incidence. In addition to the high reflectance the peak is very steep allowing for chromatic colors.

A more detailed analysis illustrate the mechanism of this high reflectance. The ray paths of some of the relevant orders are shown in Fig. 3.17a. As the light interact with the grating multiple transmitted orders exist if $\lambda < n\Lambda$, where $n = 1.5$ is the refractive index of the foil. These downward fluxes are denoted 0a, 1a and their contributions normalized to the incident light are shown in Fig. 3.17b. The different regimes where different number of orders exist in the bulk are seen. At the back side the order are reflected with reflectance R0, R1 etc. depending on the order (Fig. 3.17c). The upward fluxes after this interaction, (0b, 1b etc.) are shown in Fig. 3.17d, which reveals that the major part of the energy is carried by the $\pm 1^{st}$ orders. When arriving at the top surface the grating allows for out-coupling of the

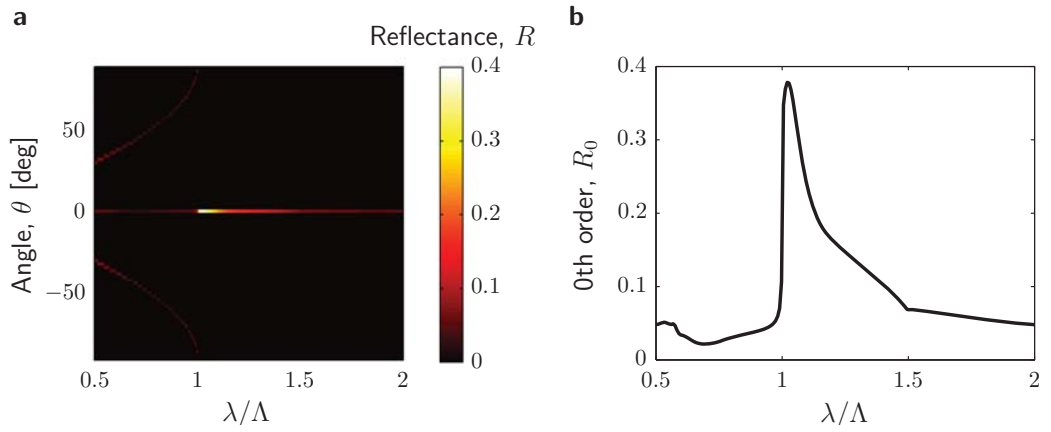

Figure 3.16: Reflectance from grating on foil a) Calculated reflectance as function observation angle for light at normal incidence. The line grating has a filling fraction of 50% and a height of $\Lambda/2$. Notice the absolute values of the reflectance is approximately an order of magnitude higher than that of a single interface. **b)** The zero order reflectance from the system. Identical to the spectrum in a scattering angle of $\theta = 0$ in panel a.

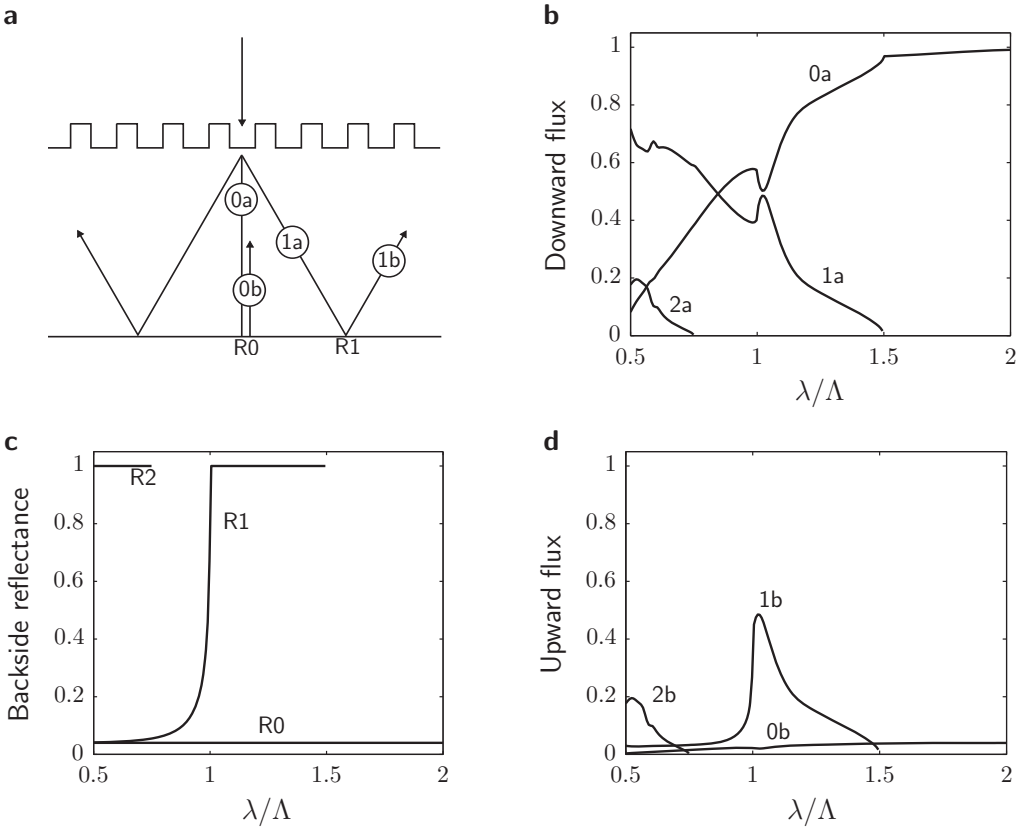

Figure 3.17: Mechanism for high reflectance in foil. a) Sketch of the relevant orders/fluxes in the foil. The numbers relate to the diffraction order. All downward fluxes a denoted with an a, while upward fluxes are denoted with a b. **b)** Downward fluxes after first interaction with the grating. The curve denoted 1a represents the sum of the $\pm 1^{st}$ orders. Likewise for 2a. The curves are only plotted in wavelength regions where they exist. **c)** Fresnel reflectance on the backside of the different order as function of normalized wavelength λ/Λ. The curves are calculated from the internal Fresnel coefficients and the diffraction equation. **d)** The upward flux after one interaction with the backside, given by the product of the curves in panel b and c. The 'color' information is mainly carried by $\pm 1^{st}$ orders.

light to the zero'th reflected order leading to the strong peak. The peak in the first order upward flux arise from a combination of high efficiency in the transmitted first order from the grating (1a) and high reflectance at the back. Such a grating may therefore used as a colored mirror with high reflectance. The iridescence is however still present.

In order to exploit the high reflectance a design has been proposed where the high intensity carried by the 1b fluxes rather than being send to the zero'th reflected order is scattered to many angles, thereby enabling observation of the color from all directions upon normal incident light. This is done by replacing parts of the front surface with diffuser regions designed to scatter the light. The principle is shown in Fig. 3.18a. The grating and diffuser regions are positioned in an alternating pattern. The width of each region is supposed to be designed such that the first

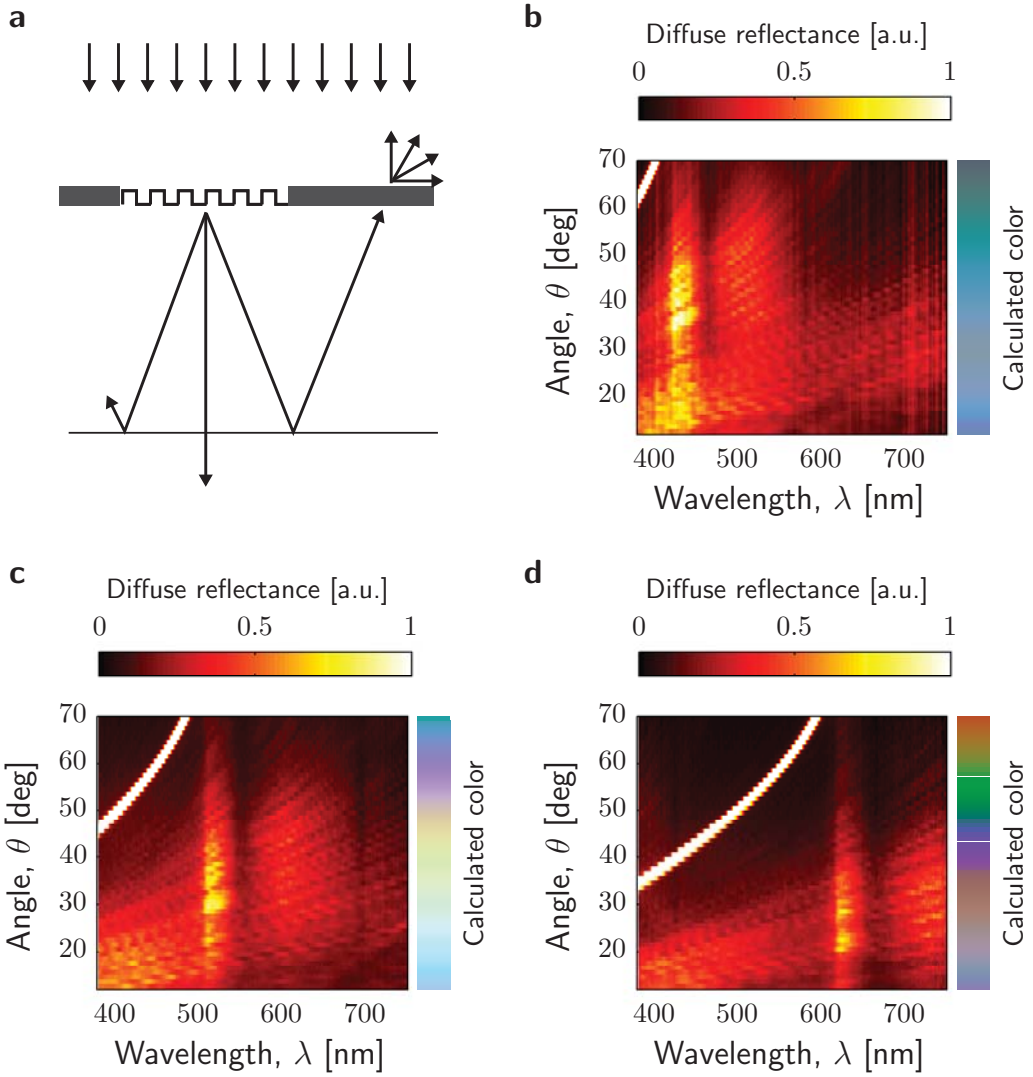

Figure 3.18: Concept and experimental result for colored diffuser in foil. **a)** Schematic sketch of the concept. The surface is split in diffuser and grating regions. The $\pm 1^{st}$ from the gratings are scattered on the diffuser region enabling outcoupling to a number of angles. **b)** Measured diffuse reflectance for blue sample with grating period of 425 nm and randomized binary diffuser regions. The calculated colors of the different scattering angles are shown next to the plot. The color scale does not included the diffraction peaks. **c)** Similar as panel b, but with $\Lambda = 505\,\text{nm}$ **d)** Similar as panel b, but with $\Lambda = 615\,\text{nm}$

order of wavelength $\lambda/\Lambda = 1.05$ from the grating region upon reflection on the back side hits the diffuser regions, such that the wavelengths with highest reflectance is diffusely transmitted through the top surface. In the experimental realization this was also intended, however a design error resulted in significant deviation from the optimal width. The fabricated regions were 110 µm wide, while the optimal width was 180 µm for the case of the 100 µm thick Topas 6015 foils used in the study. The desired effect is however still illustrated in the experiments as more than half of the

light hits the diffuser as intended.

The diffusers were made as binary diffusers made by a random line pattern [54]. The patterns were generated in MATLAB by insertion of 400 nm wide lines in random positions until the filling fraction was 50% on average. Each of the diffuser regions were different in terms of random pattern. This diffractive diffuser design was chosen over refractive elements such as micro lens arrays [55] in order to be able to fabricate the test samples in one lithography step and a single subsequent etch. Three different colors were tested (red, green and blue) and therefore the diffraction efficiency should be high over a large range of wavelengths. The criterion is a π-phase shift of the light going through the different parts of the gratings and on this basis the depth of the gratings was chosen to be 350 nm in the experimental realization.

The master mold was fabricated using EBL and dry etching. Three areas with the grating-diffuser design were fabricated with an area of $3 \times 3\,\mathrm{mm}^2$. The grating periods of the three areas were 425 nm, 505 nm, and 615 nm to obtain blue, green and red diffusive colors.

The replication into polymer foils was done using thermal embossing as described in Sec. 2.1.3 at 190 °C and 15 kN for 30 minutes. The replicas were fully imprinted (measured by AFM).

The optical effect of the sample was characterized using the angle resolved measurement setup. Here the reflected intensity was measured at varying angle for constant incidence angle (normal incidence). The results for the three areas are shown in Fig. 3.18b-d. For each of the scattering angles the color is calculated from the spectrum by use of CIE 1931 2 degree observer and the standard D65 light source, and shown to the right of each plot. The basic principle works despite the non-optimal width of the regions. It is seen that there is increased intensity at wavelengths just above the grating periods for a large angle interval as intended. There are however disturbing effects. The main problem is the 1st reflected diffraction order, which completely dominates the spectra at higher angles. In the plots do the colors scale not include the peaks of the diffraction as they are significantly stronger than the diffuse light. The reflected 1st order is present for wavelengths shorter than the period of the grating on this effect does therefore mainly disturb the green and red samples. Again the angle insensitive colors is not accomplished.

3.4 Discussion of practical applicability

The color effects demonstrated above are all in line with the basic premisses of the replication constraint and are possible to utilize in an injection molding setting. The effects related to the grating behavior in foils is perhaps more relevant in the context of roll-2-roll replication [56], where the master is a cylindrical shaped roll and the substrate is a polymer foil, which is imprinted as it continuously passes by the master roll by use of thermal or UV imprinting. The throughput of this method is extremely high.

There are however a number of limitations concerning the presented structures which are very hard to work around and limits the applications significantly. First of all the obtainable effects are not by any means capable of replacing inks or pigments in the production of consumer products as the preferred coloration method. It seems that under the replication constraint the produced effects are either weak or with very high degree of iridescence. The latter may of cause be seen as an advantage as

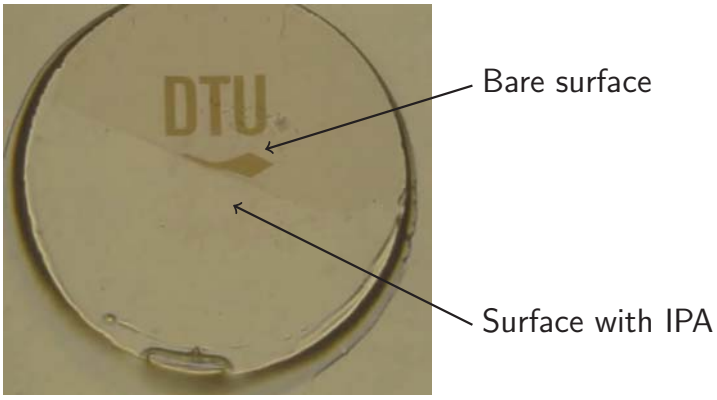

Figure 3.19: Index matching. Sample of Sec. 3.3.2 projected onto a screen thereby illustrating the color filter behavior. The upper part is bare with the structures surrounded by air, while the lower part is covered with a clear liquid (IPA). The effect disappears due to index matching.

it offers possibilities for decorative effects, which are not available using standard pigmentation.

Another problem, which has not been discussed until this point, is the mechanical durability of the proposed surfaces. Since the structures are defined in the very surface of the plastic parts any wear of the surface will completely remove the effects. This has also been seen for the shown surfaces if handled without care. The simple solution would be to protect the structures with a protective coating, however typical coatings are based on polymers and do therefore match the refractive index of the polymer in which the structures are defined. Since the diffraction effects are based on index contrast the color effects will disappear. This is illustrated in Fig. 3.19 where one of the color filters based on scattering on random surface structures (Sec. 3.3.2) is projected onto a wall with a overhead projector. The sample is covered in isopropyl alcohol (IPA) in which case no logo seen on the screen. As the IPA is blown away from the sample the color re-appears since scattering of the mainly the blue light does now take place. In the picture the lower half is covered with IPA. It worth noticing that IPA has a refractive index of 1.38 [57] so it does not match the index of the substrate perfectly.

Another solution is to incorporate higher structures in the surface which acts as protective shield for the functional structures. This concept has recently been demonstrated for hydrophobic surfaces by Huovinen *et al.* [58], where the effects on static and dynamic loading were investigated. In the case of optical surfaces it is needed that these extra structures do not alter the optical effects or introduce new ones. Also it does not solve the problem of deposition of grease from fingers. A greasy finger on the sample will have same index matching properties as demonstrated above and the effect will disappear.

While these issues with handling is a problem for the use in for example toys, there might be application where the surfaces are untouched, for example on the backside of transparent polymer parts mounted in fixed positions.

One might also turn this sensitivity to handling into a positive feature for use in security applications where easy verification of a package or something else being

unopened or untouched. The effects are visible to the naked eye so the verification is simply manual inspecting and if touched the effects are destroyed on not possible to recover by cleaning or re-painting.

In conclusion does the original idea of NanoPlast not seem possible, where pigments are solely replaced by replication based surface structures. However the surfaces my be used for other applications, where the iridescence and low mechanical strength may be advantageous.

Chapter 4

Metal-coated nanostructured polymer surfaces

Color effects from pure plastic have been described in the previous chapter and the conclusion was that bright angle-insensitive colors as replacement for inks and pigments are not achievable from polymer surfaces under the assumption of replication-based fabrication. In this chapter the possibilities for production of structural colors using nanostructured polymer surfaces in combination with a small amount of post processing are investigated. Specifically the effects of an ultra thin metal layer are considered.

Polished metal surfaces do in general appear shiny as they reflect a large amount of the incident light. The immediate benefit of this in relation to the work described in the previous chapters is the increased amount of light, which may be manipulated for the purpose of reflective colors. A thin uniform layer of metal on e.g. a structure with reflective diffractive elements like in Fig. 3.15 would utilize the same optical principle, but with much higher overall reflectance. This also allows for a protective coating without having problems with index matching as described in Sec. 3.4.

It is however other effects emerging from the optical properties of metals and metallic nanostructures, which are utilized in this chapter. The concept of localized surface plasmon resonances (LSPR) is explored in order to produce colors, which come much closer to the goal of bright angle insensitive colors. The findings of the chapter have been reported in Paper D.

4.1 Background

4.1.1 Optical properties of metals

Opposite polymers, metals posses the ability to conduct current due to the existence of free electrons, which are not bound to the atomic core [59]. The free electrons influence the optical response significantly since they are allowed to follow the optical field with no restoring force. The metal may therefore be seen as a plasma with negative charge, which is free to move and an equally sized positive charge which is fixed in space. This model is known as the Drude-model. The optical response of the plasma is what is utilized in the following to create bright colors, when depositing metal on nanostructured plastic.

First we describe the reflectance characteristics of the unstructured metal, by assuming the Drude-model. By writing up the equation of motion for the electrons and relating this to Eq. (3.7) it can be shown that the relative permittivity is given by [60]

$$\epsilon_r = 1 - \frac{{\omega_p}^2}{\omega^2 + \mathrm{i}\gamma\omega}, \tag{4.1}$$

where γ is damping coefficient, due to collisions of the electron on the stationary positive ions and ω_p is the plasma frequency given by

$$\omega_p = \sqrt{\frac{Ne^2}{\epsilon_0 m}}, \tag{4.2}$$

where m is the free electron mass and N is the density of free electrons calculated from the number of valence electrons and the density of atoms of the metal in question. e is the electron charge. By assuming negligible damping and calculating the normal incidence reflectivity using the Drude permittivity and the Fresnel equations, one gets that all light is reflected at frequencies lower than the plasma frequency, and that the reflectivity drops for frequencies higher than the plasma frequency. With plasma frequencies lying in the UV for most metals this leads to very high reflectivity in the visible spectrum. This is illustrated by e.g. silver and aluminum which are both widely used as mirrors due to their high reflectance in the full visible spectrum. This property of metals is a very desirable starting point for creating bright colors working in reflection opposite to what was discussed for the low reflectance of polymers in Sec. 3.1.2.

For some metals other effects arising from the electronic structure is needed to explain their reflectance behavior in the visible spectrum. Damping and interband transitions accounts for a large part of the discrepancies between the Drude-model and the behavior of a metal such as gold [61]. Gold has an interband transition threshold lying in the middle of the visible spectrum, leading to large absorption for wavelengths shorter than the threshold and reduced reflectivity as consequence. Hence the characteristic 'golden' color. A similar effect is present in cobber and silver. For silver however the threshold lies in the UV and does therefore not affect the properties relevant for appearance to humans. For aluminum the interband transitions are possible throughout entire visible spectrum, but do mainly take place in a narrow wavelength interval in the near-infrared. The transition probability is very low in the visible and the interband transitions therefore only slightly affects the reflectivity. When performing simulations the permittivity is based on empirical values which include these effects.

4.1.2 Localized surface plasmons

As briefly introduced in Sec. 1.2 metallic nanoparticles give rise to resonant interaction with incident light, such that certain wavelengths are absorbed more than others and certain wavelengths are scattered more than others.

The reason for the resonant behavior is that the motion of the free electrons is limited by the geometrical shape of the metal e.g. a sphere or disk. When the electron cloud moves due to the electric field, charge builds up at the surfaces of the particle. Positive charge is accumulated at the surface in the direction of the

electric field and negative charge on the opposite surface. This leads to a restoring force and the system starts to behave like a mass-spring system with a characteristic resonance frequency. At resonance the electric field drives the electron cloud of the particle at its natural frequency leading to much larger separation of charges than at other frequencies. This is characterized by the polarizability $\alpha(\omega)$, which relates the electric field and the dipole moment, $\mathbf{p}$ (for the case of dipolar resonances), such that

$$\mathbf{p} = \epsilon_0 \epsilon_{coat} \alpha \mathbf{E} \tag{4.3}$$

with ϵ_{coat} being the dielectric constant of the material surrounding the particle. The polarizability can be found by solving the full electrodynamic problem of an electric field impinging on a particle. If the particle is very small compared to wavelength the quasi-static approximation can be applied, where the electric field is assumed to be constant in space within the particle. For a metallic sphere, with dielectic constant ϵ_m this leads to a size-independent resonance position as the polarizability may be found to be [60]

$$\alpha_{sphere} = 4\pi r^3 \frac{\epsilon_m - \epsilon_{coat}}{\epsilon_m + 2\epsilon_{coat}}, \tag{4.4}$$

where r is the sphere radius. The resonance of this expression is when the real part of ϵ_m is opposite in sign and equals twice the value of ϵ_{coat}. Therefore the resonance position is only determined by the dispersion of the involved materials. This changes when going to aspherical particles with aspect ratios different from 1. For example the oblate spheroid for which the quasi-static approximation leads to a polarizability given by [62]

$$\alpha_{spheroid} = \frac{\pi D^2 t}{6} \frac{\epsilon_m - \epsilon_{coat}}{\epsilon_{coat} + L(\epsilon_m - \epsilon_{coat})}, \tag{4.5}$$

where D is the long axis of the oblate spheroid (diameter) and t is the short axis (thickness). L is a geometrical factor which is dependent on the ratio between D and t and for the electric field being aligned along the major axis is given by [60]

$$L_D = \frac{D^2 t}{2} \int_0^\infty \frac{1}{(D^2 + q)\sqrt{(q + D^2)^2 (q + t^2)}} dq. \tag{4.6}$$

Here the resonance position depends on both the material parameters and the aspect ratio and it is possible to tune the resonance by varying e.g. D. The oblate spheroid is interesting since it approximates the response of disks with diameter D and thickness t well [62]. Disk are used below in the proposed surface.

The effects on the farfield are given by the extinction cross section and scattering cross section which depend on the imaginary part and the magnitude of the polarizability respectively

$$C_{ext} = \frac{k^4}{6\pi} |\alpha|^2 \tag{4.7}$$

$$C_{sca} = k \mathrm{Im}[\alpha]. \tag{4.8}$$

It should be emphasized that Eqs. (4.4)-(4.5) only are valid when the particles are much smaller than the wavelength of the light. For larger particles effects such

as radiation damping, dynamic depolarization and retardation should be taken into account. These effects leads to redshift of the resonance of spherical particles with increasing radius, which therefore in fact do possess size-dependent resonances opposite what is predicted from Eq. (4.4). A correction to the oblate spheroid polarizability, which includes the first two effects is given below

$$\alpha'_{spheroid} = \alpha'_{spheroid}\left[1 - i\frac{k^3\alpha_{spheriod}}{6\pi} - \frac{k^2\alpha_{spheriod}}{2\pi D}\right]^{-1}, \tag{4.9}$$

where k is the wavevector of the light in the incident medium. The extension cross section of oblate spheroids of aluminum embedded in a material with refractive index 1.5 with constant thickness $t = 20\,\text{nm}$ and varying diameter has been calculated using Eqs. (4.7) and (4.9) and plotted in Fig. 4.1.

The diameter has been varied from 50 nm to 110 nm in increments of 10 nm. This size range is chosen since this is the relevant size range of the surface which will be presented in the following. It is seen that by changing the diameter the aspect ratio and therefore also the resonance position is changed. This illustrates some of the possibilities for tunability utilizing LSPR.

4.1.3 Surface plasmon polaritons

Under the right conditions a metal-dielectric interface supports surface waves known as surface plasmons polaritions (SPPs), which are propagating and confined surface waves manifested as oscillations in the plasma at the surface of the metal with an exponentially decaying field away from the interface in both the metal and the dielectric. The condition for existence of SPPs is that the interface is between a material with real positive dielectric constant (e.g. polymer or air) and a material with negative real part of the dielectric constant (e.g. metals below the plasma frequency). If the dielectric constant of the dielectric material is denoted ϵ_1 and the dielectric constant of the metal is denoted ϵ_m the dispersion relation for a SPP at a

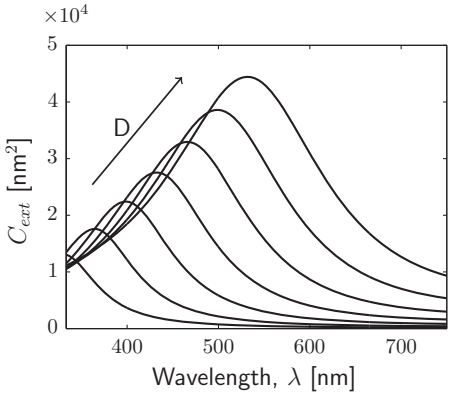

Figure 4.1: Exctinction cross section of oblate aluminum spheriods. The extinction cross section as calculated from Eqs. (4.7) and (4.9) for oblate aluminum spheroids with thickness $t = 20\,\text{nm}$ and increasing diameter, D, as indicated by the arrow. The diameters are 50-110 nm in increments of 10 nm. The resonance position is seen to increase with D.

single interface can be found to be

$$\beta = \frac{\omega}{c_0}\sqrt{\frac{\epsilon_1\epsilon_m}{\epsilon_1+\epsilon_m}}, \tag{4.10}$$

where β is the in-plane wavenumber and c_0 is the vacuum speed of light. The dispersion relation is plotted in Fig. 4.2 for a lossless Drude metal with interface to either air ($n = 1$) or polymer ($n = 1.5$) along with the linear dispersion relations of the dielectric material (light lines). In order to couple light from free space to SPPs it is necessary to match both energy and momentum and from Fig. 4.2 it is seen that there is no overlap between the light line and the corresponding SPP mode. This has the consequence that it is not possible to couple directly to the SPP mode of a flat interface without any mechanism to account for the phase matching at the surface. Here two methods will be discussed: Grating assisted coupling, relevant to the way free space light couples to the proposed surface and coupling using a subwavelength aperture, which is relevant for the near field measurements presented later.

In grating assisted coupling the missing momentum, Δk is supplied by the grating in a similar fashion to what is given by the diffraction equation where the wavevectors of the different diffraction orders are seperated with equal amount $\Delta k = 2\pi m/\Lambda$. In order to achieve grating coupling the in-plane wavevector component of the incoming light and the momentum provided by the grating should add up to the β of given by the SPP dispersion relation. The condition for grating coupling is therefore given by

$$\beta = k\sin\theta_i + \frac{2\pi m}{\Lambda}, \qquad m = 0, \pm1, \pm2, ... \tag{4.11}$$

where k is the wavenumber of the incident light and Λ is the period of the grating. One should notice that the coupling efficiency depends on particular grating.

When light is scattered by a subwavelength particle or is limited by a subwavelength aparture, it gains wavevector components in a continuum, which are higher than the free space wavevector [60]. This allows a part of the light to couple to the SPP since it match the wavevector matches β. Using this method it possible to

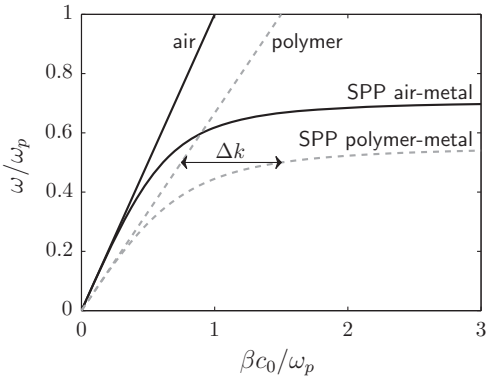

Figure 4.2: SPP dispersion of loss less Drude metal. The SPP dispersion relation, Eq. (4.10) for interface between a loss less Drude metal and air and polymer respectively. The 'lightlines' of the free propagation in air and polymer is also shown. The difference in momentum Δk, which must be supplied to enable coupling from propagation in polymer to the SPP.

approach a very sharp fiber to the surface of a metal and excite SPPs in all directions away from the tip. Likewise it is possible to detect the existence of of an SPP with fiber probe if there is an overlap with the evanescent field, which thereby is able to couple to the guided modes of the fiber.

In Eq. 4.10 and Fig. 4.2 the dispersion of a single interface was presented. The design which will be presented in the following comprises a very thin metallic film rather than a semi-infinite metal. For a metallic film the evenescent field may extend beyond the thickness of the metal and the dispersion relation is modified accordingly. For the general case of a metallic thin film sandwiched between two dielectric materials with real positive permittivities ϵ_1 and ϵ_2 the dispersion relation is given by

$$\exp(-2k_m t) = \frac{k_m/\epsilon_m + k_1/\epsilon_1}{k_m/\epsilon_m - k_1/\epsilon_1} \cdot \frac{k_m/\epsilon_m + k_2/\epsilon_2}{k_m/\epsilon_m - k_2/\epsilon_2}, \tag{4.12}$$

where t is the thickness of the metal film. The qauntities k_m, k_1 and k_2 are the z-components of the wavevector in the metal, region 1 and region 2 respectively. In terms of free space wavevector and β are they given by [60]

$$k_m{}^2 = \beta^2 - k_0{}^2\epsilon_m \tag{4.13}$$

$$k_1{}^2 = \beta^2 - k_0{}^2\epsilon_1 \tag{4.14}$$

$$k_2{}^2 = \beta^2 - k_0{}^2\epsilon_2. \tag{4.15}$$

For the general case of a lossy metal and different materials above and below the film, this dispersion relation is difficult to solve. It may however be done using numerical methods. For the case of an embedded film with the same refractive index on both sides it reduced to the following two solutions

$$\tanh\frac{k_m t}{2} = \frac{-k_1\epsilon_m}{k_m\epsilon_1} \qquad \text{odd} \tag{4.16}$$

$$\tanh\frac{k_m t}{2} = \frac{-k_m\epsilon_1}{k_1\epsilon_m} \qquad \text{even.} \tag{4.17}$$

The two modes arise due to hybridization between the modes on each surface as they interact when the fields overlap. The two modes have different electric field profiles. Odd and even refers to the component of the electric field in the direction of the propagation. This means that for the odd mode this component of the field is anti-symmetric around the center of the film and for the even mode the field is symmetric around the film. The fields inside the film is higher for the even mode, which leads to higher loss and lower propagation length. The odd mode has higher frequency than the even mode and splitting in energy depends on the thickness of the film and for thin films, e.g. 20 nm this splitting is significant.

4.2 Previous work

In the recent years a lot of work on plasmonic colors have been done within transmission color filters however recently also filters working in reflection have received increased attention. Below are some of the most interesting results presented.

4.2.1 Transmission filters

Many transmission color filters are based on the extraordinary transmission of light through nanometer sized holes in metal films as discovered by Ebbesen et al. [63]. An example is seen in Fig. 4.3a, where periodic arrays of holes in a silver film only allows a narrow band of wavelengths to pass thereby creating effective color filters [64]. Only some of the holes are milled all the way through the film leading to the ability to define letters. The effect is based on coupling to surface plasmons on one side of the film, waveguiding of the surface plasmon through the holes and re-emission in the forward direction on the backside of the films. The two colors are due to two different periods and therefore different wavelengths which can couple to SPP. This effect may also be fabricated using other metals such as aluminum [65, 66]. This is the case in Fig. 4.3b, where the influence of the hole shape is also seen investigated.

Other concepts such as metal-insulator-metal (MIM) nanoresonators have also been used to create transmission filtering [67] through the resonant coupling from free space light to surface plasmon modes and back to free space. This is illustrated in Fig. 4.3c.

4.2.2 Reflection filters

Color filters involving metals are not always working by means of plasmon excitation. Recently Kats *et al.* demonstrated bright colors upon deposition of an absorbing dielectric (Ge) on a gold surface [68, 69]. The mechanism is based on single layer interference and due to a large phase-shift at the gold-dielectric interface and high refractive index of the films the color may be created and tuned by deposition of films of few nanometer in thickness.

In Fig. 4.4a is an example shown, which utilizes confined cavity modes in periodic slits to obtain colors in reflection due to high absorption at the resonance wavelength of the cavity [70]. This was proposed by Wu *et al.* and is fabricated by deposition of a silver film on a pre-patterned glass substrate with high narrow ridges each defining

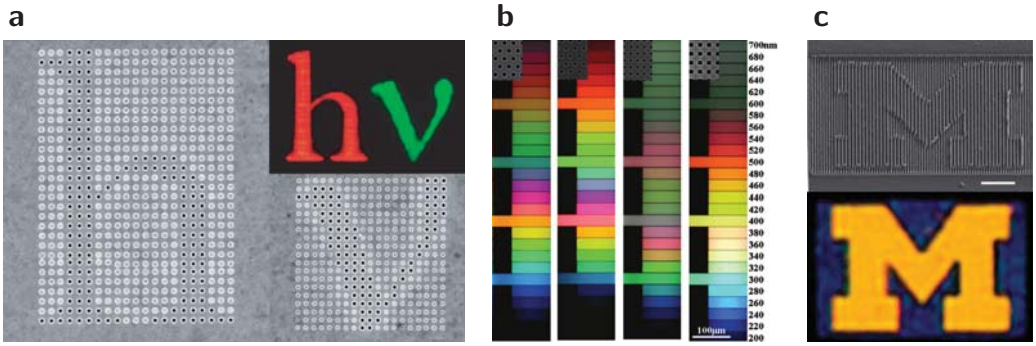

Figure 4.3: Examples of plasmonic transmission color filters. **a)** Transmission color filter in hole array in silver film due to the coupling to SPP and waveguiding through the holes. The periods of the red and green are 550 nm and 450 nm respectively. From Genet and Ebbesen [64]. **b)** Same mechnism as in panel a, but with an aluminum film with holes of different shapes. From Inoue *et al.*[66]. **c)** Color filtering based on a layered plasmonic cavity resonator arranged in lines. From Xu *et al.* [67]

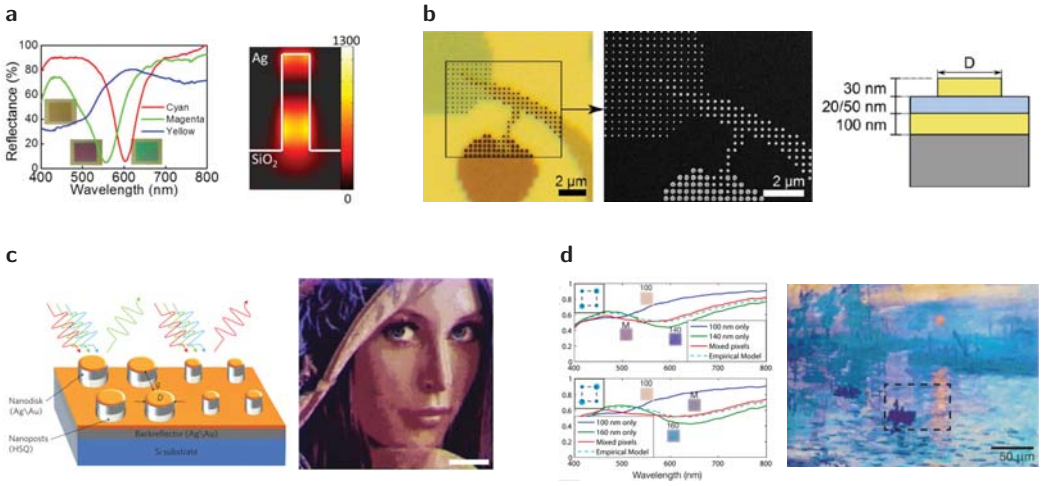

Figure 4.4: Examples of plasmonic reflection color filters. a) Colors produced by resonant interaction with glass-filled silver cavities. From Wu *et al.* [70]. **b)** Color from gap-plasmon resonances between gold disks distanced from a gold film. From Roberts *et al.* [71]. **c)** Disks of chromium-silver-gold which are created by deposition on pillar arrays. From Kumar *et al.* [72].**d)** Similar as panel c, but with aluminum as metal. Multiple disk sizes are combined to yield an extended color palette. From Tan *et al* [73].

a cavity sourounded by metal. The angular sensitivity of the structure is low due to the confined nature of the modes inside the cavities. Since it is based on line gratings the effect is highly polarization dependent.

Roberts *et al.* demonstrated subwavelength color definition by use of gold nano disks arranged in a periodic pattern (340 nm in period) on top of a gold film and with a glass spacer with the thickness of few tenths of nanometers [71]. This is illustrated in Fig. 4.4b. The effect is due to gap-plasmon resonances existing in the gap between the disk and the gold layer. The resonance condition is dependent on disk size and may therefore be tuned. Furthermore it was demonstrated how to protect the surface with a thin layer of polymer with only a slight modification of the colors as result. The small change is due to the fact that the mode mainly exists in below the disk.

Kumar *et al.* demonstrated color printing beyond the diffraction limit [72] by deposition of a chromium-silver-gold metal stack on top of 95 nm high pillars arrays written in negative e-beam resist on a silicon substrate. In this way disks composed of the given metal stack are created which leads to LSPR. Different pillar sizes and distances lead to different colors in reflection. They were able to draw the picture shown in Fig. 4.4c using the method. The method proposed in this thesis is inspired by this work, but is different in some important aspects.

Recently a follow-up paper [73] from the same group came out proposing the use of aluminum and an extension of the color palette by combining pillars of different sizes together[1]. The substrate was again silicon and the image in Fig. 4.4d was drawn with this extended pallette. One should notice the reflectance curves, which are also given here. The contrast between high and low reflectance regions of the spectra

[1]This paper by Tan *et al.* was submitted within 3 days of the submission of Paper D of this work.

seem to be very low, which should lead to very vague colors.

Also Lochbihler *et al.* have proposed structures relying on deposition of aluminum on prefabricated pillars both as a single aluminum film [74] and as an metal-dielectric-metal stack [75]. Here were the pillars very high (250 nm).

Methods which do not include the expensive nano-lithography may also be used to create color. By doing the proper annealing of thin gold films the gold agglomerate in clusters which posses characteristic absorption properties depending on their size and arrangement. This was demonstrated by Yan *et al.* for gold films on silicon [76].

4.3 Design considerations

Below is the proposed surface described along with the arguments for the choice of geometry and materials.

4.3.1 Basic design

As discussed above it is possible to limit the size of metal particles and thereby create the strong wavelength dependent interaction with incident light needed for creation of colors in the reflected light. One of the conditions that must be fulfilled for LSPR to appear is the existence of isolated metal nanoparticles. The demands on mass fabrication do not allow for nanolithography being performed on the single component. Therefore the creation of isolated metal structures should be due to the nanotopography of the polymer surface created in a replication based process. This has led to a basic structural design and fabrication process shown in Fig. 4.5. A mold is fabricated with two height levels, here with a periodic array of holes. In a replication process the polymer surface is formed with the inverse structures, here a periodic array of pillars with vertical sidewalls. Upon directional deposition of metal, isolated particles are formed on the top of each pillar. Also, a metal layer is formed on the lower lying surface comprising holes with the shape of the protrusions. For the shown case the result is a periodic disk array distanced from a periodic hole array. Finally a protective coating is applied which protects from handling and wear as well as deposition of grease from fingers as discussed in Sec. 3.4. This basic geometry have many parameters, which may be varied and the following analysis serves to narrow down the parametric space to that of highest interest and to arrive at the design with most possibilities.

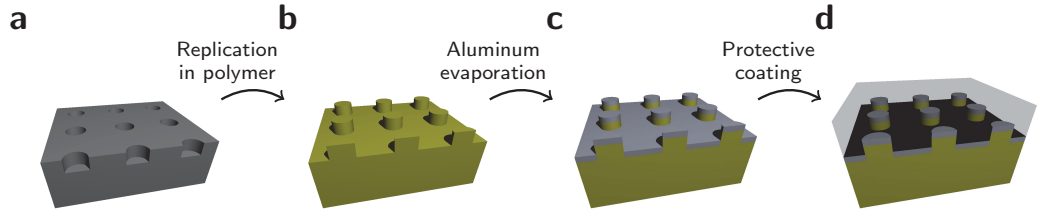

Figure 4.5: Basic concept of LSPR based colors. a) Mold comprising hole array. **b)** Replicated polymer part with pillar array. **c)** Directional deposition of metal leads to isolated disks and holey film. **d)** Protective coating allows for handling and practical use.

First the height of the polymer structures, h, is chosen to be constant throughout any area to be decorated. This will ease the fabrication of the master mold since only a single lithography step and a single etch step will be needed. The metal layer is also restricted to be of uniform thickness, t. A metal layer of varying thickness across a polymer part would complicate the metal deposition on the single polymer parts significantly. Thereby the desired plurality of colors should be due to tuning of the lateral dimensions only.

The geometrical shape of the metallic nanoparticles is important for its plasmonic properties. In this study protrusions with circular cross section have been chosen. This has several advantages. First the response of the resulting metallic disks are independent of polarization due to their angular symmetry. More elongated structures have significant polarization dependence. Triangles and squares would also be a possibility however they are harder to fabricate, since all processes tends to create rounded corners when going to very small structures. This is the case for the processes involved in both the master fabrication and in the following replications steps. The circular shape is an even bigger advantage when using the fast EBL method utilized in this work (see Sec. 4.4.1) since this method relies on the gaussian shape of the electron beam.

The lateral distribution of the individual structures is a very important parameter when it comes to the angular properties of the surfaces. Periodic arrays will lead to diffraction effects and coupling to SPPs in the underlying film, in discrete orders. The consequence is angle dependent optical response as described by the diffraction equation, Eq. (3.25) and by the condition for grating coupling to SPPs in Eq. (4.11). If positioned randomly, the structures will scatter light diffusely and not facilitate diffraction anomalies. This mimics the properties of a pigmented ink better. On the other hand, the distance between and therefore the coupling to neighboring resonators is constant for a periodic array, while it varies for randomly positioned structures. The coupling strength influences the resonance position and the randomly positioned disks will therefore suffer from inhomogeneous broadening of resonances although the single disks are identical. From a fabrication point of view the periodic structures are promoted due to the fast EBL scheme which only allows for periodic writing if the full speed potential should be utilized. Based on these consideration mainly periodic arrangements have been investigated. A quadratic unit cell with side length, Λ, has been chosen throughout the study. This could also have been chosen to be e.g. hexagonal which allows for higher density of structures. Future work could include a study of this geometry. The basic principles would be the same.

The protective coating is chosen to be transparent material with refractive index n_{coat} of approximately 1.5. This included many lacquers and polymeric coating materials. The optical thickness of the coating should be larger than the coherence length of the light in order to avoid Fabry–Pérot effects in the coating to disturb the color experience. Specifically this means that fringes in spectrum are allowed as long as they are closely enough spaced that the human impression is not affected.

In summary, an idealized schematic design consists of circular polymer pillars with diameter, D, and height, h, arranged in 2D periodic pattern with period, Λ. On this surface is a metal of thickness, t, deposited followed by a transparent coating. Of the four geometrical design parameters should only the lateral parameters D and Λ be varied to create multiple colors.

4.3.2 Choice of materials

For the proposed structure three materials are required; a base polymer, a metal, and a coating material. The base polymer should be chosen depending on the application, but in principle any polymer may be used. The coating material was already discussed above.

When it comes to the plasmonic functionality the choice of metal is very important. Optical properties, fabrication related issues and costs are all important factors. Here the discussion will be limited to four different metals; gold, silver, aluminum, and cobber.

A flat reflectivity throughout the visible spectrum for the corresponding bulk material is desirable since the engineering in larger degree can be done by structural modifications, with no need to take the abrupt spectral changes changes due to material dispersion into account. This particular argument promotes silver and aluminum as materials for this applications, since cobber and gold have interband transition thresholds in the central part of the visible spectrum.

The plasmonic resonances which may be produced by gold, silver and cobber are more narrow than what is possible with aluminum. This is due to the higher losses of aluminum [77], where high loss leads to broadening of the resonances. This is a important in applications such as sensing, however it is not as critical for creation of spectral variation across the visible spectrum for color purposes since many colors may be produced with relatively slowly varying features [73].

Also factors such as ease of fabrication and long term robustness has to be taken into account. The need for an adhesion layer such as titanium of chromium complicates the metal deposition for silver and gold, while aluminum and cobber attach better on most surfaces [78]. Gold has the advantage of being very inert and will not degrade due to reactions with atmospheric air. In that regard silver, which reacts with both oxygen and sulfur needs to be protected by a diffusion barrier (such as gold). Copper will also react with oxygen to form a cobber oxide, which is why copper statues and roofs turn green over time. Aluminum will also form a thin oxide layer on its surface. It is however very stable and stops growing at a thickness of 2-3 nm [79]. The oxide layer then protects the underlying aluminum.

When it comes to cost and abundance aluminum has the advantage while gold is the worst in that regard.

All in all it was chosen to use aluminum as the preferred metal for further investigations. An extra advantage of aluminum over e.g. silver will become evident when the angular dependence due to SPP excitation is discussed in more detail.

4.3.3 Numerical simulations

The initial design of the structures was based on numerical simulations, which have led to a more precise definition of the relevant design space and an understanding of the physical effects behind the spectra.

The used software was CST Microwave Studio, which was operated using the frequency domain solver in 3D. Periodic boundary conditions were employed at the boundaries in the lateral directions. Normal to the structures, the simulation domain was extending 300 nm away from the metal and at these boundaries Floquet ports were used, thereby defining the directions of transmitted and reflected modes. The programs build in mesh refinement tool was used for meshing with tolerance of 0.01.

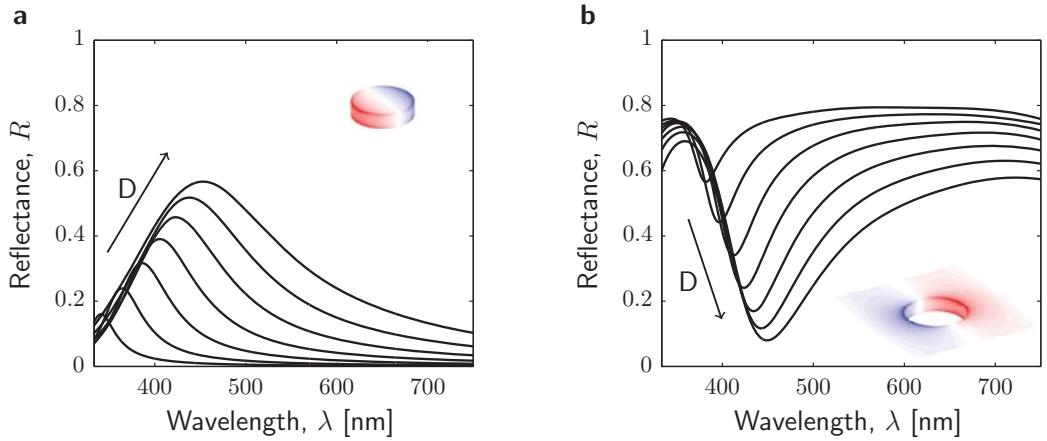

Figure 4.6: Reflectance of disk and hole arrays. a) Reflectance spectra of aluminum disk arrays with varying diameters from 50 nm to 110 nm in increments of 10 nm. Constant parameters were period, $\Lambda = 200$ nm, and metal thickness, $t = 20$ nm. The disks were embedded in a material with refractive index $n = 1.5$. The inset show the surface charge destribution. **b)** Reflectance spectra of hole arrays with similar parameter variation as for the disk arrays. The resonance position is seen to vary with diameter.

This implies that the tetrahedral mesh is iteratively refined until the relative error on the scattering parameters between three consecutive mesh refinements is less than 1 %. The mesh refinement was performed using the highest frequency of interest.

For calculation of spectra the build-in tool for broadband frequency sweep was used. Here the spectra are interpolated from a number of discrete frequencies at which the scattering parameters has been calculated. The number of frequencies necessary to calculate a spectrum depends on the sharpness of the spectral features. Again a stopping criterion is defined to accept the interpolated spectrum, when the relative deviations for all scattering parameters is less than 1 % two times in a row. The typical spectra are based on 10-15 frequencies. Calculation of electric and magnetic fields at specific frequencies (e.g. at resonance) was carried out separately after calculation of the spectrum.

For the simulations presented here the substrate has refractive index $n_s = 1.5$ and unless otherwise stated the structure is coated with a material with refractive index $n_{coat} = 1.5$. When no coating is present the upper material is air with refractive index of $n_{air} = 1$. The permittivity values of the aluminum is from Palik [80]. All shown spectra are simulated at normal incidence.

In order to minimize the parameter space, it was decided to identify an aluminum thickness which would be appropriate to achieve strong tunable effects. By fixing this the number of parameters was limited to three; pillar height, pillar diameter, and period. Based on the initial simulations the aluminum thickness was fixed to 20 nm.

The pillar height was found to have a significant effect on the spectral response and the ability to achieve strong resonances to be tuned by the lateral dimensions. The reason for this is the interplay between the plasmon resonances of the aluminum disk and the hole in the aluminum film. In Fig. 4.6 are the reflectance spectra of

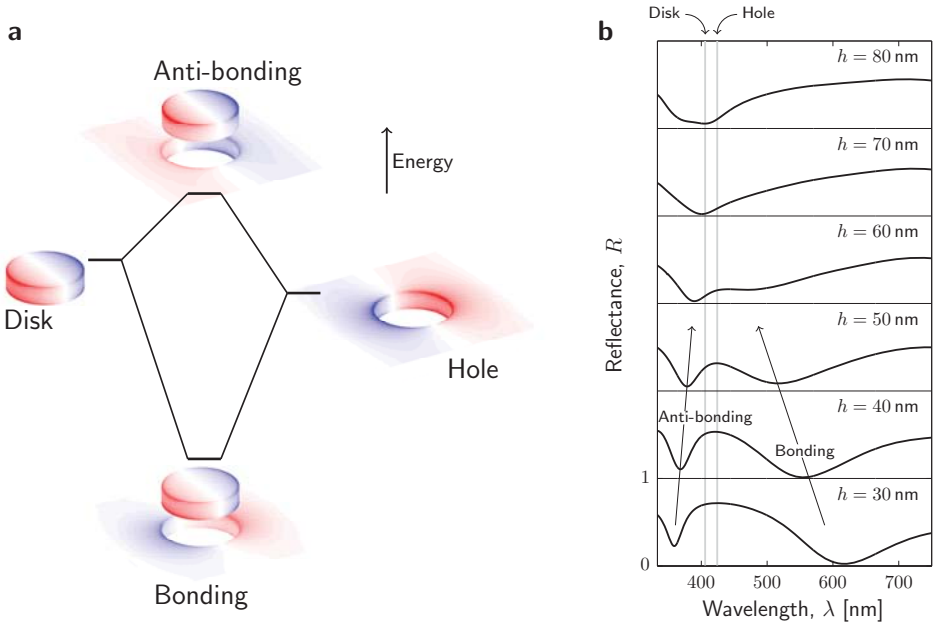

Figure 4.7: Plasmon hybridization in disk-hole structure. a) Energy diagram illustrating the relevant energy levels of the plasmon hybridization. The dipoles of the disk and hole split into two new modes, a low energy bonding mode and a high energy anti-bonding mode. The two new modes show different behavior in the charge oscillations. **b)** Reflectance spectra for varying pillar height, h. The energy splitting is seen to be highly depended on pillar height (vertical gap). The two distinct modes cease to exist for higher pillars.

disk and hole arrays shown for varying diameters, with fixed period of 200 nm and metal thickness of 20 nm. Both the disks and holes possess dipolar resonances which redshift with increasing diameter. One should notice the correspondance between the calculated extinction cross section of the oblate spheroid of Fig. 4.1 and the simulated reflectance of the disk array in Fig 4.6a. The surface charge density, σ, is shown as insets for the two cases. It is calculated from the electric field by use of Gauss law [81] and the boundary conditions for the electric field at the material interfaces. This gives

$$\sigma = \epsilon_0 \, \hat{\mathbf{n}} \cdot (\mathbf{E}_2 - \mathbf{E}_1), \tag{4.18}$$

where $\hat{\mathbf{n}}$ is the surface normal and $\mathbf{E}_1$ and $\mathbf{E}_2$ are the electric fields inside and outside of the metal respectively. It is noteworthy that the structures exemplifies the Babinet principle [82] such that the resonance position of the structures are close to being the same for a disk array and the similar sized hole array. There is a small difference which is due to the finite thickness and lossy metal.

When bringing the two dipoles close together as is the case in the proposed structure they start to interact and hybridize [83] into two new modes. Similar to the hybridization of atoms when forming molecular bond, one mode has lower energy than the initial modes (bonding mode) and the other has higher energy (anti-bonding mode). The energy splitting and the surface charge distributions of the relevant modes are shown in Fig. 4.7a. In the low energy mode it is seen that the charge

oscillations in the disk and hole are out of phase, while for the high energy mode they are in phase.

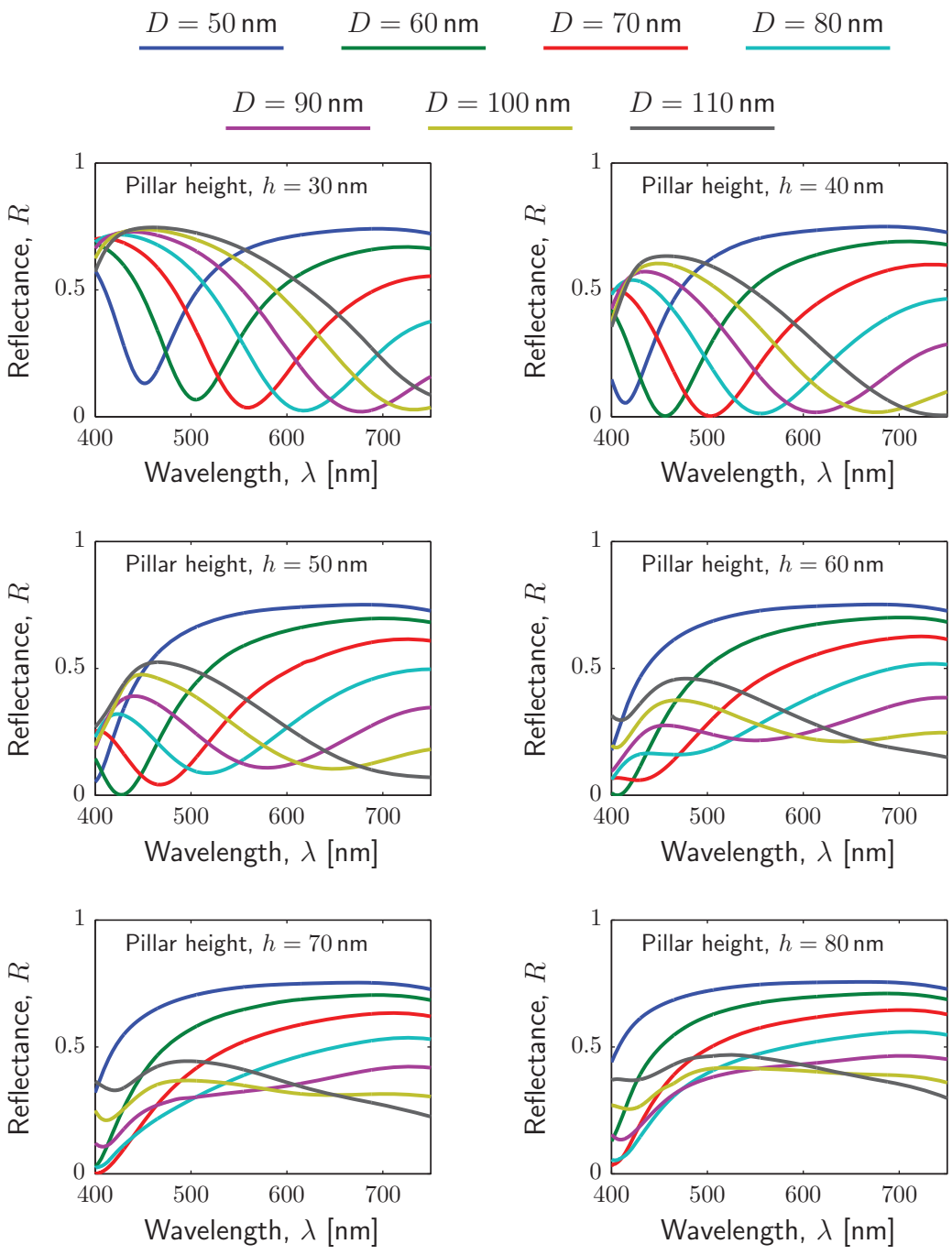

Figure 4.8: Dependence of pillar height. Simulated spectra for varying diameter and pillar height, but with constant period $\Lambda = 200\,\text{nm}$ and aluminum thickness $t = 20\,\text{nm}$. Each plot shows the spectra for a constant pillar height. The desired tunability of deep reflectance dips is present for low pillars, while this is not the case for higher pillars.

The coupling and therefore also the energy splitting is highly dependent on the distance between the disk and the lower lying metal plane. The impact of this on the reflectance spectra is significant as seen in Fig. 4.7b, where the pillar height is varied for a diameter of 80 nm and a period of 200 nm. The resonance positions of the corresponding disk and hole arrays are marked with vertical lines and the two hybrid modes move towards these as the pillar height is increased.

The position of the bonding mode is found to be very dependent on diameter, even more than is the case for the separate disk and hole dipole resonances of Fig. 4.6. This is utilized to create the desired tunability. In fact the existence of the hybrid modes seems to be crucial for any significant tunability across the visible spectrum to exist with the given choice of materials. This is illustrated in Fig. 4.8 where each plot illustrates the simulated reflectance spectra of different diameters for a specific pillar height. The period was 200 nm in all cases. It is seen that when a bonding mode of significant strength exists (low pillars) it is possible to create a deep dip anywhere in the visible spectrum, while this is not possible for the higher pillars. This conclusion is very important, when it comes to the use of aluminum as the plasmonic material. The opposite structure where the disks are located below the holey plane was also investigated numerically, however this configuration did not prove useful as it seemed impossible to excite the hybrid modes in the same manor. Therefore it was not possible to create the desired tunability of the resonances.

The influence of the diameter is also illustrated in Fig. 4.8. The resonance position is very dependent on diameter and it is the parameter with which one can tune the resonance position, when all the vertical parameters are fixed as demanded by the fabrication requirements.

The period of the structure has two effects. The normal incidence reflectance spectrum is affected by changing period due to the changed coupling between neighboring resonators. This effect is illustrated in Fig. 4.9a, where simulated reflectance spectra of different periods for constant diameter are shown. The influence on the resonance position is not as strong as is the case for the diameter, but it has an influence. In Fig. 4.9b this is shown in more detail, with a plot of the resonance

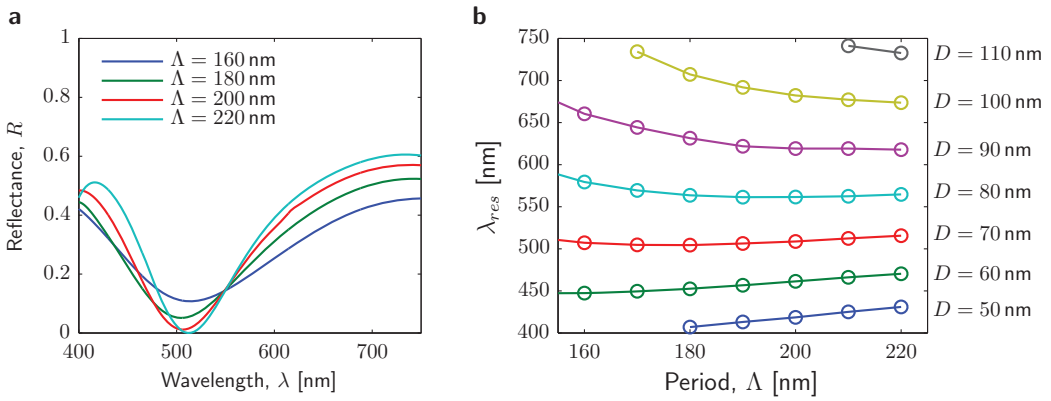

Figure 4.9: Resonance position - period dependence. **a)** Simulated reflectance spectra for varying period, Λ and $D = 70\,\text{nm}$, $h = 40\,\text{nm}$ and $t = 20\,\text{nm}$. **b)** Resonance position, λ_{res} as function of period for different diameters. The period is seen to have little influence on the resonance position compared to the diameter.

position as function period for different diameters are plotted. It is seen that a change in period is most important for larger disks since the neighbor-neighbor coupling is more pronounced in this case.

Besides this, the period it is very important when it comes to the angular behavior. The existence of diffraction orders is highly undesired as well is the grating induced coupling to SPPs. Both phenomena are very dependent on period and gives rise to undesired iridescence, when the period becomes too large. This is analyzed in more depth in the experimental section below.

4.4 Experimental results

4.4.1 Fabrication

The experimental realization of the plasmonic disk-hole structure as described above was carried out using EBL and dry etching for stamp fabrication and a hot embossing step for the production of samples.

Initially the first trial stamps were defined using conventional EBL. The need for significant areas for characterization and to demonstrate the practical applicability of the method a change was made to the fast EBL method as described in Sec. 2.1.1.

For the samples described below a current of 6 nA was used with aperture of 100 µm. The writing fields were chosen to be close to 200 µm with the exact size being determined by the period of the given structure. The exposures were carried out on silicon wafers with 120 nm zep520a. The samples were dry etched using the nanoetch process described in Sec. 2.1.1 for 20 s. After resist stripping the wafers were anti-stiction coated with FDTS.

A sample layout was designed, which included a sweep of the lateral parameters, D and Λ. The period was varied from 160 nm to 240 nm in steps of 20 nm by varying the shot pitch of the EBL system. The variation in diameter was carried out by variation of the nominal dose from 5 µC/cm^2 to 180 µC/cm^2 with varying increments.

Based on the numerical analysis it was chosen to etch to a depth of between 50 and 60 nm to be in the hybridization domain, yet still allowing for the disks to be separated from the lower lying plane. As will become evident below, this extra height compared to the optimal simulation results is needed due to rounding of the end-facet of the pillars. The height was measured with a standard tip in AFM to be $h = 56 \pm 4$ nm by use of the height histogram of the images, where the uncertainty is based on the width of the peaks in the histograms.

The etched silicon master was inspected with SEM (Zeiss Supra VP 40) to map the resulting size of the etched holes. The hole size for each of the areas was determined using image analysis of the obtained SEM images. For the silicon master the structures were imaged with acceleration voltage of 7 kV and a working distance of 3.0 mm using the in-lens detector. The magnification was such that the width of the imaged area was 2 µm. The extraction of hole sizes was done using a MATLAB script, which from a threshold determines the edge of the hole. This method should be used with care due to edge-blooming effects, which makes it difficult to determine the exact position of the edge. The method was compared with AFM measurements of selected areas, which confirmed the obtained results.

The area of all holes in a picture was measured and this was converted to an equivalent diameter (diameter of circle with similar area). The result of the analysis

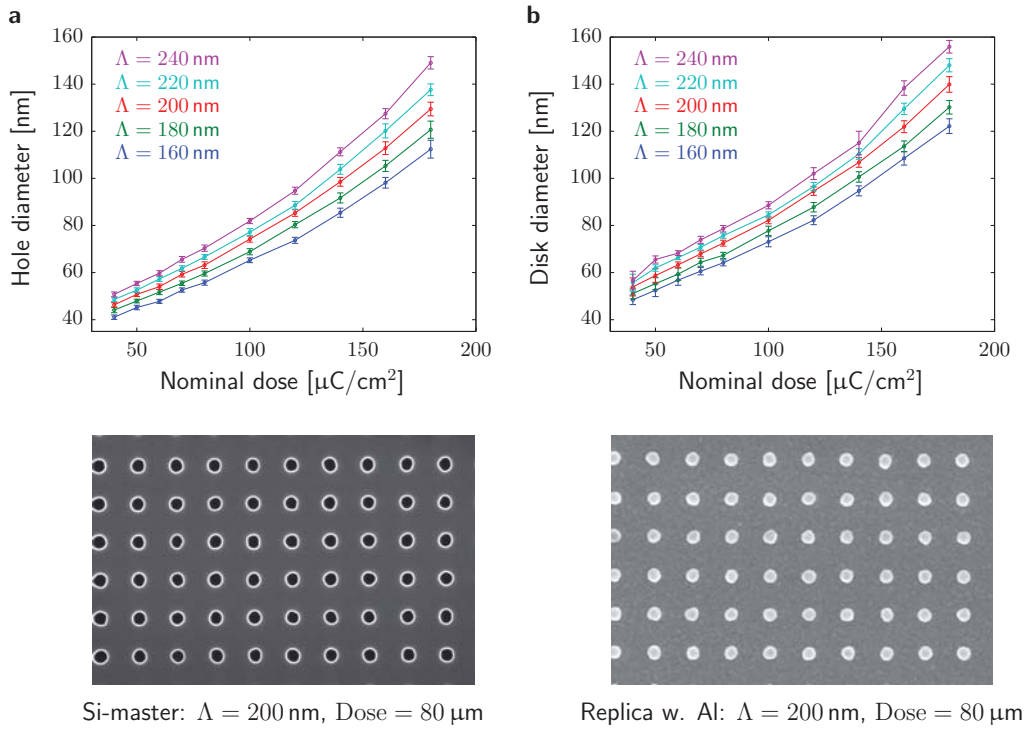

Figure 4.10: Hole and disk sizes. a) Hole diameter in the silicon master as function of nominal dose for the fast EBL method from SEM analysis. The errorbars indicate the standard deviation within one picture. Also shown is one of the used images. **b)** Similar analysis as in panel a, but for the aluminum coated polymer replica. Again one of the used images is shown, corresponding to the master shown in panel a.

is shown in Fig. 4.10a where the obtained diameter-data are plotted as function of nominal dose. The errorbar on the measured diameter indicates the standard deviation on the calculated diameter within a picture. Also shown is an example of a picture used in the analysis. The sample areas with a nominal dose less than 40 $\mu C/cm^2$ have been omitted from the plot, due to bad quality of the samples with large variation in hole sizes. From the analysis it is seen how it is possible to tune the hole diameter from 40 nm to above 150 nm by varying the nominal dose. It is also seen how the same nominal dose results in different hole sizes for different periods. This is expected since a higher charge per hole is delivered for larger periods with the same nominal dose. The backscattering is constant for constant nominal dose.

The same type of analysis was carried out on polymer replications with aluminum deposited on top. For these pictures the acceleration voltage was 2 kV and a working distance of 2.9 mm. The result of this analysis is shown in Fig. 4.10b along with one of the used images (corresponding to the master image in Fig. 4.10a). What should be noticed is an overall increase in diameter of 8 nm on average, which is attributed to the way the aluminum is deposited on top of the pillars with a small overhang. The embossing was done thermally in a 4 μm 75K PMMA film spin-coated on glass wafers (BOROFLOAT 33, 0.5 mm thick). This method was chosen to demonstrate the ability to do replication in thermoplastics, while maintaining very well-defined and

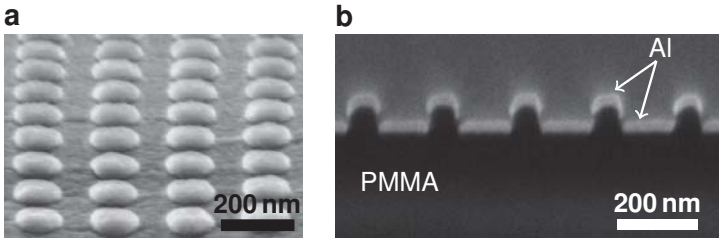

Figure 4.11: Fabricated surfaces imaged with SEM. a) Slanted view, 15 degrees above the horizon. **b)** Cross section obtained using focused ion beam for milling of the edges. The disks are seen to have a significant overhang due to rounded pillars.

flat samples for optical characterization. The embossing was carried using at 190°C with a pressure of 6 bar held for 30 minutes before cooling to 90 °C and releasing the pressure (CNI, NIL Technology).

Aluminum deposition was carried out using e-beam evaporation allowing for minimal step coverage as described in Sec. 2.1.4. Using the QCM the thickness was controlled to 20 nm and the rate was 1.5 nm/s.

The protective coating was in this case Ormocomp applied by multiple spin-coating and UV curing steps until the desired thickness was reached, where no visible interference fringes were seen.

From the SEM images of Fig. 4.11 it is seen that a significant rounding of the metal disks is present in the fabricated samples. The disk tends to characterized better as a curved cap on top of the pillar. This discrepancy from the ideal cylindrical disks arise during the different fabrication steps. The etch does not produce perfectly sharp corners in the bottom of the holes. The replication process will due to thermal shrinkage enhance this effect, and the metal deposition will deposit the metal with an overhang.

Based on the analysis of the samples of the first master two more masters were made. One with larger areas (4×6 mm^2) for use in angular resolved measurements and one with a more 'popular' layout. The latter was fabricated to demonstrate the possibilities for drawing illustrations and logos. It contained a DTU logo comprising areas with three different hole sizes all arranged with a period of 200 nm, thereby creating three different colors. The resulting surfaces are shown later in this section.

4.4.2 Normal incidence measurements

The reflectance at normal incidence as function of period and diameter was measured using the microscope setup (Sec. 2.2.1) for samples both prior and after coating. The resulting spectra, as well as bright field microscope images of the samples are shown in Fig. 4.12. In the case of the coated samples a boxcar filter (6 nm wide) has been used to filter out the Fabry–Pérot noise introduced by the from the spectra.

First of all it is noticeable that a wide range of bright colors may be produced by varying the lateral parameters as done. This is the case for both the uncoated and coated samples. Unlike the case of Roberts *et. al* [71], where the plasmonic modes were affected little by the deposition of a coating, a significant red-shift of the spectra is seen here for all samples. This is evident from both the spectra and

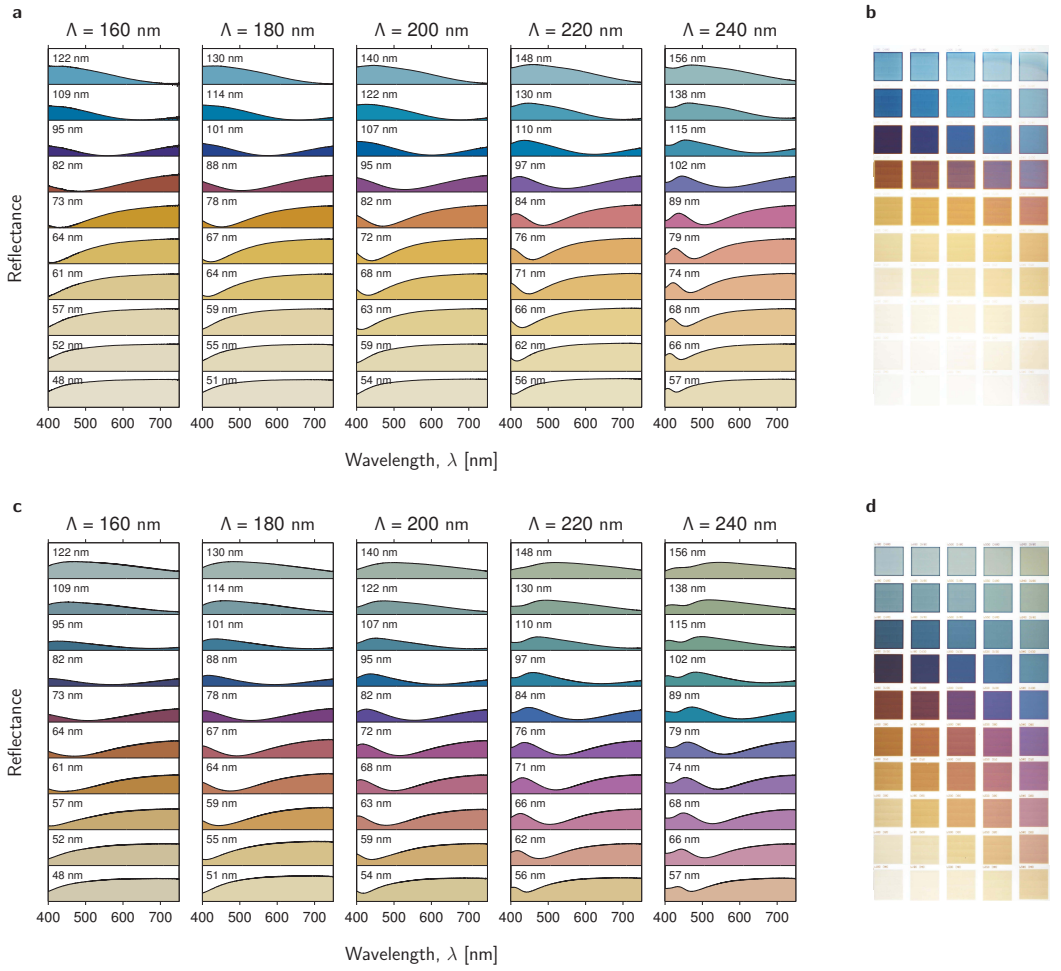

Figure 4.12: Experimental reflectance spectra. a) Reflectance spectra measured on uncoated sample. Each column has constant period, while the diameter is indicated in the corner of each spectrum. **b)** Bright field microscope image of the uncoated sample used for the measurements. Each colored fields has a sidelength of 800 µm. **c)** Reflectance spectra measured on coated sample. **d)** Bright field image of coated sample.

the microscope images. This is due to the increase in the effective refractive index surrounding the structure and is in line with what is predicted from the polarizability of simple dipolar plasmonic resonators, as in Eq. (4.3). The overall spectral behavior confirms what was found in the numerical simulations. There is a strong dependence of the diameter on the resonance position. The exact resonance positions as given by the spectra has been extracted for each period and are plotted in Fig. 4.13a-e. The red-shift introduced by the coating is very clear in these plots. It is seen that an almost linear relation between the diameter and the resonance wavelength may be found for constant period. A linear fit has been found for each period and the slope is plotted in Fig. 4.13f. This slope indicates the spectral shift of the resonance due to a change in diameter of 1 nm of the disks. In other words it tells how sensitive the system is to structural changes. If the slope is low a large diameter change is needed to move the resonance, but the system is less sensitive to variations in

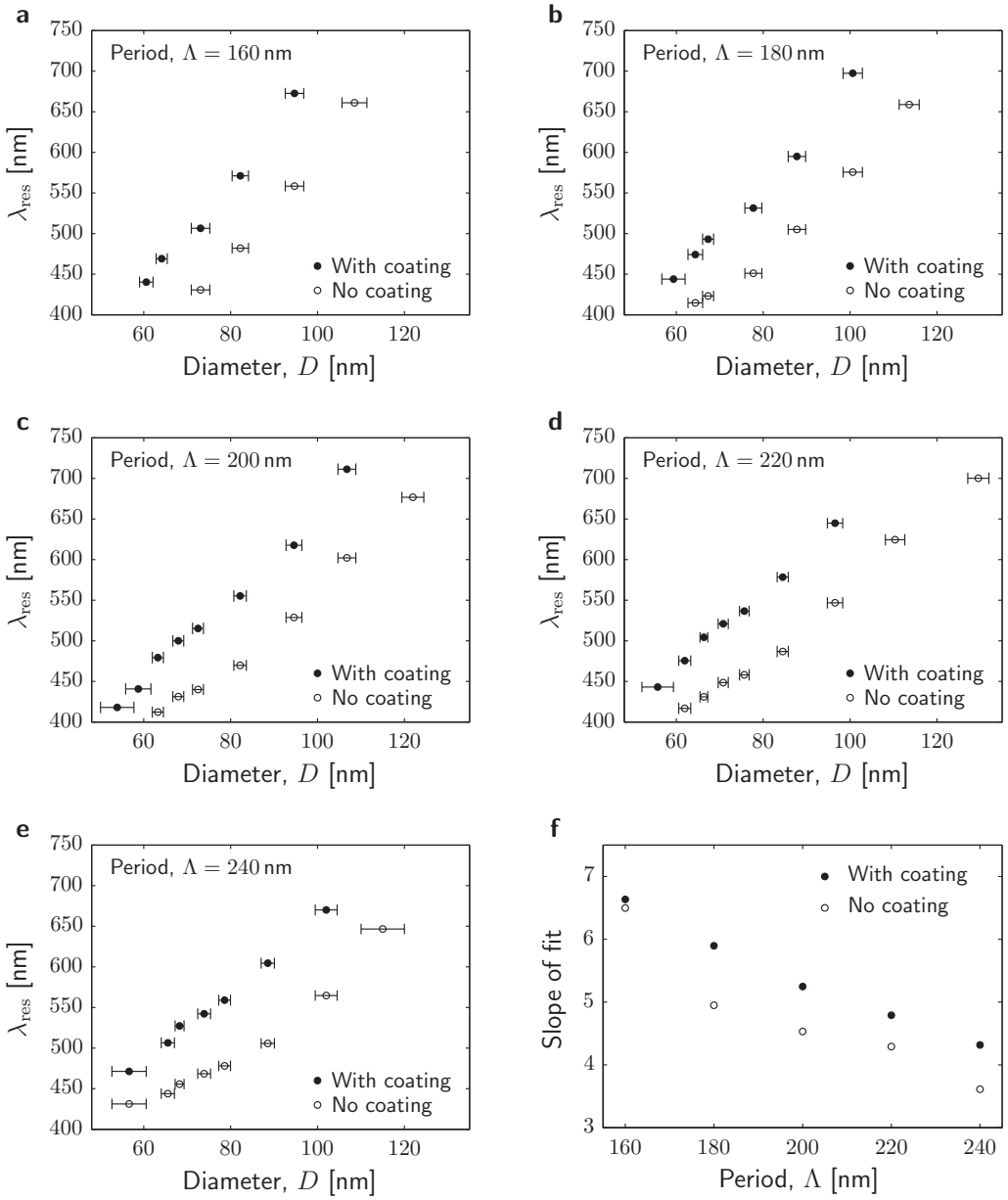

Figure 4.13: Experimental resonance positions. **a)** Resonance position as function of diameter for period, $\Lambda = 160\,\text{nm}$ for the coated and uncoated sample of Fig. 4.12. **b)** $\Lambda = 180\,\text{nm}$. **c)** $\Lambda = 200\,\text{nm}$. **d)** $\Lambda = 220\,\text{nm}$. **e)** $\Lambda = 240\,\text{nm}$. **f)** Slope of best fit as function of period extracted from panels a-e.

reproducibility compared to the case of a high slope. The period has significant influence on this slope and it is seen that it is approximately 7 for $\Lambda = 160\,\text{nm}$ and only 4 for $\Lambda = 240\,\text{nm}$.

When comparing the experimental spectra of Fig. 4.12 with the simulated spectra of Fig. 4.8 it becomes evident, based on the resonance positions, that the experimental results resembles the simulated spectra with lower pillars than what was measured by AFM. This difference is due to the rounding of the end facets of the polymer pillars which takes place during fabrication, as discussed above. This reduce that

vertical gap between the disk and the lower lying plane thereby leading to higher coupling. From this it is seen that the vertical gap is a more significant parameter than the pillar height.

4.4.3 Near-field measurements

As described, the lower lying holey film plays an important role since the holes contribute to the hybrid plasmonic mode which leads to the tunable absorption resonances. However, it also supports SPPs, which due to the angle-dependent grating-coupling criterion leads to undesired angle-dependent spectral features. Near-field measurements of the SPP mode and disk resonances have been carried out using a dual probe near-field scanning optical microscope (NSOM, MultiView4000TM, Nanonics Imaging Ltd.). In this system the excitation is done using one tapered metal coated fiber probe, which is kept at a fixed position and the near field is measured with another fiber probe by scanning an area in the close vicinity of the excitation. In practice this is done by adjusting the distance between the tips until

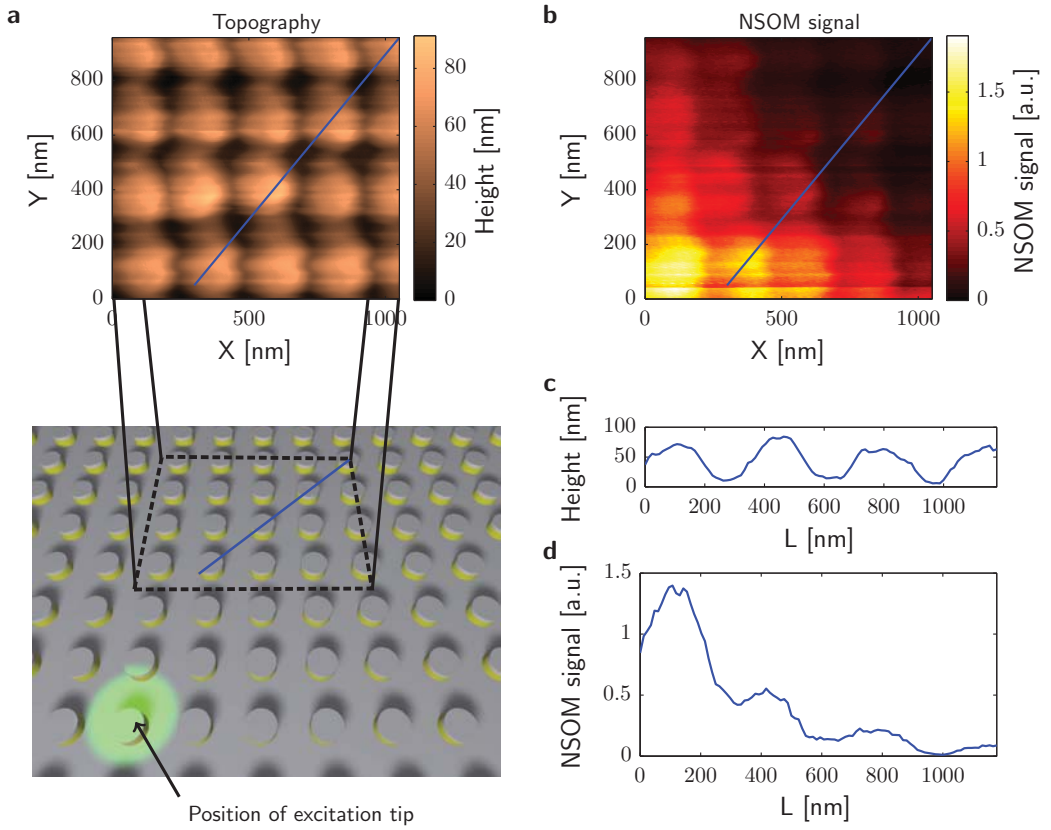

Figure 4.14: Near field measurements. a) Topographic data of the scanned area obtained simultaneously with the near field data of panel b. The sketch indicates the approximate relative position between the excitation probe and the scanned area. **b)** NSOM signal from the scanned area. **c)** Topographic profile along blue line in panel a. **d)** NSOM signal profile along blue line in panel b. A clear decay away from the excitation is seen along with increased signal above the disks indicating the localised plasmon resonance.

the scanning tip scans across the stationary tip. By scanning away from this point the approximate position of the excitation is know.

Such a measurement is shown in Fig. 4.14 for a sample with $\Lambda = 240\,\text{nm}$ and $D = 102 \pm 3\,\text{nm}$ with light of wavelength 532 nm. The resonance for the given structure is centered around $\lambda = 565\,\text{nm}$, but extends beyond the excitation wavelength. The measurement method allows for simultaneous sampling of topography (Fig. 4.14a) and NSOM signal (Fig. 4.14b). The approximate relative position between the scanned area and the excitation probe is indicated. In Fig. 4.14c and d cross-sections of topography and NSOM signal are shown. Due to the sharp subwavelength excitation tip (aperture diameter of 100 nm) the light contains a range of horizontal wavevector components, which enable coupling to the propagating surface modes of the lower lying aluminium film, as described in Sec. 4.1.3. These modes propagate away from the excitation point and couple to the individual disk resonators, which thereby are excited. The decaying nature of the SPP signal as measured by the NSOM away from the excitation tip is clearly seen as well are the localized modes around the disks. From exponential fits an approximate propagation length of 300-400 nm is estimated (decay to a factor 1/e of initial value). A flat continuous 20 nm thick aluminum film will theoretically support two SPP modes with decay lengths of 2 µm (even) and 11 µm (odd) for the wavelength in question. The much shorter decay length found here is due to large loss to excitation of the localized modes. The tip used for detection had an aperture diameter of ∼200 nm which is bigger than the individual disk resonators and it is therefore not possible to resolve the dipolar nature of the localized modes. The large size of the detection probe relative to the structures also result in significant tip-folding in the topographical image.

A more thorough investigation using several wavelengths (on and off resonance), in combination with differently sized disks would have been interesting. This was however not possible due to limited amount of time on the equipment.

4.4.4 Angle dependence

The angular response is key if the method is to be used as replacement for inks. Therefore the sensitivity to varying observation angle was measured using the angle resolved measurement setup described in Sec. 2.2.2. The specular reflectance was measured as function of angle, $\theta = \theta_{in} = \theta_{out}$, on samples with areas $4 \times 6\,\text{mm}^2$. The samples were oriented such that the angle was varied along the direction of the grating. In Fig. 4.13a is the data from such a measurement of a coated sample with period 200 nm and disk diameter of 86 nm shown in a surface plot. The color indicates the reflectance plotted as function of wavelength and angle. The characteristic dip in reflectance known from the normal incidence measurements arising from the 'bonding' mode is seen around $\lambda = 580\,\text{nm}$. This broad resonance dip shifts approximately 20 nm as the angle is increased to 70 degrees. Another dip in the reflectance emerges from the low wavelengths at an angle around 20 degrees. As the angle is increased this dip moves to higher wavelengths. This behavior is undesirable since it introduces angle dependence in the reflectance spectra. The dashed black lines indicate the theoretical location of the odd and even SPP modes for a 20 nm aluminum film embedded in a material with refractive index 1.5. It is seen that the even mode correspond well to the angle dependent dip. The even mode is also the most lossy of the SPP modes as the imaginary part of SPP propagation constant β is significantly higher for this mode than for the odd mode. At the higher angles it is seen that the

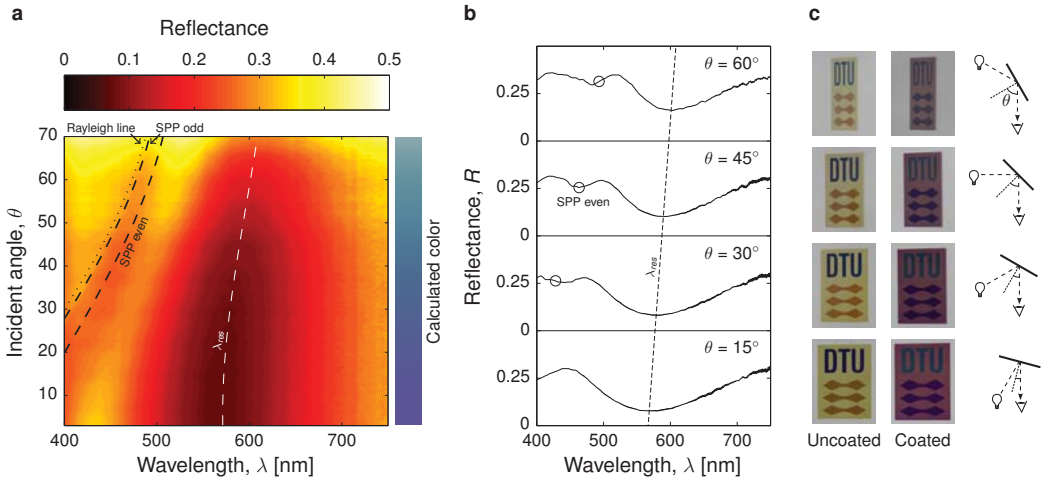

Figure 4.15: Angle resolved measurements. a) Angle resolved measurements of coated samples with $\Lambda = 200\,\text{nm}$ and $D = 86 \pm 2\,\text{nm}$. The theoretical positions for excitation of SPP modes and the Rayleigh line are indicated. **b)** Spectra at four specific angles. The even SPP mode is indicated with circles. **c)** Photographs of a DTU logo fabricated with the method taken at different angles. Both an uncoated and a coated sample is shown. The low angle sensitivity is clearly seen. The logo is 11.4 mm tall.

even mode deviates slightly from the center of the dip. This is due to interaction with the localized mode, which push the modes away from each other. This effect is also expected to cause the redshift of the 'bonding' mode resonance. This effect is described below in more detail for a sample where the effect is more evident. The Rayleigh line where new diffraction orders appear, is also indicated in the plot, however in this case it does not seem to cause a strong anomaly in the specular reflected light. The main problem with diffraction is the reflected 1st order modes, which due to their dispersion leads to iridescence if they are present.

The calculated color as function of angle is shown in the bar next to the surface plot. It is seen that the angle dependent features shift the color slightly as the angle is increased, but that the color is very constant at least up to around 40 degrees.

Four spectra at selected angles are shown in Fig. 4.13b illustrating the same features as shown in the surface plot in more detail.

To illustrate the low angle sensitivity of the color a DTU logo ($8.5 \times 11.4\,\text{mm}^2$), fabricated with the method, is shown from different angles in Fig. 4.13c. The three colors in the logo are made of arrays with $\Lambda = 200\,\text{nm}$, but with different diameters. Both an uncoated and a coated version of the sample is shown, and it is seen that the colors of the logo are constant as the angle of observation is changed.

In the example above the spectral spacing between the SPP mode and the localized mode was large so the effect on the localized mode was not very significant. In other cases the two modes interact more as the angle is increased. Such an example is shown in Fig. 4.16, where the specular reflectance of uncoated sample with period 200 nm and diameter 66 nm is shown. For this structure the resonance of the 'bonding' mode lies around $\lambda = 440\,\text{nm}$ at normal incidence. The white dashed line mark this wavelength and the black dashed lines mark the theoretical position

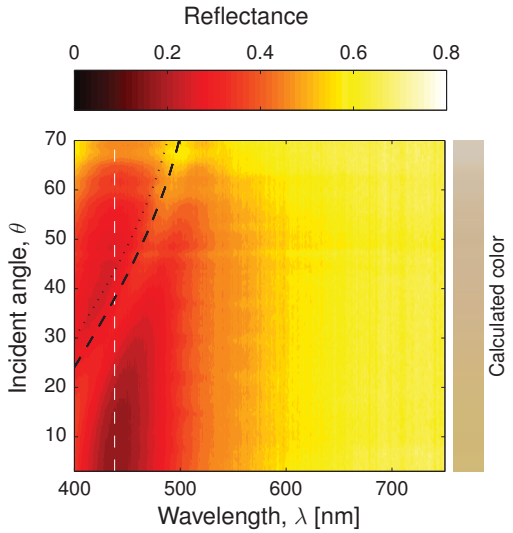

Figure 4.16: Avoided crossing between SPP and localized mode. Surface plot of specular reflectance of uncoated sample with $\Lambda = 200\,\text{nm}$ and $D = 66 \pm 2\,\text{nm}$. The white line marks the resonance position at normal incidence and the dashed black line show the theoretical SPP position for a continuous film.

of the relevant SPP mode. As seen the modes do not follow these lines. In the λ-θ plot, which corresponds to an energy-wavevector plot, the two modes show what is known as avoided crossing [84], which arise due to coupling between the two. The mode which starts as localized mode bends and becomes more SPP-like, and the SPP mode bends and become more like the localized mode. This illustrates that the existence of SPP modes does not only affect the angular response due to its own dispersion. It also couples to the mode, which is at normal incidence is responsible for the color and shifts this. As a result the color starts to change at lower angles as seen by the colorbar to the right of the plot. This was already seen in Fig. 4.13 where a small shift of the localized mode was observed despite the large spacing between the modes.

It should be emphasized that the case in Fig. 4.16 is not symmetric in refractive index and the SPP dispersion should be found from Eq. (4.12). In the given case only one mode is relevant. It is the mode which is mainly located on the polymer-metal interface on the backside of the film. The mode corresponding to the other surface is not present in plot as it is only relevant for even higher angles.

In all the shown cases the period has been 200 nm. The positions of both diffraction anomalies and the important SPP mode are both highly depended on the period. The diffraction equation only involved the materials surrounding the metal and is therefore determined solely by the period if we assume polymer embedding. The SPP mode on the other hand depends on the dielectric properties of the chosen metal. As an example aluminum and silver is compared in Fig. 4.17, where the even SPP mode is plotted for both materials and for different periods. It is seen that for aluminum it is possible to move the mode out of the plot by lowering the period. At $\Lambda = 160\,\text{nm}$ the mode does not show up before 60 degrees, and the influence on the angle sensitivity is therefore minimized. Going to this small periods will however

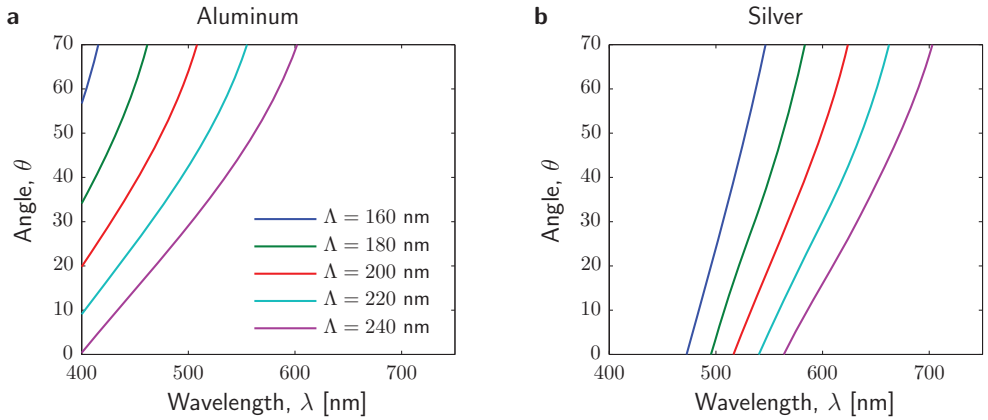

Figure 4.17: SPP position depending on period and materials. a) The position of the even SPP mode for a 20 nm thick aluminum film embedded in material with refractive index 1.5 for varying periods of the grating which facilitates the coupling. The angle refers to the incident angle in air for easy comparison with the measurement results of Fig. 4.15. **b)** Similar to panel a, but for a silver film.

complicate the fabrication and make the optical response more sensitive to variation in the diameter as discussed above. For silver the mode lies in the visible spectrum no matter what, even at normal incidence. This makes it impossible to remove the coupling to SPPs and the angle dependence is affected accordingly. Based on this analysis aluminum is favored as the metal of choice.

It can be concluded that the specular reflectance of the surface is relative insensitive to the angle. The SPP excitation leads to angle dependent effects, which may be avoided by going to even smaller periods.

4.5 Discussion and outlook

The surfaces described above do posses some of the qualities which are needed for use in decoration. There are however challenges which should be addressed in the future.

First of all the basic premise of the subwavelength gratings is that it is a specular effect. This means that despite low angular dependence in the reflectance a uniform color experience demands uniform illumination. This is often not the case. As already mentioned one way to get around this is by arranging the pillars in a non-periodic manor, however due to broadening of resonances and much lower writing speed this is not a good solution. Another method would be to functionalize the coating in such a way that it scatters the light. This scattering could be introduced by use of a semi-crystalline polymer as coating which scatters light at the grain boundaries. Another method could be by surface texture in the coating and a third method could be to have scattering particles contained in the coating. No matter which method is used the scattering will take place both before and after interaction with the plasmonic structures and therefore the observed color will be a mix of light reflected at different angles at the surface. Of cause the scattering and more uniform color experience comes with the price of worse resolution in the printing method. How

sharp and small features it is possible to make depends on the amount of scattering. This should be investigated in an empirical study.

Secondly, the range of colors which may be produced is limited as only the colors based on a reflectance dip arise using this method. A very nice red is for example hard to make as it is based on a low reflectance in a large wavelength interval. In order to extend the amount of colors, which is possible to fabricate one could combine more than one disk size in the grating unit-cell. This approach is also what is proposed by Tan *et al.* [73]. What is important to note is that it is not enough to just place pixels of a given size (e.g. $10 \times 10\,\mu\text{m}^2$) next to each other as the result will be the average spectrum. This is illustrated in Fig. 4.18, where simulated spectra are shown for the fixed parameters, $h = 40\,\text{nm}$, $t = 20\,\text{nm}$ and $\Lambda = 200\,\text{nm}$. In Fig. 4.18a are the spectra of the case of $D = 50\,\text{nm}$ and $D = 100\,\text{nm}$ shown. In Fig. 4.18b are these two disk sizes combined in two different ways. One is the average spectrum which arise if pixels of arrays with the two sizes are placed next to each other. The other is if the two disk sizes are combined in the same unit cell of the grating. There is a very big difference in the result as both disks contribute to absorption light, when they are

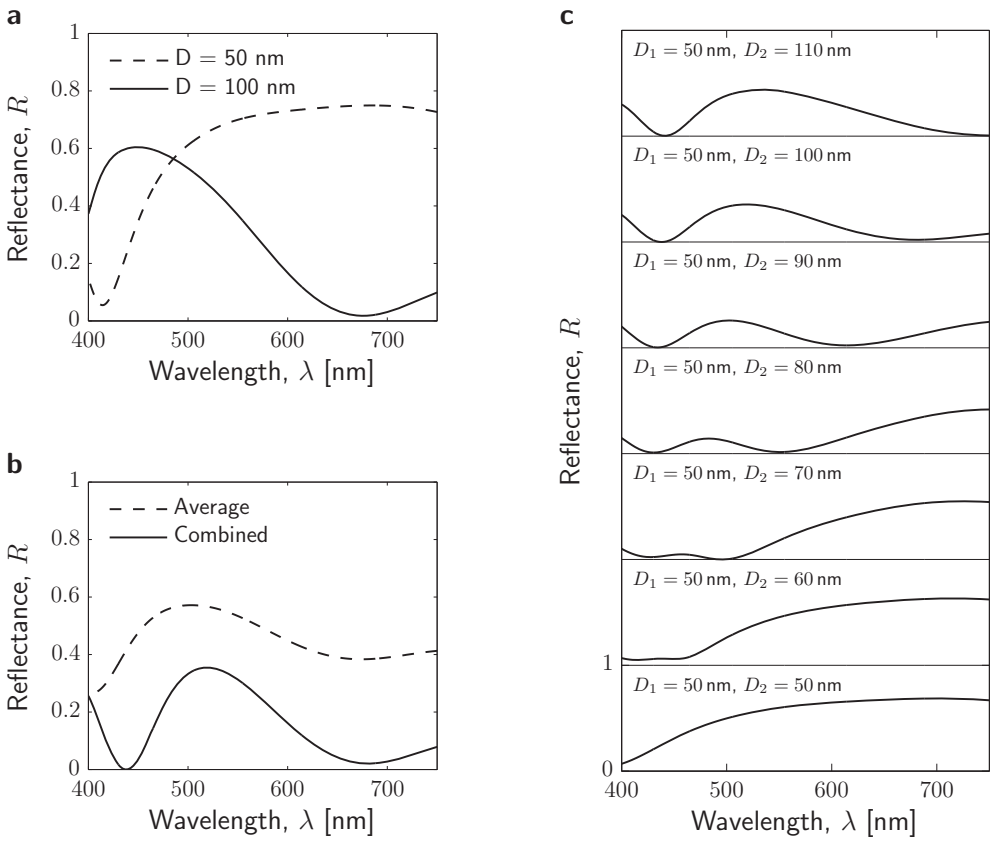

Figure 4.18: Effect of combined diameters. a) Simulated reflectance spectra of with fixed parameters $h = 40\,\text{nm}$, $t = 20\,\text{nm}$ and $\Lambda = 200\,\text{nm}$. The spectra of two different diameters are shown. **b)** The two different spectra combined in two ways. One as the average arising from larger pixels and the other as combined in the same unit cell. **c)** Spectra arising from varying the size of one of the disks in a unit cell.

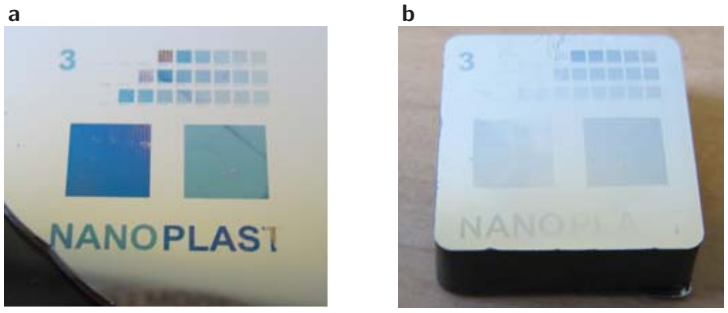

Figure 4.19: Issues with replication. **a)** Sample made from Ni shim using UV-casting of Ormocomp. The colors are created upon aluminum deposition. **b)** Injection molded polypropylene sample. The colors are not created due to bad replication.

combined on a small area. This will not happen in the pixel case. In Fig. 4.18c it is shown how the two resonance dips may be tuned independently by varying the size of one of the disks. The resonance position of the fixed disk is only slightly shifted due to the change of the other diameter.

The last point is the feasibility in relation to mass production. The overall fabrication scheme allows for large volume production, however until this point the method has not been transferred to an industrial process. Both the polymer replication and the metal deposition constitutes challenges. In Fig. 4.19 are samples from an industrial scale experiment shown. In this experiment, a Ni-shim was fabricated from a polymer imprint, such that the shim had same polarity as the silicon master. The sample in Fig. 4.19a shows the result from UV-casting using Ormocomp from such a shim, while Fig. 4.19b shows the result if the shim is inserted in an injection molding tool and used as mold for injection molded polypropylene samples. The colors arise in the UV-casted case, but not in sample made from injection molding. The replication quality is simply not good enough. This has been the trend in all replications made in bulk thermoplast samples and a significant effort must be invested in this transfer to large scale methods in the future.

The metal deposition step is also critical. It is problematic to do the line of sight deposition on free form units for the case of injection molded plastic parts. Also the handling of individual parts into a vacuum chamber may constitute a problem. Roll-to-roll, which was mentioned in Sec. 3.4 may be the solution as roll-to-roll metal evaporation systems exist. Whether it with these systems is possible to create isolated disks must be investigated.

These challenges must be met before the effects successfully can be used for large scale color printing on plastic.

Chapter 5

Conclusion

Under the assumption of replication based fabrication it has been investigated how far structural color effects in the surface of polymers may be pushed. The proposed nanostructured surfaces have been investigated through theoretical considerations and experimental prototyping.

For pure polymer surfaces it was shown how tapered surface structures may lead to either an anti-reflective effect or transmission color filters depending on the size of the structures. This type of structures were formed using self-masked reactive ion etching. When the structures are sufficiently small they work as a gradient in the refractive index at the air-polymer interface, thereby suppressing the Fresnel reflection, which would normally be present. In clear materials this is advantageous when surface glare makes it difficult to for example read the text behind a screen or protective cover. It was shown how this type of structure, when applied to pigmented polymers effectively increases the chroma of the pigmented surface. In that case more light is allowed to interact with the pigment before being reflected towards the observer and the color due to the pigment may therefore be observed as being more pure or clear.

For larger structures wavelength depending scattering was observed and it was shown how different colors may be produced in the transmitted light, due to different tapered surface geometries formed by the self-masking process. The colors arise due to diffraction and the specular transmittance may be linked directly to the phase shift undergone by the light as it propagates through the random surface topography by use of diffraction theory.

The diffraction grating as a color producing element was discussed as element in the surface of an opague polymer and as element in transparent polymer foils. The reflectance is very limited, when only the reflectance at the interface is considered therefore only black pigments constitutes a dark enough background for gratings to be sufficiently visible. In a transparent foil the total internal reflection on the backside of the foil allows for total reflectance, which is an order of magnitude higher than that of a single interface. This may be utilized in combination with diffusive elements to create foils, which reflect colored diffusive light when illuminated at normal incidence. The proposed concept did however have some flaws, which degrade the effect.

None of the fabricated effects proved able to replace inks by any means. These effects should more be seen as possible effect-surfaces used as eye catchers in cheap one time use products such as packaging. A major issue is the lack of mechanical

robustness, which cannot be improved by protective coating due to index matching.

By relaxing the design criteria and allowing for deposition of aluminum it has been shown that it is possible to create bright reflective colors, which show little angular dependence. By formation of a polymer pillar array and subsequent aluminum deposition it is possible to create features in the metal, which support tunable LSPR. The main tuning mechanism is the pillar diameter, when the pillar height and metal thickness are fixed.

The fabrication method forms a disk array distanced above a hole array. Both disks and holes possess dipolar resonances on their own, but the interplay between these dipoles haven proven crucial for the functionality of the metasurface. When brought close together the modes hybridize and new modes are formed of which the low energy mode to large extend is the one used for the color creation. Deep tunable resonances are present, when the vertical gap between the lowest part of the disk and the highest part of the underlying film is small enough. Few tens of nanometers is needed for the proper coupling.

In the fabricated devices a significant rounding bends the disks downwards close to the film thereby increasing the coupling. It is crucial that the disks are not connected to the underlying film.

The sensitivity to varying incident angles was found to be low, at least for angles up to around 40 degrees. The main limitations is due to coupling to SPP modes, which creates angle dependent absorption dips and interacts with the localized modes. This effect may be limited by going to smaller periods, around 160 nm.

The main challenges in the progress towards industrial scale applications include repeatable dimensional control of the master over large areas. The effects are ultra sensitive to structural variation. Furthermore the replication processes in bulk polymer should be of high enough quality such that pillars with vertical sidewalls and little end-facet roundings are produced. The large area metal deposition with sufficiently directional deposition is a challenge, especially in terms of fabrication time and cost. And finally the functionalization of the coating material in order to produce diffuse reflecting surfaces should be investigated to limit the sensitivity to variations in illumination. If these challenges are overcome the proposed plasmonic metasurface may be used for large area color printing on plastics without using inks.

References

[1] Fried, J. R. *Polymer science and technology* (Prentice Hall, 2003).

[2] Thompson, R. C., Swan, S. H., Moore, C. J. & vom Saal, F. S. Our plastic age. *Phil. Trans. R. Soc. B* **364**, 1973–6 (2009).

[3] Hopewell, J., Dvorak, R. & Kosior, E. Plastics recycling: challenges and opportunities. *Phil. Trans. R. Soc. B* **364**, 2115–26 (2009).

[4] Thompson, R. C. *et al.* Lost at sea: where is all the plastic? *Science* **304**, 838 (2004).

[5] Deco Technology Group Inc. *Pad Printing* (accessed May 6, 2014). Http://www.decotechgroup.com/library/pad-printing/.

[6] Seago, A. E., Brady, P., Vigneron, J.-P. & Schultz, T. D. Gold bugs and beyond: a review of iridescence and structural colour mechanisms in beetles (coleoptera). *J. R. Soc. Interface* **6**, S165–S184 (2009).

[7] Stavenga, D., Foletti, S., Palasantzas, G. & Arikawa, K. Light on the moth-eye corneal nipple array of butterflies. *P. Roy. Soc. B-Biol. Sci.* **273**, 661–667 (2006).

[8] Kinoshita, S., Yoshioka, S. & Miyazaki, J. Physics of structural colors. *Rep. Prog. Phys.* **71**, 076401 (2008).

[9] Bernhard, C. G. Structural and functional adaptation in a visual system. *Endeavour* **26**, 79–84 (1967).

[10] Clapham, P. & Hutley, M. Reduction of lens reflexion by the moth eye principle. *Nature* (1973).

[11] Wilson, S. & Hutley, M. The optical properties of moth eyes; antireflection surfaces. *Opt. Acta* **29**, 993–1009 (1982).

[12] Boden, S. A. & Bagnall, D. M. Optimization of moth-eye antireflection schemes for silicon solar cells. *Prog. Photovoltaics* **18**, 195–203 (2010).

[13] Yamada, N., Ijiro, T., Okamoto, E., Hayashi, K. & Masuda, H. Characterization of antireflection moth-eye film on crystalline silicon photovoltaic module. *Opt. Express* **19**, A118–A125 (2011).

[14] Ou, Y., Corell, D. D., Dam-Hansen, C., Petersen, P. M. & Ou, H. Antireflective sub-wavelength structures for improvement of the extraction efficiency and color rendering index of monolithic white light-emitting diode. *Opt. Express* **19**, A166–A172 (2011).

[15] Saito, A. *et al.* Numerical analysis on the optical role of nano-randomness on the morpho butterfly's scale. *J. Nanosci. Nanotechno.* **11**, 2785–2792 (2011).

[16] Barber, D. J. & Freestone, I. C. An investigation of the origin of the colour of the lycurgus cup by analytical transmission electron microscopy. *Archaeometry* **32**, 33–45 (1990).

[17] Freestone, I., Meeks, N., Sax, M. & Higgitt, C. The Lycurgus Cup - A Roman nanotechnology. *Gold Bull.* **40**, 270–277 (2007).

[18] Stockman, M. I. Nanoplasmonics: The physics behind the applications. *Phys. Today* **64**, 39–44 (2011).

[19] Klein, G. A. *Industrial Color Physics* (Springer, 2010).

[20] Sharma, G. *Digital Color Imaging Handbook* (CRC Press, 2002).

[21] Højlund-Nielsen, E., Greibe, T., Mortensen, N. A. & Kristensen, A. Single-spot e-beam lithography for defining large arrays of nano-holes. *Microelectron. Eng.* **121**, 104 – 107 (2014).

[22] Gadegaard, N. *et al.* Arrays of nano-dots for cellular engineering. *Microelectron. Eng.* **68**, 162–168 (2003).

[23] Jansen, H., de Boer, M., Legtenberg, R. & Elwenspoek, M. The black silicon method: a universal method for determining the parameter setting of a fluorine-based reactive ion etcher in deep silicon trench etching with profile control. *J. Micromech. Microeng.* **5**, 115 (1995).

[24] Schnell, M., Ludemann, R. & Schaefer, S. Plasma surface texturization for multicrystalline silicon solar cells. In *Photovoltaic Specialists Conference*, 367–370 (2000).

[25] Buestrich, R. *et al.* Ormocers for optical interconnection technology. *J. Sol-Gel Sci. Techn.* **20**, 181–186 (2001).

[26] Plummer, J., Deal, M. & Griffin, P. *Silicon VLSI technology : fundamentals, practice and modeling* (Prentice Hall, 2000).

[27] Saleh, B. & Teich, M. *Fundamentals of photonics* (Wiley, 2007).

[28] Pedrotti, F. L., Pedrotti, L. M. & Pedrotti, L. S. *Introduction to optics* (Pearson Prentice Hall, 2007).

[29] Bao, G., Dobson, D. & Ramdani, K. A constraint on the maximum reflectance of rapidly oscillating dielectric gratings. *SIAM J. Control Optim.* **40**, 1858–1866 (2002).

[30] Ersoy, O. K. *Diffraction, Fourier Optics and Imaging* (John Wiley and Sons, 2006).

[31] O'Shea, D. C., Suleski, T. J., Kathman, A. D. & Prather, D. W. *Diffractive Optics: Design, Fabrication, and Test* (SPIE Press, 2003).

[32] Harvey, J. E., Vernold, C. L., Krywonos, A. & Thompson, P. L. Diffracted radiance: A fundamental quantity in nonparaxial scalar diffraction theory. *Appl. Optics* **38**, 6469–6481 (1999).

[33] Harvey, J. E. Fourier treatment of near-field scalar diffraction theory. *Am. J. Phys.* **47**, 974 (1979).

[34] Moharam, M. G., Gaylord, T. K., Pommet, D. A. & Grann, E. B. Stable implementation of the rigorous coupled-wave analysis for surface-relief gratings: enhanced transmittance matrix approach. *J. Opt. Soc. Am. A* **12**, 1077–1086 (1995).

[35] Grating Diffraction Calculator - GD-Calc, KJ Innovation, Santa Clara, CA, USA.

[36] Raut, H. K., Ganesh, V. A., Nair, A. S. & Ramakrishna, S. Anti-reflective coatings: A critical, in-depth review. *Energy Environ. Sci.* **4**, 3779–3804 (2011).

[37] May, G. S. & Sze, S. M. *Fundamentals of semiconductor fabrication* (Wiley, 2004).

[38] Chandrasekhar, S. *Radiative Transfer* (Dover Publications, 1960).

[39] Wolff, L. B. Diffuse-reflectance model for smooth dielectric surfaces. *J. Opt. Soc. Am. A* **11**, 2956–2968 (1994).

[40] Kaless, A., Schulz, U., Munzert, P. & Kaiser, N. Nano-motheye antireflection pattern by plasma treatment of polymers. *Surf. Coat. Tech.* **200**, 58 – 61 (2005).

[41] Yanagishita, T., Nishio, K. & Masuda, H. Anti-reflection structures on lenses by nanoimprinting using ordered anodic porous alumina. *Appl. Phys. Express* **2**, 022001 (2009).

[42] Ting, C.-J., Huang, M.-C., Tsai, H.-Y., Chou, C.-P. & Fu, C.-C. Low cost fabrication of the large-area anti-reflection films from polymer by nanoimprint/hot-embossing technology. *Nanotechnology* **19**, 205301 (2008).

[43] Morphotonix, Lausanne, Switzerland, http://www.morphotonix.com/.

[44] Saito, A. *et al.* Reproduction, mass production, and control of the morpho butterfly's blue. *Proc. SPIE* **7205**, 720506–720506–9 (2009).

[45] Chung, K. *et al.* Flexible, angle-independent, structural color reflectors inspired by morpho butterfly wings. *Adv. Mater.* **24**, 2375–2379 (2012).

[46] Cao, L., Fan, P., Barnard, E. S., Brown, A. M. & Brongersma, M. L. Tuning the color of silicon nanostructures. *Nano Lett.* **10**, 2649–2654 (2010).

[47] Chung, K. & Shin, J. H. Range and stability of structural colors generated by morpho-inspired color reflectors. *J. Opt. Soc. Am. A* **30**, 962–968 (2013).

[48] Walia, J., Dhindsa, N., Khorasaninejad, M. & Saini, S. S. Color generation and refractive index sensing using diffraction from 2d silicon nanowire arrays. *Small* **10**, 144–151 (2014).

[49] Højlund-Nielsen, E. *et al.* Angle-independent structural colors of silicon. *J. Nanophotonics* **8**, 083988 (2014).

[50] Kanamori, Y., Shimono, M. & Hane, K. Fabrication of transmission color filters using silicon subwavelength gratings on quartz substrates. *Photon. Technol. Lett.* **18**, 2126–2128 (2006).

[51] Christiansen, A., Clausen, J., Mortensen, N. & Kristensen, A. Injection moulding antireflective nanostructures. *Microelectron. Eng.* **121**, 47–50 (2014).

[52] Domine, D., Haug, F. J., Battaglia, C. & Ballif, C. Modeling of light scattering from micro- and nanotextured surfaces. *J. Appl. Phys.* **107**, 044504–044504–8 (2010).

[53] Schröder, S. *et al.* Modeling of light scattering in different regimes of surface roughness. *Opt. Express* **19**, 9820–9835 (2011).

[54] Kurtz, C. N. Transmittance characteristics of surface diffusers and the design of nearly band-limited binary diffusers. *J. Opt. Soc. Am.* **62**, 982–989 (1972).

[55] Chang, S.-I. *et al.* Microlens array diffuser for a light-emitting diode backlight system. *Opt. Lett.* **31**, 3016–3018 (2006).

[56] Ahn, S. H. & Guo, L. J. Large-area roll-to-roll and roll-to-plate nanoimprint lithography: A step toward high-throughput application of continuous nanoimprinting. *ACS Nano* **3**, 2304–2310 (2009).

[57] Chu, K.-Y. & Thompson, A. R. Densities and refractive indices of alcohol-water solutions of n-propyl, isopropyl, and methyl alcohols. *J. Chem. Eng. Data* **7**, 358–360 (1962).

[58] Huovinen, E. *et al.* Mechanically robust superhydrophobic polymer surfaces based on protective micropillars. *Langmuir* **30**, 1435–1443 (2014).

[59] Novotny, L. & Hecht, B. *Principles of nano-optics* (Cambridge university press, 2012).

[60] Maier, S. A. *Plasmonics: Fundamentals and Applications* (Springer, 2007).

[61] Fox, M. *Optical Properties of Solids* (Oxford university press, 2010).

[62] Langhammer, C., Schwind, M., Kasemo, B. & Zoric, I. Localized surface plasmon resonances in aluminum nanodisks. *Nano Lett.* **8**, 1461–1471 (2008).

[63] Ebbesen, T. W., Lezec, H. J., Ghaemi, H. F., Thio, T. & Wolff, P. A. Extraordinary optical transmission through sub-wavelength hole arrays. *Nature* **391**, 667–669 (1998).

[64] Genet, C. & Ebbesen, T. W. Light in tiny holes. *Nature* **445**, 39–46 (2007).

[65] Lee, H.-S., Yoon, Y.-T., shin Lee, S., Kim, S.-H. & Lee, K.-D. Color filter based on a subwavelength patternedmetal grating. *Opt. Express* **15**, 15457–15463 (2007).

[66] Inoue, D. *et al.* Polarization independent visible color filter comprising an aluminum film with surface-plasmon enhanced transmission through a subwavelength array of holes. *Appl. Phys. Lett.* **98**, 093113 (2011).

[67] Xu, T., Wu, Y.-K., Luo, X. & Guo, L. J. Plasmonic nanoresonators for high-resolution colour filtering and spectral imaging. *Nat. Commun.* **1**, 59 (2010).

[68] Kats, M. a., Blanchard, R., Genevet, P. & Capasso, F. Nanometre optical coatings based on strong interference effects in highly absorbing media. *Nat. Mater.* **12**, 20–4 (2013).

[69] Kats, M. a. *et al.* Enhancement of absorption and color contrast in ultra-thin highly absorbing optical coatings. *Appl. Phys. Lett.* **103**, 101104 (2013).

[70] Wu, Y.-K. R., Hollowell, A. E., Zhang, C. & Guo, L. J. Angle-insensitive structural colours based on metallic nanocavities and coloured pixels beyond the diffraction limit. *Sci. Rep.* **3**, 1194 (2013).

[71] Roberts, A. S., Pors, A., Albrektsen, O. & Bozhevolnyi, S. I. Subwavelength plasmonic color printing protected for ambient use. *Nano Lett.* **14**, 783–787 (2014).

[72] Kumar, K. *et al.* Printing colour at the optical diffraction limit. *Nat. Nanotechnol.* **7**, 557–561 (2012).

[73] Tan, S. J. *et al.* Plasmonic color palettes for photorealistic printing with aluminum nanostructures. *Nano Lett.* **14**, 4023–4029 (2014).

[74] Lochbihler, H. & Ye, Y. Two-dimensional subwavelength gratings with different frontside/backside reflectance. *Opt. Lett.* **38**, 1028–30 (2013).

[75] Lochbihler, H. Reflective colored image based on metal-dielectric-metal-coated gratings. *Opt. Lett.* **38**, 1398–1400 (2013).

[76] Yan, M., Dai, J. & Qiu, M. Lithography-free broadband visible light absorber based on a mono-layer of gold nanoparticles. *J. of Opt.* **16**, 025002 (2014).

[77] West, P. *et al.* Searching for better plasmonic materials. *Laser Photon. Rev.* **4**, 795–808 (2010).

[78] Lee, J. R. *Fundamentals of Adhesion* (Springer Science and Buisiness Media, 1991).

[79] Knight, M. W. *et al.* Aluminum plasmonic nanoantennas. *Nano Lett.* **12**, 6000–4 (2012).

[80] Palik, E. *Handbook of Optical Constants of Solids* (Academic Press, San Diego, 1985).

[81] Griffiths, D. J. *Introduction to Electromagnetism* (Prentice Hall, 1999).

[82] Garcia de Abajo, F. J. Colloquium: Light scattering by particle and hole arrays. *Rev. Mod. Phys.* **79**, 1267–1290 (2007).

[83] Prodan, E., Radloff, C., Halas, N. & Nordlander, P. A hybridization model for the plasmon response of complex nanostructures. *Science* **302**, 419–422 (2003).

[84] Väkeväinen, A. I. *et al.* Plasmonic surface lattice resonances at the strong coupling regime. *Nano Lett.* **14**, 1721–1727 (2014).

Paper A

Color effects from scattering on random surface structures in dielectrics

Jeppe Clausen,[1,4] **Alexander B. Christiansen,**[2,4] **Joergen Garnaes,**[3] **N. Asger Mortensen,**[1] **and Anders Kristensen**[2]

[1]*Department of Photonics Engineering, Technical University of Denmark, Oersteds Plads, Building 343, DK-2800 Kgs. Lyngby, Denmark*
[2]*Department of Micro and Nanotechnology, Technical University of Denmark, Oersteds Plads, Building 345B, DK-2800 Kgs. Lyngby, Denmark*
[3]*Danish Fundamental Metrology, Matematiktorvet, Building 307, DK-2800 Kgs. Lyngby, Denmark*
[4]*Both authors have contributed equally.*

[*]*anders.kristensen@nanotech.dtu.dk*

Abstract: We show that cheap large area color filters, based on surface scattering, can be fabricated in dielectric materials by replication of random structures in silicon. The specular transmittance of three different types of structures, corresponding to three different colors, have been characterized. The angle resolved scattering has been measured and compared to predictions based on the measured surface topography and by the use of non-paraxial scalar diffraction theory. From this it is shown that the color of the transmitted light can be predicted from the topography of the randomly textured surfaces.

OCIS codes: (050.1940) Diffraction; (220.4241) Nanostructure fabrication; (330.1690) Color; (290.0290) Scattering.

References and links

1. C. G. Bernhard, "Structural and functional adaptation in a visual system," Endeavour **26**, 79–84 (1967).
2. P. B. Clapham and M. C. Hutley, "Reduction of lens reflexion by the moth eye principle," Nature **244**, 281–282 (1973).
3. S. Kinoshita, S. Yoshioka, and J. Miyazaki, "Physics of structural colors," Rep. Prog. Phys. **71**, 076401 (2008).
4. Y. Yoon, H. Lee, S. Lee, S. Kim, J. Park, and K. Lee, "Color filter incorporating a subwavelength patterned grating in poly silicon," Opt. Express **16**, 2374–2380 (2008).
5. H. Lee, Y. Yoon, S. Lee, S. Kim, and K. Lee, "Color filter based on a subwavelength patterned metal grating," Opt. Express **15**, 15457–15463 (2007).
6. Y. Kanamori, M. Shimono, and K. Hane, "Fabrication of transmission color filters using silicon subwavelength gratings on quartz substrates," IEEE Photon. Technol. Lett. **18**, 2126–2128 (2006).
7. Y. Ye, Y. Zhou, H. Zhang, and L. Chen, "Polarizing color filter based on a subwavelength metal-dielectric grating," Appl. Opt. **50**, 1356–1363 (2011).
8. C. Genet and T. W. Ebbesen, "Light in tiny holes," Nature **445**, 39–46 (2007).
9. X. Hu, L. Zhan, and Y. Xia, "Color filters based on enhanced optical transmission of subwavelength-structured metallic film for multicolor organic light-emitting diode display," Appl. Opt. **47**, 4275–4279 (2008).
10. R. Leitel, A. Kaless, U. Schulz, and N. Kaiser, "Broadband antireflective structures on pmma by plasma treatment," Plasma Process. Polym. **4**, S878–S881 (2007).
11. I. Wendling, P. Munzert, U. Schulz, N. Kaiser, and A. Tünnermann, "Creating anti-reflective nanostructures on polymers by initial layer deposition before plasma etching," Plasma Process. Polym. **6**, S716–S721 (2009).
12. C. Ting, M. Huang, H. Tsai, C. Chou, and C. Fu, "Low cost fabrication of the large-area anti-reflection films from polymer by nanoimprint/hot-embossing technology," Nanotechnology **19**, 205301 (2008).
13. H. Schift and A. Kristensen, "Nanoimprint lithography—patterning of resists using molding," in *Springer Handbook of Nanotechnology*, B. Bhushan, ed. (Springer, 2010), pp. 271–312.

#161219 - $15.00 USD Received 10 Jan 2012; revised 2 Feb 2012; accepted 2 Feb 2012; published 7 Feb 2012

14. L. Sainiemi, V. Jokinen, A. Shah, M. Shpak, S. Aura, P. Suvanto, and S. Franssila, "Nonreflecting silicon and polymer surfaces by plasma etching and replication," Adv. Mater. **23**, 122–126 (2011).
15. H. Jansen, M. d. Boer, R. Legtenberg, and M. Elwenspoek, "The black silicon method: a universal method for determining the parameter setting of a fluorine-based reactive ion etcher in deep silicon trench etching with profile control," J. Micromech. Microeng. **5**, 115–120 (1995).
16. S. Aura, V. Jokinen, L. Sainiemi, M. Baumann, and S. Franssila, "UV-embossed inorganic-organic hybrid nanopillars for bioapplications," J. Nanosci. Nanotechno. **9**, 6710–6715 (2009).
17. D. Domine, F. J. Haug, C. Battaglia, and C. Ballif, "Modeling of light scattering from micro- and nanotextured surfaces," J. Appl. Phys. **107**, 044504 (2010).
18. J. E. Harvey, "Fourier treatment of near-field scalar diffraction theory," Am. J. Phys. **47**, 974 (1979).
19. J. E. Harvey, C. L. Vernold, A. Krywonos, and P. L. Thompson, "Diffracted radiance: a fundamental quantity in nonparaxial scalar diffraction theory," Appl. Opt. **38**, 6469–6481 (1999).

1. Introduction

Nature has demonstrated optical effects such as antireflection and colors based on micro and nanostructures. Well known examples are anti reflective moth eye structures [1,2] and iridescent butterfly wings [3]. This has stimulated biomimetic research on obtaining such functionality by micro and nanofabrication methods. Optical effects that rely solely on surface topography has the potential for cost-efficient manufacturing in cheap polymers by embossing/imprinting or injection molding and can provide an alternative for chemical additives or multilayer deposition requiring vacuum methods.

This paper addresses structural color filters. Such devices have been proposed that are based on either sub-wavelength one dimensional gratings [4–7] or nano-holes in metal surfaces that rely on plasmon enhanced propagation [8, 9]. These filters are all multi-material devices, and require several process steps to fabricate.

The results in this paper show that structural color filters can be produced in a single material, without use of pigments, dyes or multi-material sub wavelength structures. We demonstrate the application of strong scattering on random surface structures with dimensions close to the wavelength of the light. The structures show color effects in the direct transmission of white light, when fabricated in an otherwise fully transparent and colorless material and the textured surfaces thereby work as structural color filters fabricated in a single material. The optical performance of the demonstrated color filters rely on mechanisms different from those of periodic color filters [4–9], which in general have higher efficiencies and smaller spectral widths. On the other hand, the type of filter proposed here will benefit from a much lower fabrication cost.

The fabricated surfaces are characterized optically in transmission measurements and angle resolved scattering measurements. The measured results are compared to results calculated using diffraction theory and topographical information achieved by atomic force microscopy (AFM) and it is shown that for the investigated surface the specular transmittance can be predicted from an AFM-scan.

In recent years several methods for fabricating optically functional structures in polymeric materials have been investigated. For antireflective structures and structural color filters in polymers, the applications typically require large areas, making electron beam lithography inconvenient. Instead, methods like maskless plasma etching have been investigated which can fabricate randomly ordered nanostructures on large areas. The structures can be defined directly in the polymer surfaces e.g. by direct etching with a low pressure plasma [10] or by the use of an initial layer as random masking in a plasma etch [11].

Another approach is to fabricate the structures in a master and subsequently replicate them to the polymer. The replication process can be done by the use of an electroplated mold followed by hot embossing [12] or by casting a soft elastomeric mold from the master and subsequently use it for hot embossing or UV-nano imprint lithograpy (UV-NIL) [13, 14].

#161219 - $15.00 USD Received 10 Jan 2012; revised 2 Feb 2012; accepted 2 Feb 2012; published 7 Feb 2012

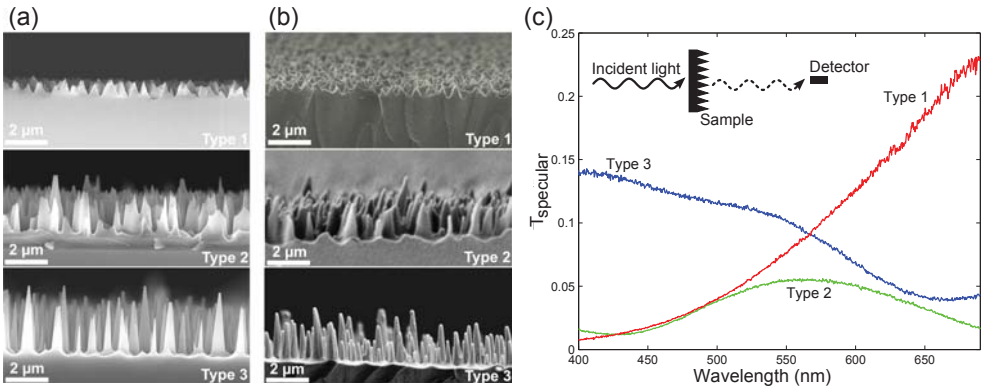

Fig. 1. (a) Three different types of random surface structures fabricated in silicon by reactive ion etching. (b) The corresponding replica in Ormocomp fabricated in an UV-NIL process using a PDMS stamp casted from the silicon surface. The sharp corners of the silicon structures are rounded in the replication process. (c) Transmittance spectra of the three types of Ormocomp surface structures. The spectra are measured normal to the surface for normal incident light. The three types of surfaces appear orange, green, and blue respectively, when seen against a white light source.

2. Experimental section

The random structures were fabricated in silicon using reactive ion etching (RIE-STS Cluster System C004) with a gas mixture of SF_6 (15 sccm) and O_2 (22.5 sccm). The pressure was 300 mTorr, the platen power was 200 W, and the etching time was 10 minutes. The structures appear due to micro masking and the formation of a SiO_xF_y layer, which passivates the silicon surface. The resulting type of structure is determined by the rate of which the passivation is formed and subsequently removed by flourine radicals [15]. Three different types of structures were seen on one wafer. The variations are due to non-uniformities of the etch in the radial direction of the wafer. The three different types of structures are seen in Fig. 1(a). In the center of the wafer the structures are of type 1, at a distance of 10 mm from the edge the structures are of type 2, and 4 mm from the edge the structures are of type 3. All structures have lateral sizes similar to the wavelength of visible light and are therefore not characterized as sub-wavelength structures. As shall be demonstrated this results in scattering of incoming light, and the variations in height, shape, and pitch of the different types of structures lead to different scattering characteristics when replicated in transparent materials.

The structures are replicated in the organic-inorganic hybrid polymer Ormocomp (Micro resist technology Gmbh, Berlin) based on the method described by Sainiemi *et al.* [14], where an elastomeric stamp is casted from the silicon and used in UV-NIL. The PDMS (Sylgard 184, Dow Corning) was mixed as recommended by the manufacturer and poured onto the master and left for degassing in a desiccator for 30 minutes prior to curing (65 degrees Celsius for 3 hours). The silicon master was coated with FDTS for anti adhesion.

Ormocomp was spin coated on a glass substrate to a thickness of approximately 50 μm. The imprints were performed in an Obducat NIL Imprinter 2.5 at room temperature with a hydrostatic pressure on the backside of the PDMS stamp (10 bar) for 10 minutes. The Ormocomp was cured with a UV-light source (1000 W for 10 minutes) through the glass substrate and the stamp was subsequently removed. The resulting replica of the silicon master are seen in Fig. 1(b). As expected from earlier reports the replicated structures are rounded [14, 16], but the main characteristics of the various structures are maintained in the replica.

#161219 - $15.00 USD Received 10 Jan 2012; revised 2 Feb 2012; accepted 2 Feb 2012; published 7 Feb 2012

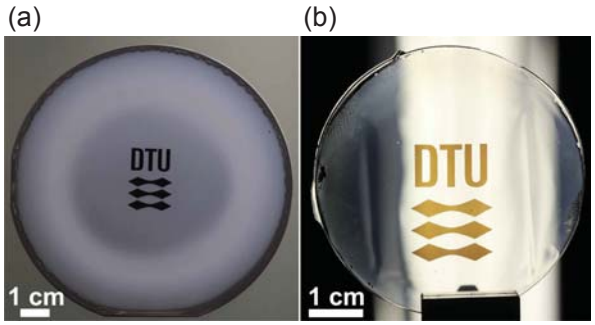

Fig. 2. (a) Silicon master with a black DTU-logo fabricated by selective removal of the surface structures around the logo using photolithography and isotropic silicon etching. The structures in the logo are of type 1 (Fig. 1(a)). (b) Replication in an Ormocomp film on a glass substrate fabricated by UV-NIL with a PDMS stamp casted from the master. When seen against a white light source the logo appears orange.

By using UV lithography the structures can be fabricated in specific patterned areas to make color filters of any macroscopic design. An example is seen in Fig. 2(a), where the pattern is seen as a black logo in the center of the silicon master. The structures in the logo are of type 1 and the corresponding replication is seen in Fig. 2(b). Here, the macroscopic logo is comprising wavelength scale structures not visible to the naked eye, yet causing the logo to appear orange when seen against the white light illumination.

All optical measurements were performed using a homebuild setup. The samples were illuminated at normal incidence with white light (Xenon lamp, HPX-2000). The light was collected in a fiber (500 μm in diameter) and analyzed in a spectrometer (Jaz, Ocean Optics). The setup made it possible to move the detecting fiber to any desired angle with respect to the sample.

AFM-images were scans of 20×20 μm^2 with a resolution of 512×512 pixels. The size of the scanned area influences the resolution of the scattering angle in the calculations [17] and is chosen such that good angular resolution is achieved while maintaining a sufficient spatial resolution in the AFM scan. The tip used was a high aspect ratio tip (Improved Super Cone type 125C40-R). Specifications according to the manufacturer: Tip height $>$ 7 μm, radius $<$ 10 nm, and full cone angle $<$ 10 degrees. The AFM used was a Metrology AFM based on a Dimension 3100 from Digital Instruments, Veeco Metrology Group (now Bruker) and a metrology head based on piezoelectric flexures equipped with capacitive distance sensors. All measurements were carried out in dynamic resonant mode.

3. Results and discussion

The structures have been characterized in the visible range from 400-700 nm. The specular transmission of light of the three types of structures is shown in Fig. 1(c). The quite different geometry of the three types also results in very different transmission spectra. The transmission spectrum of structures of type 1 shows much higher specular transmission for long wavelengths than for short wavelengths. The reason for this is wavelength dependent scattering which occurs at the structured surface, where light with short wavelength is scattered more than light with long wavelength. The opposite is the case for the transmission spectrum of type 3, where red light is scattered more than blue light. For type 2 a peak in the transmission at 560 nm is observed. The three different transmission spectra illustrate the color appearance of the different areas of the imprint when seen against white light. Type 1 appears orange, type 2 appears green, and type 3 appears blue. In order to investigate the scattering behavior in more detail,

#161219 - $15.00 USD Received 10 Jan 2012; revised 2 Feb 2012; accepted 2 Feb 2012; published 7 Feb 2012

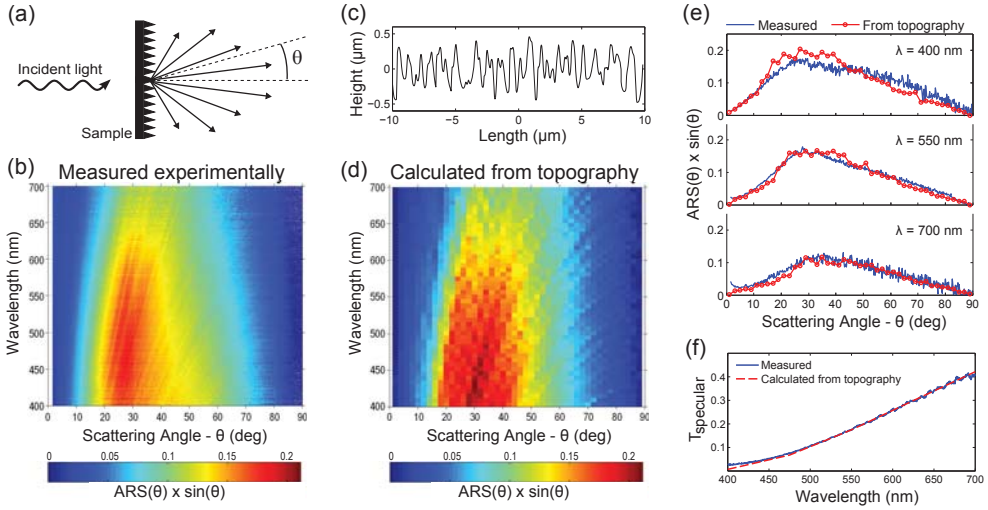

Fig. 3. (a) Sketch of the measurement geometry for angle resolved measurements. The data are collected with normal incident light and the detector is moved to various angles measuring the intensity as function of θ. (b) Measured angular resolved scattering ARS(θ) for visible wavelengths. The data are multiplied by a factor of $\sin\theta$ to achieve a probability distribution. (c) Typical profile from two dimensional scan recorded by AFM used for the modeling. (d) ARS(θ) calculated from a 20×20 μm^2 scan of the surface topography. The data are normalized to all propagating modes and multiplied by $\sin\theta$. (e) Comparison of the experimentally measured data and the data calculated from the surface topography for three different wavelengths. (f) Comparison of the measured specular transmittance and the specular transmittance calculated from the measured surface topography.

measurements of the angle resolved scattering (ARS) were performed on another sample with similar scattering characteristics as type 1 in Fig. 1(c). Under normal incident light, the transmitted intensity was measured as a function of scattering angle θ as illustrated in Fig. 3(a). The transmission haze $H_T = T_{\text{diff}}/T_{\text{total}}$ is the probability that an incoming photon is diffusely scattered [17]. The specular transmitted light T_{specular} and the transmission haze are related as $T_{\text{specular}} = 1 - H_T$. In Fig. 3(b), the intensity normalized to the intensity of the incoming light is plotted as function of wavelength and scattering angle. In order to convert the data to a probability distribution, they are multiplied by a factor of $\sin\theta$ and for each wavelength the data are normalized such that 2π times the integral over θ equals the transmission haze [17]. The light is most probable to be diffracted to an angle around 30 degrees and the shorter wavelengths are most likely to be scattered. This explains the orange color of the specular transmitted light.

ARS must be intimately connected to the surface topography. The measured ARS has been compared to predictions based on measurement of the surface topography and diffraction theory. The surface topography was measured by AFM and a typical profile from an AFM scan is seen in Fig. 3(c). The model is based on non-paraxial scalar diffraction theory [18, 19] and the used method is described in detail by Domine *et al.* [17].

While the overall qualitative agreement is seen by comparison of Fig. 3(b) and 3(d), the quantitative agreement can be evaluated in more detail in Fig. 3(e), where experimentally measured results and the results achieved from topographical information are compared directly for three different wavelengths. It is seen that the model predicts the scattering behavior of the surface structures very well.

It is also possible to make predictions for the specular transmittance using the surface to-

#161219 - $15.00 USD Received 10 Jan 2012; revised 2 Feb 2012; accepted 2 Feb 2012; published 7 Feb 2012

pography as the only input. In Fig. 3(f) the calculated and measured values of the specular transmittance are plotted as function of wavelength for the investigated surface. While a deviation is seen for wavelengths shorter than 500 nm, the model fits the measured data very well in the rest of the considered interval and the color appearance can be predicted from the AFM image.

The quality of the measured AFM data has proven to be important for the achieved result. The tips used were specially designed for high aspect ratio surfaces in order to be able to resolve relevant features of the surface. The same analysis has been carried out using a standard AFM tip. The result of this analysis showed an increase in the specular transmittance over the entire wavelength interval of up to 0.1 compared to the measured data shown in Fig. 3(f).

Although the AFM measurements have proven adequate for the topographical characterization of the investigated surface, it would be less straight forward to characterize surfaces with structures of higher aspect ratio in detail. This is for example the case for the surfaces of type 2 and type 3 in Fig. 1(b) because the shape of the AFM tip would influence the observed topography more significantly. For prediction of the transmittance for surfaces with such high aspect ratios one may have to investigate other techniques or thoroughly approximate the tip shape and correct for the influence on the observed topography.

4. Conclusion

In conclusion, a route to the realization of cheap single material color filters has been demonstrated based on the concept of light scattering on surface structures. Three distinct colors have been observed for three different surfaces. The scattering characteristics could be reproduced from topographical data and the specular transmittance spectrum could be predicted from a simple model which opens up new avenues for design of single-material plastic color filters.

Acknowledgments

The work was supported by the EC FP7 funded NaPANIL (Contract No. 214249) project and the NanoPlast project funded by the Danish National Advanced Technology Foundation (File No.: 007-2010-2). We thank professor Ole Sigmund for fruitful discussions, and acknowledge Emil Hoejlund-Nielsen and Thomas Buss for experimental assistance.

#161219 - $15.00 USD Received 10 Jan 2012; revised 2 Feb 2012; accepted 2 Feb 2012; published 7 Feb 2012

Paper B

Minimizing scattering from antireflective surfaces replicated from low-aspect-ratio black silicon

Alexander B. Christiansen,[1] Jeppe Clausen,[2] N. Asger Mortensen,[2] and Anders Kristensen[1,a)]
[1]*Department of Micro and Nanotechnology, Technical University of Denmark, Oersteds Plads, Building 345B, DK-2800 Kgs. Lyngby, Denmark*
[2]*Department of Photonics Engineering, Technical University of Denmark, Oersteds Plads, Building 343, DK-2800 Kgs. Lyngby, Denmark*

(Received 2 July 2012; accepted 11 September 2012; published online 24 September 2012)

The scattering properties of randomly structured antireflective black silicon polymer replica have been investigated. Using a two-step casting process, the structures can be replicated in Ormocomp on areas of up to 3 in. in diameter. Fourier analysis of scanning electron microscopy images of the structures shows that the scattering properties of the surfaces are related to the spatial periods of the nanostructures. Structures with a dominating spatial period of 160 nm, a height of 200 nm, and aspect ratio of 1.3 show insignificant scattering of light with wavelength above 500 nm and lower the reflectance by a factor of two. © *2012 American Institute of Physics*.
[http://dx.doi.org/10.1063/1.4754691]

Antireflective nanostructures have the potential to provide an alternative to expensive coatings for optical components. High aspect ratio structures with periods around 200 nm have been shown to greatly reduce Fresnel reflections for a broad band of wavelengths.[1] Such periodic structures can be fabricated on large areas by laser interference lithography[2] or by anodized aluminium oxide.[3] An important feature of this kind of structure is that below a certain ratio between period and wavelength, only zeroth order diffraction will occur at the surface, and no light will be scattered.[4,5] Minimizing scattering is crucial when the antireflective element is to remain fully transparent and increase the direct transmission of light. Only recently, the scattering properties due to imperfections in periodic structures have been studied.[6]

Another method for fabricating antireflective surfaces is by pattern transferral of the nanostructures in black silicon (BSi) surfaces. BSi structures are randomly positioned, cone-shaped formations, formed in silicon by a mask-less etching process.[7] However, due to the random nature of these structures, such surfaces will inherently scatter incoming light. Several studies have used this type of structures for antireflection,[8–10] but the scattering properties of the surfaces have only recently been addressed.[11]

In this letter, we present a simple method for replicating BSi structures into Ormocomp, a transparent organic-inorganic hybrid polymer (Micro resist technology Gmbh, Berlin), on areas of up to 3 in. in diameter. The silicon masters were characterized by scanning electron microscopy (SEM) and dark field microscopy, and the Ormocomp replica were characterized by SEM and Fourier analysis, and light transmission measurements. The structures which showed increased transmission for light with a wavelength down to 500 nm were used to demonstrate the antireflective effect, which was significant even for structures with aspect ratio as low as 1.3.

a)Electronic mail: anders.kristensen@nanotech.dtu.dk.

The BSi substrates were structured by reactive ion etching (Pegasus DRIE, STS). The structures were formed in a single etching cycle with an O_2/SF_6 -based etch.[7] By varying the gas-flows and platen power, different types of BSi surfaces were fabricated, denoted from hereon as types A-F.

After etching the BSi substrates [See Fig. 1(a1)], the surface can be patterned using conventional photolithography and dry etching to remove the nanostructures from the defined areas (a2). Using molecular vapor deposition, the BSi masters were coated with an anti-stiction layer. Ormocomp was poured on the master (a3) and a 1.5 mm thick and 4 in. wide polymethylmethacrylate (PMMA) substrate was placed on top. The thickness of the Ormocomp film was controlled by placing spacers at the periphery, between the master and PMMA back plate. The Ormocomp was cured with UV light in the wavelength range of 260–320 nm, through the PMMA (a4). The type of PMMA is Plexiglas XT 20070, which has a limited but sufficient transmittance in the 260–320 nm range. After UV exposure, the flexibility of the Ormocomp and PMMA allowed for the gradual releasing of the Ormocomp film from the BSi master, while the Ormocomp remained attached to the PMMA (a5). Finally, the Ormocomp Mother stamp was coated with an anti-stiction layer.

Samples with structures on a single face were fabricated by pouring Ormocomp on the Mother stamp and placing a PMMA backplate on top. The Ormocomp was again cured with UV light, through the PMMA, as shown in Figs. 1(b1) and 1(b2). Two identical Ormocomp Mother stamps were used to fabricate samples with identical antireflective structures on the front and back face, see Fig. 1(c). A comparison of the structures on a BSi master and the final Ormocomp sample is shown in Figs. 1(d1) and 1(d2).

The silicon masters and the final Ormocomp samples were characterized by SEM top and side view micrographs. The relative scattering properties of the structures were characterized with a dark field optical microscope (Nikon Eclipse L200). The microscope was calibrated with a highly

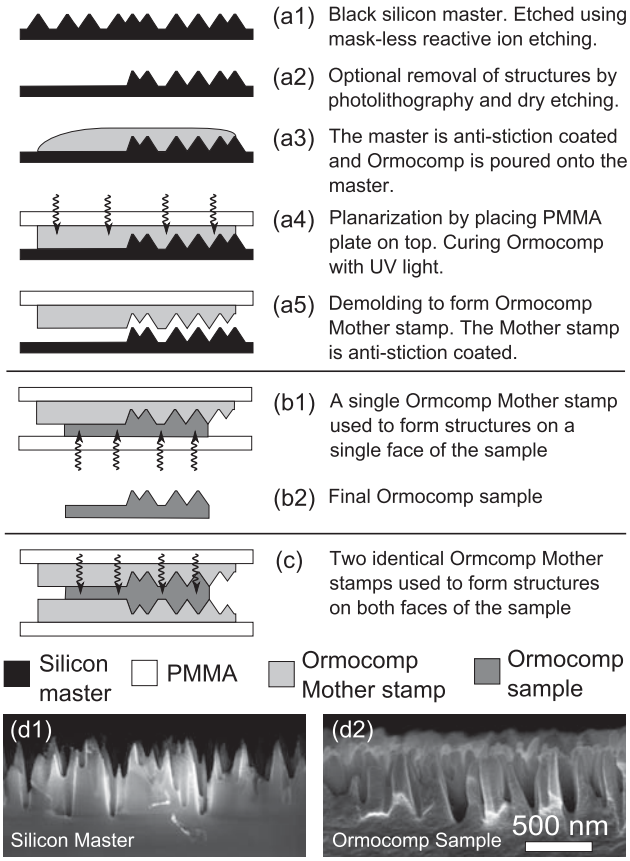

FIG. 1. (a) Process for fabricating Ormocomp Mother stamps. A black silicon master is formed by mask-less reactive ion etching. Selected areas can be removed using conventional photolithography and dry etching. The master is anti-stiction coated and Ormocomp is poured onto the master. A PMMA plate is placed on top, planarizing the Ormocomp film. The Ormocomp is cured with UV light and the Mother stamp is released. (b) The final Ormocomp sample is formed from the Mother stamp similar to steps (a3) and (a4). (c) Using two identical Mother stamps, a sample can be formed with identical nanostructures on each face. (d1) Side view SEM of a black silicon master. (d2) The final Ormocomp sample which was replicated from the Mother stamp.

scattering sample (type F, see Fig. 2), and the exposure settings and white balance were fixed for all recorded images. Thus, the relative scattering properties of the six types of surfaces can be characterized.

Power spectral densities of each Ormocomp sample were calculated from the top view SEM images by azimuthal averaging of the 2D Fourier spectrum of the surface.[12] This allows for identifying the dominating spatial frequency of the randomly ordered structures.

For the direct transmission measurements, the samples were illuminated at normal incidence with white light (Xenon lamp, HPX-2000, Ocean optics), through a fiber and a collimator. The samples were aligned perpendicular to the incident light using a goniometer. The light was then collected in a fiber with a collimator and analyzed in a spectrometer (Jaz, Ocean Optics). Thus, only non-scattered, directly transmitted light was collected by the collimator.

Angle resolved scattering (ARS) measurements were performed using the same setup, by rotating the collecting fiber around the axis of the illuminated sample. The scattered transmitted light was collected at an angle (θ) from the normal, in the range 15° to 90°.

Figures 2(a) and 2(b) show SEM images of the BSi masters as viewed from the side and top, respectively. Fig. 2(c) shows dark field microscope images of the BSi masters. Fig. 2(d) shows photographs of the fabricated Ormocomp samples, when illuminated by an intense white light source (Xenon lamp). The samples were illuminated at normal incidence and photographed from an oblique angle. The results shown in Figs. 2(c) and 2(d) offer a simple comparison of the relative scattering properties of the different BSi masters and the final Ormocomp samples, respectively.

Figure 3(a1) shows the intensity of transmitted, scattered light, measured at an angle of $\theta = 30°$, for the six different Ormocomp samples. The intensity of the scattered light varies within two orders of magnitude when comparing the different samples. The results show that for all samples, the shorter wavelengths are scattered significantly stronger than the longer wavelengths. Figs. 3(a2) and 3(a3) show surface plots of the full ARS measurements of samples C and A, respectively.

Figure 3(b) shows the power spectral density of a top view SEM image of a type A Ormocomp sample. The black lines show a fit to a power function of the first and last parts of the data. The intersection of the two lines thus marks the dominating spatial frequency, q, of the surface structures, and the error bars represent a 95% confidence interval on q, based on the uncertainties of the parameters of the two fitted functions. Power spectra for the other Ormocomp samples were analyzed in a similar manner, and the intersections are denoted by squares.

Figure 3(c) shows direct transmission measurements of planar and structured Ormocomp samples. For clarity, sample F is not shown as the transmission is below 0.5 throughout the spectrum. Most samples show antireflective properties at a wavelength of 900 nm, while only sample A

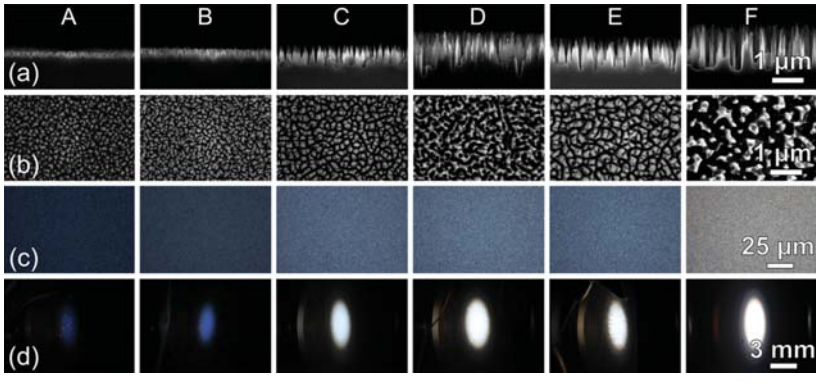

FIG. 2. (a) Side view SEM of BSi. (b) Top view SEM image of BSi. (c) Dark field optical micrographs of BSi. (d) Photographs of fabricated Ormocomp samples. Samples were illuminated by a powerful white light source under normal incidence, and the scattered light was photographed at an oblique angle.

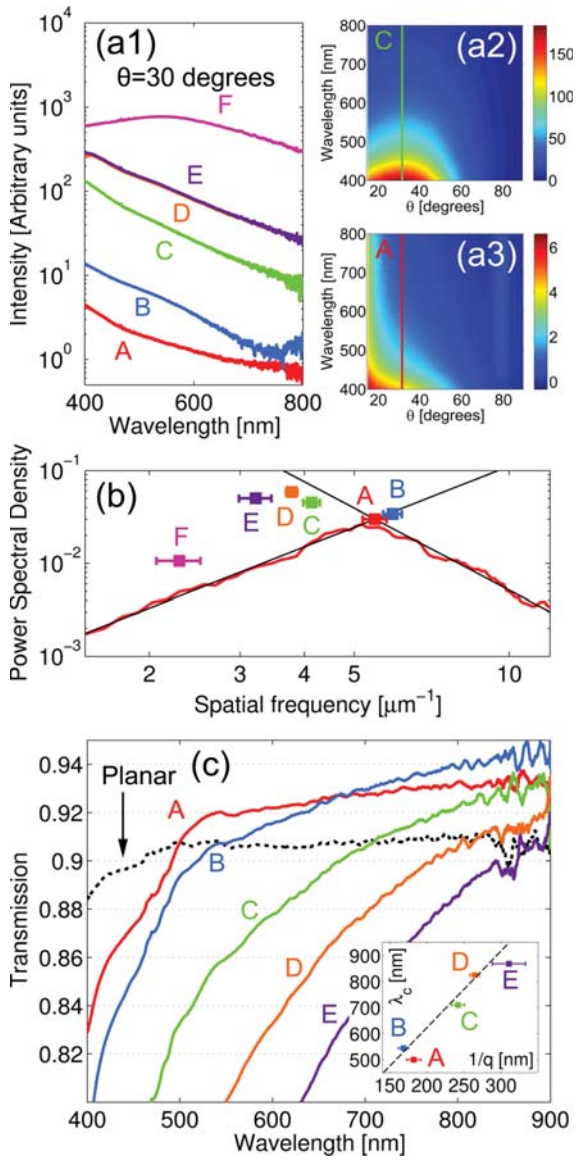

FIG. 3. (a1) Intensity of transmitted, scattered light, measured at an angle of $\theta = 30°$, for the six different Ormocomp samples. (a2) and (a3) Surface plots of the full ARS measurements of samples C and A, respectively. (b) Power spectral density of type A Ormocomp sample. The square marked A is the dominating spatial frequency, q, found by fitting, with a 95% confidence interval. Squares marked B-F indicate q for other types of surfaces. (c) Direct transmission measurements of Ormocomp samples with antireflective structures on one face. Inset: Wavelength at intersection between transmission spectra of planar and structured surfaces, λ_c, as a function of the dominating structural periods, q^{-1}.

and B show increased transmission down to 500 nm and 550 nm, respectively. Samples C, D, and E show reduced transmission in the entire visible spectrum due to scattering. It is evident that the structures of type A, with aspect ratio of 1.3 and height of 200 nm, reduce the reflectance by a factor of 2, from 4% and down to 2% in the visible spectrum.

The inset in Fig. 3(c) shows the wavelength of the intersection of each transmission line with the planar line, denoted λ_c, as a function of the dominating structural periods, q^{-1}, found in Fig. 3(b). The plot thus correlates the spatial frequency of the surface structures to the scattering properties. This central result shows that larger values of q lower the cut-off wavelength, λ_c, at which scattering becomes significant.

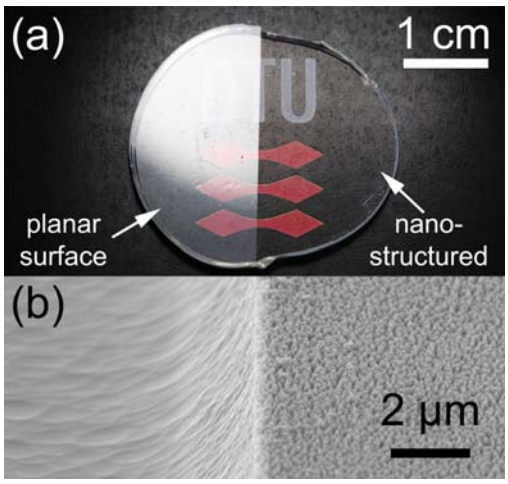

FIG. 4. (a) Photograph of Ormocomp sample with antireflective nanostructures on top and bottom face, placed on a sheet of paper with a printed logo. Nanostructures are on the right side of the fully transparent sample. (b) SEM image of the sample, showing the difference between the planar (left) and the nanostructured surface (right).

This shows that replica of BSi structures are viable for increasing transmission of light in the visible spectrum, despite the random nature on the structures. Furthermore, the scattering properties can be estimated simply from a top view SEM image.

Finally, the type A structures were used to fabricate a sample with nanostructures on both faces, see Fig. 1(c). The resulting sample is shown in Fig. 4(a), where the transparent Ormocomp disc is placed on a sheet of paper with a printed logo. On the left side, the light from a lamp is reflected specularly from the planar top and bottom surface of the sample. On the right side, nanostructures covering both the top and the bottom faces suppress part of the Fresnel reflections, rendering the underlying surface visible. We note that the scattered blue light is too dim to see in daylight conditions.

In conclusion, we have shown that the spatial frequencies of BSi structures are related to the scattering properties of the antireflective surfaces. Structures with a dominating spatial frequency of 160 nm, a height of 200 nm, and aspect ratio of 1.3 show insignificant scattering of light with wavelengths above 500 nm and reduce Fresnel reflections by up to a factor of 2. Using a simple two-step casting process, the structures can be fabricated in Ormocomp on areas of up to 3 in. in diameter.

We thank Ole Sigmund, Johannes Weirich, and Jakob Birkedal Wagner for fruitful discussions. The work was supported by the NanoPlast project funded by the Danish National Advanced Technology Foundation (File No. 007-2010-2).

[1]H. K. Raut, V. A. Ganesh, A. S. Nair, and S. Ramakrishna, Energy Environ. Sci. **4**, 3779 (2011).
[2]K.-C. Park, H. J. Choi, C.-H. Chang, R. E. Cohen, G. H. McKinley, and G. Barbastathis, ACS Nano **6**, 3789 (2012).
[3]H. Deniz, T. Khudiyev, F. Buyukserin, and M. Bayindir, Appl. Phys. Lett. **99**, 183107 (2011).
[4]E. B. Grann, M. G. Moharam, and D. A. Pommet, J. Opt. Soc. Am. A **11**, 2695 (1994).
[5]H. S. Jang, J. H. Kim, K. S. Kim, G. Y. Jung, J. J. Lee, and G. H. Kim, J. Nanosci. Nanotechnol. **11**, 291 (2011).

[6]D. Lehr, M. Helgert, M. Sundermann, C. Morhard, C. Pacholski, J. P. Spatz, and R. Brunner, Opt. Express **18**, 23878 (2010).
[7]G. Kumaravelu, M. Alkaisi, and A. Bittar, in *Photovoltaic Specialists Conference, 2002. Conference Record of the Twenty-Ninth IEEE* (2002), pp. 258–261.
[8]L. Sainiemi, V. Jokinen, A. Shah, M. Shpak, S. Aura, P. Suvanto, and S. Franssila, Adv. Mater. **23**, 1 (2011).
[9]C.-C. Hong, P. Huang, and J. Shieh, Macromolecules **43**, 7722 (2010).
[10]C.-J. Ting, M.-C. Huang, H.-Y. Tsai, C.-P. Chou, and C.-C. Fu, Nanotechnology **19**, 205301 (2008).
[11]J. Clausen, A. B. Christiansen, J. Garnaes, N. A. Mortensen, and A. Kristensen, Opt. Express **20**, 4376 (2012).
[12]S. Schroeder, A. Duparre, L. Coriand, A. Tuennermann, D. H. Penalver, and J. E. Harvey, Opt. Express **19**, 9820 (2011).

Paper C

Enhancing the chroma of pigmented polymers using antireflective surface structures

Jeppe S. Clausen,[1,*] Alexander B. Christiansen,[2] Anders Kristensen,[2] and N. Asger Mortensen[1]

[1]Department of Photonics Engineering, Technical University of Denmark, Oersteds Plads, Building 343, DK-2800 Kgs. Lyngby, Denmark

[2]Department of Micro and Nanotechnology, Technical University of Denmark, Oersteds Plads, Building 345B, DK-2800 Kgs. Lyngby, Denmark

*Corresponding author: jepcl@fotonik.dtu.dk

Received 13 August 2013; revised 9 October 2013; accepted 15 October 2013; posted 16 October 2013 (Doc. ID 195160); published 8 November 2013

In this paper we investigate how the color of a pigmented polymer is affected by reduction of the reflectance at the air–polymer interface. Both theoretical and experimental investigations show modified diffuse-direct reflectance spectra when the reflectance of the surface is lowered. Specifically it is found that the color change is manifested as an increase in chroma, leading to a clearer color experience. The experimental implementation is done using random tapered surface structures replicated in polymer from silicon masters using hot embossing. © 2013 Optical Society of America

OCIS codes: (330.1690) Color; (120.5700) Reflection; (310.1210) Antireflection coatings; (310.6628) Subwavelength structures, nanostructures.

http://dx.doi.org/10.1364/AO.52.007832

1. Introduction

Colored plastic is present everywhere in modern society. Many consumer products are fabricated using pigmented polymers and the appearance is an important parameter in the customer valuation of the product. In this work we suggest a method for increasing the chroma of pigmented polymers by the use of antireflective structures (ARS) in the surface of the polymer. The method may be used as selective decoration of certain areas of a surface or across the entire surface of the polymer part for general modification of the appearance.

Subwavelength ARS inspired by the eye of the moth [1] have previously been investigated in great detail as a cost-efficient alternative to expensive single or multilayer coatings deposited using vacuum equipment. The structures can, when employed on optical components such as lenses, greatly reduce the surface reflections [2–4]. Also within silicon [5–7] and III-V [8,9] technologies ARS are used, e.g., for increasing the efficiency of photovoltaic devices.

Antireflective coatings are used in various consumer products to improve functionality or appearance. In display technology antireflective coatings fabricated using thin film technologies can be used to improve the contrast ratio [10,11]. Within the textile industry various coatings applied to fabrics made from dyed polyethylene terephthalate have been used to improve the color by limiting surface reflections from the single fabric fibers [12].

In this work the ARS are introduced in the surface of colored plastic in order to modify the way the incoming light is transmitted into the polymer, thereby also modifying the interaction with the pigment. When light is incident onto a surface of a pigmented dielectric material a certain amount, determined by the refractive index and incident

1559-128X/13/327832-06$15.00/0

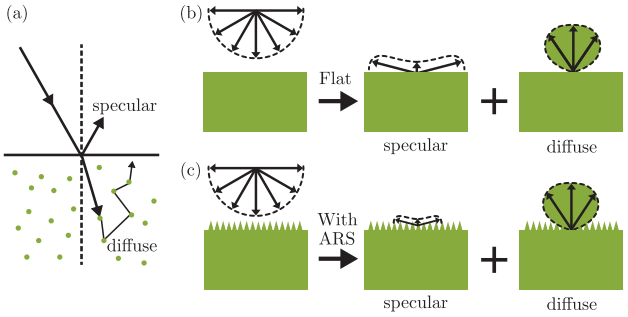

Fig. 1. (a) Illustration of specular and diffuse reflection of a light ray for a pigmented polymer. (b) Surface and bulk reflections of a pigmented polymer under diffuse illumination in the case of flat surface. (c) The surface reflectance is lowered in the presence of ARS.

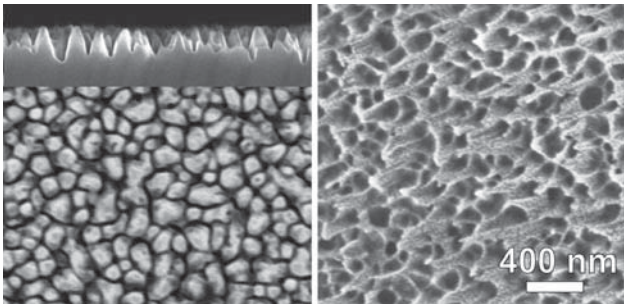

Fig. 2. Left: scanning electron micrographs of a silicon master seen from the top and from the side. Right: ABS surface after embossing (a thin layer of gold has been applied for imaging). The scale bar applies to all images. The random subwavelength nature of the ARS is evident.

angle, is reflected due to Fresnel reflection, as illustrated in Fig. 1(a). The light transmitted through the surface interacts with the pigment in a scattering process and a diffuse flux is reflected with the color of the pigment. In daily life, the incoming illumination may often be approximated by perfect diffuse illumination, as in Fig. 1(b). An observer will see the sum of the specular and the diffuse bulk reflections due to this incident radiance. By reducing the reflection at the surface, the amount of light that does not interact with the pigment is reduced and the color appearance will change, see Fig. 1(c).

The surface structures used in this study have low aspect ratio and the fabrication may therefore be done by high-throughput replication methods, such as embossing or injection molding. The effect is demonstrated in acrylonitrile butadiene styrene (ABS), one of the most widely used thermoplastics for consumer products.

2. Experimental Procedure

The ARS were fabricated on silicon wafers and then replicated in ABS in a hot embossing replication step [13]. The structures were fabricated using reactive ion etching, in a gas mixture of O_2 and SF_6 leading to randomized tapered subwavelength structures. The antireflective properties of this type of structure replicated in transparent materials have been investigated in earlier work where it was found that the reflection was reduced by a factor of 2 and only a small amount of scattering was introduced [14]. This type of structure was chosen due to the random subwavelength nature, thereby avoiding the existence of distinct diffraction orders, which would be present in holographically generated periodic structures. The surface structures are seen in scanning electron micrographs of a nanostructured silicon master in the left part of Fig. 2. The tapered structures are approximately 200 nm high. After etching, the silicon wafers were coated with perfluorodecyltrichlorosilane (FDTS) using molecular vapor deposition for easy release of the stamp after embossing.

Blue, green, and red flat substrates (5 cm diameter) for embossing were fabricated by injection molding. They were fabricated using the same unpigmented ABS and colored using master batches of the three different colors.

Hot embossing was performed in a parallel plate press at a temperature of 120°C and a constant force of 2.5 kN (corresponding to a pressure of approximately 13 bar) for 10 min followed by cooling to 80°C before releasing the pressure. A top view of the embossed surface is seen in the right part of Fig. 2. Samples with flat surfaces were fabricated using the same parameters, but with polished FDTS coated silicon wafers as stamps.

The diffuse-direct reflectance of the samples was measured using an integrating sphere (ISP-50-8-R-GT, Ocean Optics) with diffuse illumination of the sample and the detecting fiber at 8 deg with respect to the surface normal. The specular component was included in the measurements. This configuration, typically denoted $d{:}8$ [15], simulates daylight conditions in a situation with no direct light sources and near to normal observation. This configuration is chosen to include the specular contribution to the observed reflection in the color evaluation since this is a major contribution to the color changes described here. The light source was an unfiltered xenon lamp (HPX-2000, Ocean Optics), and for detection we used a spectrometer (Jaz, Ocean Optics). A white reflectance standard (WS-1, Ocean Optics) was used as reference sample.

The surface gloss was measured as the difference in reflectance with and without the specular component included in a direct-diffuse ($8{:}d$) measurement using the same integrating sphere. For the flat surface it was just below 4% corresponding to the Fresnel reflectance of the surface. For the structured surface it was below 0.5%. This reduction in gloss is mainly due to reduction in the surface reflectance, not scattering at the surface.

3. Theoretical Treatment

The goal is to determine how a modification of the surface reflectance will change the observed color under given lighting conditions. The system under consideration is a slab of pigmented polymer surrounded by air. The polymer has refractive index n.

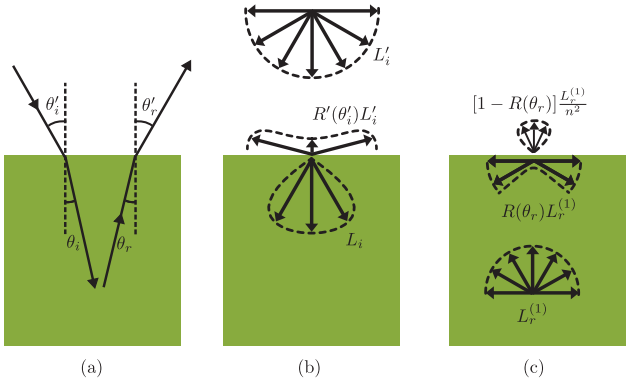

Fig. 3. (a) Definition of the angles of the incident and reflected light. (b) Illustration of the transmission of diffusive flux through the surface of the polymer. (c) The first-order diffuse reflectance from the bulk and the transmission and reflection of this flux. Figure inspired by [15].

The altered reflection properties of the surface after introduction of ARS are modeled by introduction of a parameter α, which is simply the ratio between the new reflectance and the normal Fresnel reflectance. For external reflections of the light incident at angle θ_i' [see Fig. 3(a)] the lowered reflectance R' becomes

$$R'(\theta_i') = \alpha R_f'(\theta_i'), \tag{1}$$

where R_f' is the external Fresnel reflectance for unpolarized light at the corresponding flat interface. For the internal case with the reflected light approaching the surface at an angle θ_r, the new reflectance R becomes

$$R(\theta_r) = \begin{cases} \alpha R_f(\theta_r) & \text{for } \theta_r \le \theta_c \\ 1 & \text{for } \theta_r > \theta_c \end{cases}, \tag{2}$$

where $\theta_c = \arcsin(1/n)$ is the critical angle and R_f is the internal Fresnel reflectance of unpolarized light. Here it is assumed that no scattering is introduced by the structures, thereby maintaining total internal reflection. This causes an apparent discontinuity at the critical angle for $\alpha < 1$. In reality there is a small amount of scattering, which will enable outcoupling of light near the critical angle thereby smearing out this discontinuity. The no scattering assumption is based on a small dominating period of the random structures of 180 nm, obtained from the power spectral density [14] opposed to surfaces with random structures on longer length scales [16].

The no scattering assumption also implies that Snell's law is still valid and can be applied for all light transmitted through the surface. It is also assumed that α is independent on the incident angle.

The illumination that will be used throughout the rest of this paper is diffuse light, as illustrated in Fig. 3(b). The incident diffuse light has a constant radiance, L_i', which will give rise to a partly diffuse flux below the surface with angle-dependent radiance L_i given by

$$L_i(\theta_i) = \begin{cases} [1 - R'(\theta_i')]n^2 L_i' & \theta_i \le \theta_c \\ 0 & \theta_i > \theta_c \end{cases}. \tag{3}$$

The scattering of light in the pigmented material is described using the scattering theory developed by Chandrasekhar [17], assuming isotropic scattering. In the case of a semi-infinite substrate the diffusely reflected light can be described by one parameter, the wavelength dependent single scattering albedo, ρ, defined as

$$\rho = \frac{S}{S+K}, \tag{4}$$

where S and K are the scattering and absorption coefficients, respectively. For the conservative case we therefore have $\rho = 1$, while pure absorption is characterized by $\rho = 0$. In the case of a slab of finite thickness one will, in addition to the single scattering albedo, need the optical thickness of the slab to characterize the system. However, in this description we will approximate all samples as semi-infinite substrates. Inside the scattering medium the bidirectional reflectance distribution function, f_r, [18] is given by [17]

$$f_r = \frac{dL_r}{dE_i} = \frac{\rho}{4\pi}\frac{1}{\mu_i + \mu_r} H_\rho(\mu_i) H_\rho(\mu_r). \tag{5}$$

Here, dL_r is the reflected radiance due to incident irradiance dE_i and $\mu = \cos(\theta)$. The function $H_\rho(\mu)$ is dependent on ρ and the level of approximation applied to the radiative transfer equation. While the scattering particles in the description of Chandrasekhar are embedded in a medium with refractive index being the same inside and outside of the scattering atmosphere, Wolff [19] derived a closed-form expression for the case of different refractive indices, thereby including the Fresnel reflection at the boundary between the incident and scattering media. The reflected light from the bulk is partly internally reflected at the surface and higher-order diffuse reflections are present. By summing all these higher-order contributions the reflected radiance can be found, and for $\rho > 0.6$ the closed-form expression derived by Wolff is a good approximation. The same approach is taken here except that all integrals are evaluated numerically in order to include low single scattering albedo. The first-order diffusive reflected radiance below the surface is given by

$$\begin{aligned} dL_r^{(1)} &= f_r(\cos\theta_i, \cos\theta_r) dE_i \\ &= f_r(\cos\theta_i, \cos\theta_r) L_i \cos\theta_i d\omega_i, \end{aligned} \tag{6}$$

and by integration over all solid angles the reflected part is found to be

$$L_r^{(1)} = 2\pi \int_0^{\frac{\pi}{2}} f_r(\cos\,\theta_i, \cos\,\theta_r) L_i \cos\,\theta_i\, \sin\,\theta_i \mathrm{d}\theta_i. \quad (7)$$

Following the method of Wolff [19] a part of this reflected diffuse flux escapes the medium through the surface and a part is reflected to interact with the scattering medium once again, and so on. This is illustrated in Fig. 3(c). The radiance of the j'th order reflection is found as in Eq. (7), except that the incoming radiance is now the part of $(j-1)$'th order reflected back into the bulk at the surface, leading to

$$L_r^{(j)} = 2\pi \int_0^{\frac{\pi}{2}} f_r(\cos\,\theta_i, \cos\,\theta_r) \times R(\theta_i) L_r^{(j-1)} \cos\,\theta_i\, \sin\,\theta_i \mathrm{d}\theta_i. \quad (8)$$

Note that θ_i of the j'th order equals θ_r of the $(j-1)$'th order. By summing up all contributions that escape the medium, the expression for the reflected radiance that will reach the observer becomes

$$L_r' = R'(\theta_r') L_i' + \sum_{j=1}^{\infty} [1 - R(\theta_r)] \frac{L_r^{(j)}}{n^2}, \quad (9)$$

where the first term represents the specular reflection at the surface and the second term is the sum of the diffuse contributions from the bulk.

4. Results

In order to extract the wavelength-dependent ρ for each of the colorants, the reflectance of the colored samples with planar surfaces was measured at 8 deg for diffuse incoming light. The single scattering albedo was determined for each wavelength by use of the theoretical model setting $\alpha = 1$. With the values of the single scattering albedos it is possible, by use of Eq. (9), to determine the change in reflected spectra with different values for the reduction in surface reflection. In Fig. 4 are the spectra of each of the colored flat samples shown along with two calculated spectra, of which the reflectance is reduced by a factor 2 ($\alpha = 0.5$) and completely removed ($\alpha = 0$). It is seen that the effect of this reduction in surface reflectance is a lowering of the reflectance for wavelengths that have low reflectance in the first place. For example, the reflectance of wavelengths shorter than 570 nm for the red sample is lowered significantly and the intensity ratio between short and long wavelengths is shifted. For the short wavelengths, basically all reflected light is due to the surface reflection as it is absorbed by the pigment. Therefore, the amount of reflected light of these wavelengths drops significantly, when lowering α. In general, for chromatic colors it is the significant spectral variations that lead to the color. An increase in the ratio between the high and low reflectance regions of a spectrum will make the spectral variations even more significant and therefore make the color appear more pure or clear corresponding to an increase in chroma.

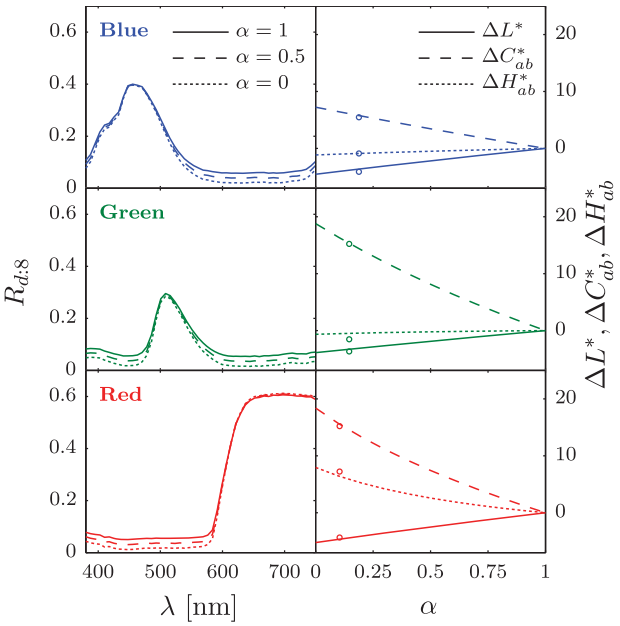

Fig. 4. Based on measured reflectance spectra are the changes in these spectra due to modifications in the surface reflectance calculated based on the proposed theoretical model. The components of the color changes for the three colors due to the lowering of α are shown. The circles mark the experimentally measured color changes plotted at the α with the best fit.

The color difference between the samples with and without ARS is evaluated based on the CIELAB 1976 color space using the cylindrical coordinates, L^*, C^*_{ab}, and h_{ab} [15]. The subscripts indicate that the quantities are calculated from the rectangular coordinates a^* and b^*. L^* is the lightness of the color and corresponds to the vertical axis in the coordinate system. The chroma is C^*_{ab} corresponding to the distance to the center axis. The hue angle, h_{ab}, is the angle coordinate. The change in hue, ΔH^*_{ab}, is calculated from the change in hue angle Δh and the chroma values of the two colors in question. The method for calculating all color values can be found elsewhere [15]. For all calculations of color values a standard illuminant D65 and the CIE 1964 10° observer have been used. A color difference in, e.g., ΔC^*_{ab} of approximately 2.3 corresponds to a just noticeable difference; however, this varies across the color space which is not visually uniform [20]. The color change between the planar surface and the surfaces with different α values has been calculated for each of the three pigments. The right column of Fig. 4 shows the results and in Table 1 are the color changes for some specific values of α listed. For all three pigments the major component of the color change is an increase in the chroma value. This means that the position in the color space is moving away from the achromatic center axis and the color becomes more clear. All colors also show a slight decrease in lightness due to the lowering of the total

Table 1. Simulated Color Changes Compared to the Color of a Flat Surface for Four Specific Values of α[a]

Sample		$\alpha = 0$	$\alpha = 0.25$	$\alpha = 0.5$	$\alpha = 0.75$
Blue	ΔL^*	−4.5	−3.3	−2.2	−1.1
	ΔC^*_{ab}	7.2	5.3	3.4	1.7
	ΔH^*_{ab}	−1.1	−0.80	−0.50	−0.23
Green	ΔL^*	−3.9	−2.9	−1.9	−0.9
	ΔC^*_{ab}	19	13	8.1	3.8
	ΔH^*_{ab}	−0.65	−0.39	−0.21	−0.089
Red	ΔL^*	−5.2	−3.8	−2.5	−1.2
	ΔC^*_{ab}	18	12	7.4	3.5
	ΔH^*_{ab}	8.0	4.7	2.6	1.1

[a]The tabulated values are from the results of Fig. 4.

reflectance. For the red pigment a significant change in hue is also seen.

The reflectance spectra of ABS samples with ARS in the surfaces were experimentally measured and are compared to those of the samples with planar surfaces in Fig. 5. As for the theoretically calculated results the reflectance drops for wavelengths with initial low reflectance. The calculated color coordinates of the measured colors are listed in Table 2 and the color differences between the flat and textured surfaces are listed in Table 3. Again it is found that the chroma increases for all three colors, while the other color attributes change less. This was also the case for the simple theoretical model in Fig. 4. To make a more direct comparison between the experimentally determined color changes and the model, the α values at which the experimental data fit the model best have been determined for each color using least square fits. The fitted α values are listed in Table 3 and the fits are also indicated in Fig. 4 where the experimental color changes are plotted at the found α values. Since α only is related to the surface it should be ideally the same for all three colors. It is seen that determined α values are between 0.1 and 0.2, implying a reduction of the reflectance at the surface to a level of 10%–20% of the original value.

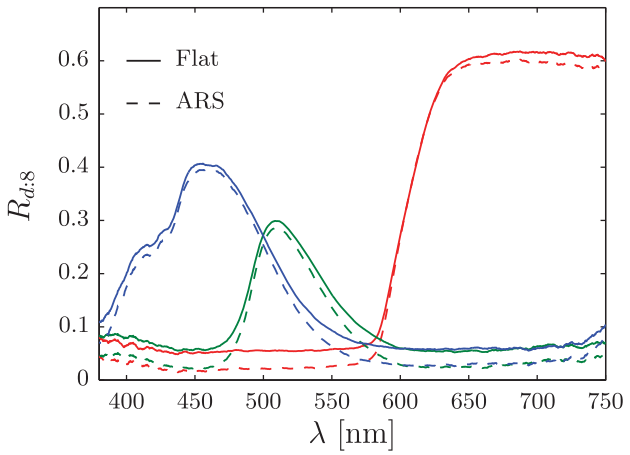

Fig. 5. Measured diffuse-direct reflectances for the three colors blue, green, and red for the case of planar surfaces (full lines) and surfaces with ARS (dashed lines). The corresponding color changes are given in Table 3.

Table 2. Color Coordinates Calculated from Experimentally Measured Reflectance Spectra (Fig. 5) for Samples with Flat Surfaces and with ARS

Sample	L^*	C^*_{ab}	h_{ab} [deg]
Blue flat	43.5	39.3	261
Blue w. ARS	39.3	44.7	259
Green flat	45.6	48.3	154
Green w. ARS	41.9	63.5	152
Red flat	42.2	51.9	29
Red w. ARS	37.8	67.1	36

Table 3. Experimentally Measured Changes in Cylindrical Color Coordinates, When Going from Flat Samples to Samples with ARS

Sample	ΔL^*	ΔC^*_{ab}	ΔH^*_{ab}	α_{fit}
Blue	−4.1	5.5	0.89	0.19
Green	−3.7	15	−1.5	0.15
Red	−4.4	15	7.2	0.10

This is somewhat lower than what is expected from previous investigations [14]. The discrepancy may be due to the simplifying assumptions of the model, such as the no scattering assumption and the assumption of α being independent on angle and wavelength.

The color changes described here are illustrated in Fig. 6, where samples of each of the three colors have been imprinted with a silicon master stamp, with ARS covering only half of the wafer. This leaves a polymer sample with the antireflective effect only being present on the right-hand side. The pictures are taken under diffuse lighting conditions.

In this paper, we have used diffuse light in the treatment of the surface. The change in color will not be the same if the samples were seen under strong point-like light sources. In this case it would depend on whether a specular reflection of one of the light sources is seen by the observer or not. In the case of a specular reflection being seen by the observer, the color difference between the flat and structured sample would be even more significant than observed with diffuse light. If no specular component was seen, there would be almost no color difference.

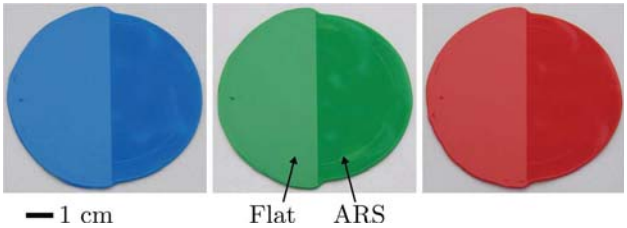

Fig. 6. Blue, green, and red ABS samples imprinted with a silicon stamp where half of the stamp was flat and the other half was covered with ARS. The left parts of the samples are flat and the right parts are with ARS.

5. Conclusion

It is found that by structural modification of the surface of a pigmented polymer it is possible to reduce the reflectance of the surface. This reduction in reflectance leads to a change in the reflected spectrum, which leads to a change in color appearance. For diffuse illumination it is found both theoretically and experimentally that the major part of the color change is an enhancement in chroma, which makes the color appear more clear and pure.

The authors acknowledge Claus H. Nielsen, DTU Danchip, for assistance with injection molding of substrates for embossing. The work was supported by the NanoPlast project funded by the Danish National Advanced Technology Foundation (File No. 007-2010-2).

References

1. C. G. Bernhard, "Structural and functional adaptation in a visual system," Endeavour **26**, 79–84 (1967).
2. P. B. Clapham and M. C. Hutley, "Reduction of lens reflexion by the moth eye principle," Nature **244**, 281–282 (1973).
3. S. Wilson and M. Hutley, "The optical properties of "moth eye" antireflection surfaces," Opt. Acta **29**, 993–1009 (1982).
4. H. Jung and K.-H. Jeong, "Monolithic polymer microlens arrays with antireflective nanostructures," Appl. Phys. Lett. **101**, 203102 (2012).
5. P. Lalanne and G. M. Morris, "Antireflection behavior of silicon subwavelength periodic structures for visible light," Nanotechnology **8**, 53–56 (1997).
6. Y. Kanamori, M. Sasaki, and K. Hane, "Broadband antireflection gratings fabricated upon silicon substrates," Opt. Lett. **24**, 1422–1424 (1999).
7. C.-H. Sun, P. Jiang, and B. Jiang, "Broadband moth-eye antireflection coatings on silicon," Appl. Phys. Lett. **92**, 061112 (2008).
8. C.-H. Sun, B. J. Ho, B. Jiang, and P. Jiang, "Biomimetic subwavelength antireflective gratings on GaAs," Opt. Lett. **33**, 2224–2226 (2008).
9. J. Tommila, V. Polojärvi, A. Aho, A. Tukiainen, J. Viheriälä, J. Salmi, A. Schramm, J. Kontio, A. Turtiainen, T. Niemi, and M. Guina, "Nanostructured broadband antireflection coatings on AlInP fabricated by nanoimprint lithography," Sol. Energy Mater. Sol. Cells **94**, 1845–1848 (2010).
10. C.-J. Yang, C.-L. Lin, C.-C. Wu, Y.-H. Yeh, C.-C. Cheng, Y.-H. Kuo, and T.-H. Chen, "High-contrast top-emitting organic light-emitting devices for active-matrix displays," Appl. Phys. Lett. **87**, 143507 (2005).
11. R. Singh, K. N. Narayanan Unni, A. Solanki, and Deepak, "Improving the contrast ratio of OLED displays: an analysis of various techniques," Opt. Mater. **34**, 716–723 (2012).
12. H.-R. Lee, D. Jae Kim, and K.-H. Lee, "Anti-reflective coating for the deep coloring of pet fabrics using an atmospheric pressure plasma technique," Surf. Coat. Technol. **142–144**, 468–473 (2001).
13. H. Becker and U. Heim, "Hot embossing as a method for the fabrication of polymer high aspect ratio structures," Sens. Actuators A **83**, 130–135 (2000).
14. A. B. Christiansen, J. Clausen, N. A. Mortensen, and A. Kristensen, "Minimizing scattering from antireflective surfaces replicated from low-aspect-ratio black silicon," Appl. Phys. Lett. **101**, 131902 (2012).
15. G. A. Klein, *Industrial Color Physics* (Springer, 2010).
16. M. Elias, P. Castiglione, and G. Elias, "Influence of interface roughness on surface and bulk scattering," J. Opt. Soc. Am. A **27**, 1265–1273 (2010).
17. S. Chandrasekhar, *Radiative Transfer* (Dover, 1960).
18. F. E. Nicodemus, J. C. Richmond, J. J. Hsia, I. W. Ginsberg, and T. Limperis, "Geometrical considerations and nomenclature for reflectance," Natl. Bur. Stand. (U.S.), Monogr. **160**, 1–52 (1977).
19. L. B. Wolff, "Diffuse-reflectance model for smooth dielectric surfaces," J. Opt. Soc. Am. A **11**, 2956–2968 (1994).
20. G. Sharma, *Digital Color Imaging Handbook* (CRC Press, 2002).

Paper D

NANO LETTERS

Letter

pubs.acs.org/NanoLett

Plasmonic Metasurfaces for Coloration of Plastic Consumer Products

Jeppe S. Clausen,[†] Emil Højlund-Nielsen,[‡] Alexander B. Christiansen,[‡] Sadegh Yazdi,[§] Meir Grajower,[∥] Hesham Taha,[⊥] Uriel Levy,[∥] Anders Kristensen,*[,‡] and N. Asger Mortensen*[,†]

[†]Department of Photonics Engineering, [‡]Department of Micro and Nanotechnology, and [§]Center for Electron Nanoscopy, Technical University of Denmark, DK-2800 Kongens Lyngby, Denmark

[∥]Department of Applied Physics, The Benin School of Engineering and Computer Science, The Center for Nanoscience and Nanotechnology, The Hebrew University of Jerusalem, Jerusalem 91904, Israel

[⊥]Nanonics Imaging Ltd., Hartum 19, Har Hotzvim, Jerusalem 97775, Israel

S *Supporting Information*

ABSTRACT: We present reflective plasmonic colors based on the concept of localized surface plasmon resonances (LSPR) for plastic consumer products. In particular, we bridge the widely existing technological gap between clean-room fabricated plasmonic metasurfaces and the practical call for large-area structurally colored plastic surfaces robust to daily life handling. We utilize the hybridization between LSPR modes in aluminum nanodisks and nanoholes to design and fabricate bright angle-insensitive colors that may be tuned across the entire visible spectrum.

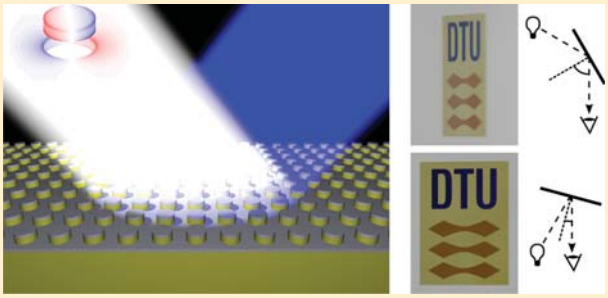

KEYWORDS: *Plasmonics, structural color, hybridization, nanofabrication*

Pigment-based coloring of polymers is used in the fabrication of almost any type of plastic-based consumer product, either as base color in the bulk polymer or in surface-decoration inks. The mixing of many colorants in a single product is both costly and limits the possibilities for recycling as separation of the different colorants is impossible. Structural colors offer an attractive approach to reduce the number of needed materials in a given product and it provides new perspectives for recycling and sustainability.

Various strategies may be taken toward structural colors. Inspired by nature[1,2] pure dielectric structures based on photonic crystals in one or more dimensions have been demonstrated[3,4] and recently the use of ultrathin high-loss dielectrics on top of metal have led to bright colors.[5] The works on plasmonic colors have widely emphasized filters working in transmission[6−9] while only more recently plasmonic cavity resonances and LSPR concepts have been used for filters working in reflection.[10−15] The resonant behavior of the plasmonic systems often leads to large field enhancements that are advantageous in other applications such as surface-enhanced Raman spectroscopy.[16−20]

The structural color effects must possess at least three important properties to become relevant for use in consumer products. First, the color effect should be insensitive to varying viewing angles. Furthermore, it should be robust for everyday use. Finally, it should be up-scalable and economically affordable. We demonstrate a plasmonic metasurface that possesses all these qualities. Recently plasmonic resonators consisting of silver and gold have been used for color printing with resolution beyond the diffraction limit.[10,15] We use insight from hybridization theory[21] to build upon the work of Kumar[10] toward coloration of volume-produced plastic components, addressing the three criteria mentioned above: angle independence, wear resistance, and up-scalability.

Thin metal nanodisks can be tuned in size to modulate the optical response through the visible and near-infrared spectral range.[22] In our work, the colors are based on metal disks on top of dielectric pillars and hovering above a holey metal film, see Figure 1a−c. Rather than employing the common choice of silver or gold, we explore aluminum, which is a widely employed material in industrial processes while so far mainly being conceptually studied as a new plasmonic material.[23−27] Silver and gold are commonly preferred over aluminum for plasmonic applications due to lower ohmic losses. However, we find an advantage of the specific interband absorption properties of aluminum, which gives a pronounced difference in the dispersion of the surface plasmon polaritons (SPPs) supported by the metal−dielectric interfaces of the continuous (holey) film. As demonstrated later, the excitation of SPPs constitutes the main limitation on the angle independence of the observed color and here SPPs supported by aluminum have an advantage over SPPs on silver surfaces due to their k-space existence closer to the "light line" in the frequency range of the visible spectrum. In addition to this, gold has the disadvantage of having an interband transition threshold centered in the

Received: April 23, 2014
Revised: June 23, 2014

   dx.doi.org/10.1021/nl5014986 | *Nano Lett.* XXXX, XXX, XXX−XXX

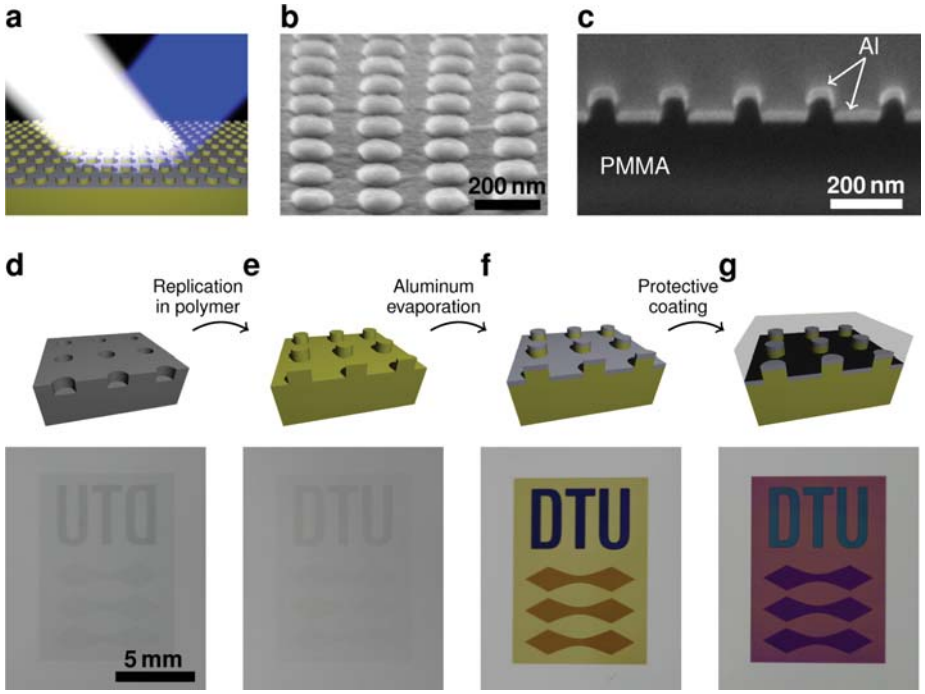

Figure 1. Basic concept of fabrication and working mechanism. (a) The reflected light is modified due to absorption resonances in the plasmonic nanostructure leading to colored reflections upon white-light illumination. The reflected color can be varied by tuning the surface geometry. (b) A SEM image of fabricated disks elevated above the holey plane seen from 15° above the horizon. (c) Cross-sectional SEM image obtained using focused ion-beam for sample preparation. (d) A master mold comprising nanohole arrays is used for the fabrication of polymer pillar arrays using hot embossing or injection molding. The photography shows a macroscopic sample with three different hole sizes leading to three different colors in the final sample. (e) A polymer pillar array replication of the master mold. (f) Aluminum is evaporated on top, creating the disk-hole structure thereby revealing colors due to the underlying polymer topography. (g) The structure is coated with a transparent material to protect from greasy contamination, fingerprints, and scratches. The resonance redshift introduced by the coating leads to clearly altered colors.

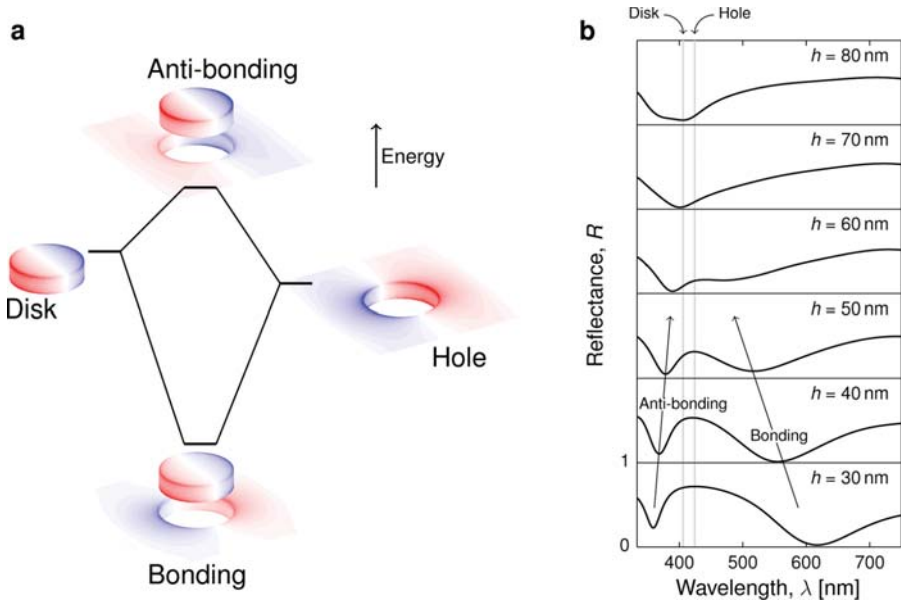

Figure 2. Plasmon hybridization due to disk-hole coupling. (a) Energy diagram illustrating the hybridization of the coupled plasmonic modes of the disks and holes of the structure into a low energy mode (bonding) and a high energy mode (antibonding). The simulated charge distributions of the pure disk and hole arrays show the dipolar nature of their resonances. For the full structure, the symmetric and antisymmetric coupling leads to an energy splitting. The shown structure is for D = 80 nm, Λ = 200 nm, h = 50 nm, and t = 20 nm embedded in material of refractive index of 1.5. It shows the symmetric and antisymmetric coupling between the disks and holes. (b) Reflectance spectra for same parameters as panel a but for varying pillar height, h. The two modes are seen as dips in the spectra. The coupling and thereby the energy splitting decreases with increasing pillar height leading to a shift of the resonances toward the natural resonances of the disk and hole arrays.

dx.doi.org/10.1021/nl5014986 | *Nano Lett.* XXXX, XXX, XXX−XXX

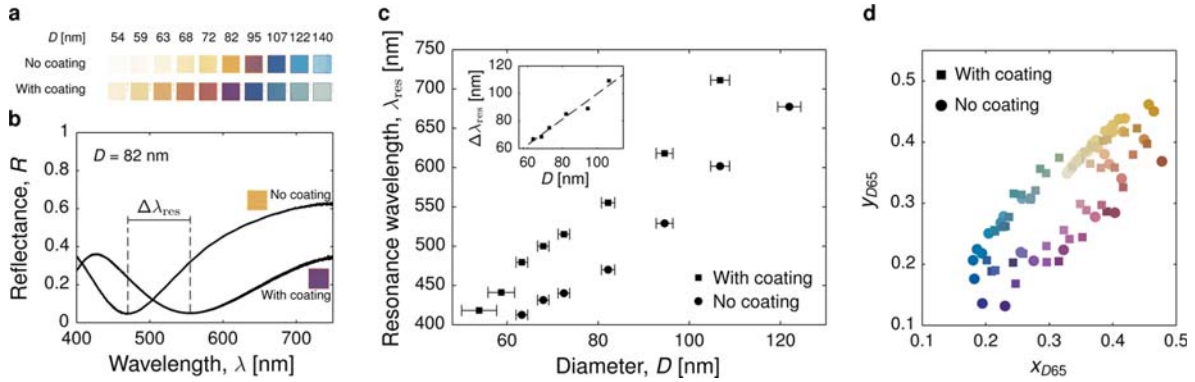

Figure 3. Diameter-dependent resonance and colors. (a) Images in bright-field microscopes of 0.8 × 0.8 mm^2 squares with period Λ = 200 nm and varying diameter. The coating-induced redshift is evident. (b) Reflectance spectra of structure with D = 82 ± 2 nm with and without coating indicating the change in resonance wavelength $\Delta\lambda_{res}$ due to the coating. (c) Resonance position as a function of disk diameter for Λ = 200 nm. The shift in resonance due to the coating is seen to be approximately linear with diameter. (d) CIE 1931 chromaticity coordinates of the fabricated samples for both the coated and the uncoated case (spectra in Supporting Information Figure S2). The color of each spot indicates the color of the corresponding sample.

visible spectrum whereas aluminum only facilitates interband transitions in a narrow wavelength range outside the visible spectrum.[28] For large-volume use of plasmonic metasurfaces in, for example, plastic consumables, the abundance and cost of aluminum makes it attractive. The integration in mass-fabrication systems is also eased significantly compared to, for example, silver where the need for an adhesion layer (such as titanium or chromium) and a capping layer (such as gold) to protect against sulphidation, complicates the metal deposition.

The fabrication scheme is presented in Figure 1d–g. A master mold is fabricated in silicon using electron-beam lithography (EBL) and dry etching. A fast single spot writing technique was employed,[29,30] which allows writing speeds higher than 1 cm^2/hour in the production of the silicon masters. This leads to a wider size distribution of the nanostructures than for conventional EBL resulting in inhomogeneous broadening of the resonances. This is however acceptable and compensated by the very large decrease in writing time. The finalized master consists of periodic hole arrays with period Λ, hole diameter D, and hole depth h. The master is a negative of the desired polymer surface, a periodic pillar array, which is fabricated in a hot embossing step. After replication, the desired pattern is practically invisible as the polymer–air index contrast is too low to significantly alter the surface reflectance of the nanostructured polymer surface. However, bright and angle-independent colors emerge when a thin aluminum film of thickness t is deposited on top of the textured polymer surface, see Figure 1f. The metal deposition must be directional in order to facilitate the creation of isolated metal disks. For situations with very large sample size and small evaporation source, this may lead to undesired side-wall deposition thereby defining the maximum sample size. When using roll-to-roll systems, this issue may be avoided due to the continuous deposition of metal.

Finally, a protective coating is deposited on top with a thickness significantly larger than the coherence length of broadband white light in order to avoid Fabry–Pérot interference affecting the color experience. The coating causes an increase in the effective refractive index surrounding the disk-hole nanostructure, which leads to a redshift of the resonances in the system and a corresponding color change as seen in the last step of Figure 1. The top coating is necessary to protect the structure from mechanical damage, fingerprints, greasy residue, and so forth. In this work, a UV-curable organic–inorganic hybrid material (Ormocomp, Micro resist technology GmbH) with good scratch resistance[31] has been used, but many different types of coatings are already used in large scale production to protect evaporated metal films of various kinds.

The colors of the structure are due to resonant absorption in the aluminum nanostructures. Both the disks and holes possess dipolar resonances on their own, which leads to increased absorption at specific wavelengths. When brought very close together the two modes hybridize into two new modes, a "bonding" mode that is characterized by a lower resonance frequency (longer wavelength) and an "antibonding" mode with higher resonance frequency.[21] Simulated surface charge distributions of the relevant modes are shown in Figure 2a for the specific structure of period Λ = 200 nm, diameter D = 80 nm, aluminum thickness t = 20 nm, and pillar height h = 50 nm. The low-energy mode is characterized by the charge oscillations in the disk and the hole being out-of-phase whereas for the high energy mode the charge oscillations are in phase. The effect on the reflectance spectrum is illustrated in Figure 2b where each of the two hybrid modes appear as significant dips in the reflectance spectra. It is seen how the energy splitting decreases, when the pillar height, h, increases thereby decreasing the coupling between the resonators. It is also seen that the strength of the "bonding" mode is highly dependent on low pillars (large coupling) and above h = 70 nm the hybridization is not seen in the reflectance spectra. For even higher pillars,[32] the behavior of the system moves toward a Fabry–Pérot-like regime where the disk array and the hole array each acts as separate mirrors with resonant reflection coefficients. It is found that when using aluminum as the plasmonic material a strong resonance of the hybrid "bonding" mode is key to the creation of tunable colors. This is seen from simulations (Supporting Information, Figure S1), which demonstrate how it is possible with strong coupling (low pillars) to obtain resonances across the entire visible spectrum by tuning the pillar diameter, while for vague coupling (high pillars) no such tuning is possible. Because we mainly utilize the "bonding" mode resonance we will in the following just denote the wavelength of this resonance λ_{res}.

dx.doi.org/10.1021/nl5014986 | Nano Lett. XXXX, XXX, XXX–XXX

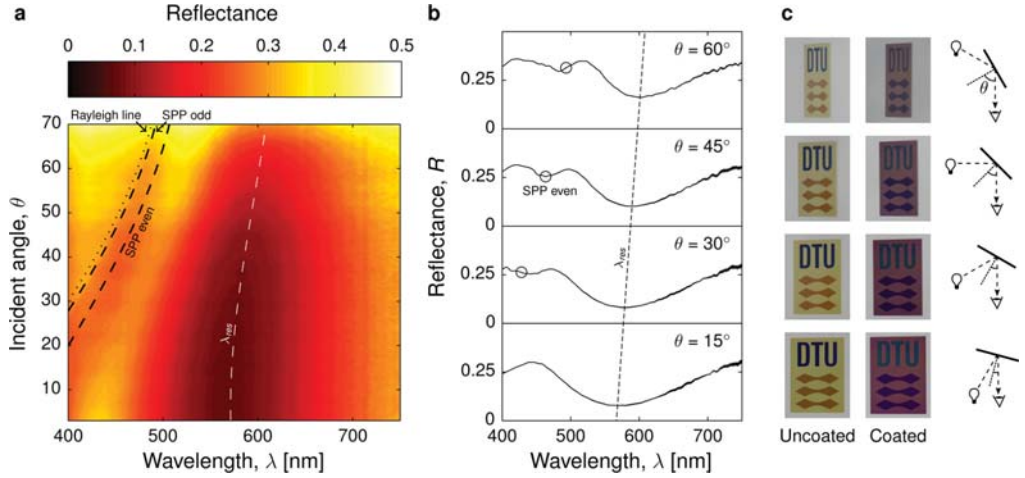

Figure 4. Angle dependence of reflected spectrum. (a) Measured angle-resolved spectra of coated sample with $\Lambda = 200$ nm and $D = 86 \pm 2$ nm. The white dashed line indicates the reflectance minimum and the black dashed lines indicate the theoretical excitation of SPPs (odd and even modes) in a 20 nm Al film embedded in material of refractive index 1.5. The dotted line indicates the appearance of new diffraction orders (Rayleigh wavelength). The resonance is seen to shift very little even at very high angles. (b) Single spectra at four different angles of the same sample as in panel a. (c) Pictures of macroscopic patterns viewed at four different angles. The colors are seen to be almost identical even for very large angles. The gray background is the unstructured surface of the samples.

While securing the existence of the important hybrid "bonding" mode by fabricating very low pillars one must keep in mind that it is of great importance that the disks are separated from the lower lying film to avoid short circuiting of the capacitively coupled disk and hole planes. By preparing a cross section sample, using focused ion beam (FIB), we can confirm that in majority of cases the disk and the lower lying film are separated, see Figure 1c.

In the fabrication of the polymer pillars a certain rounding at the pillar end-face should be expected, compared to the perfect cylindrical shape used in simulations. The rounding is seen in Figure 1c. This effectively reduces the vertical gap between the disk and hole, which is why it is necessary to fabricate the pillars slightly higher than predicted by simulations for achieving comparable coupling. Fabricated pillars were $h = 56 \pm 4$ nm high, measured by atomic force microscope, and the aluminum thickness was $t = 20$ nm, measured by quartz crystal microbalance during deposition.

The fixed pillar height and metal thickness leave the diameter and period as design parameters. In this work, diameters between 40−160 nm and periods ranging from 160 to 240 nm have been studied experimentally. Figure 3a shows color photos of $\Lambda = 200$ nm samples with and without the presence of a protective coating. Colors across the entire visible spectrum are produced at will by varying the disk diameter at fixed period. The measured reflectance spectra of disks with diameter 82 ± 2 nm are shown as example in Figure 3b. The coating induces a redshift $\Delta\lambda_{res}$ of the resonance due to increase in effective refractive index around the nanostructure. One should notice the high off-resonant reflectance in contrast to the low reflectance at resonance, which leads to very bright colors. For both the coated and uncoated case, the resonance position increases almost linearly with diameter. Specifically for the coated case, the resonance may be tuned on the wavelength interval 400−700 nm by tuning the diameter on the interval 50−110 nm. The coating-induced redshift is also found to increase linearly with diameter. Reflectance spectra for the other periods and diameters are provided in the Supporting Information (Figure S2). The effect of the period on the resonance position is less pronounced as it only influences the mutual coupling of neighboring resonators. The nearest-neighbor coupling does however influence how much a change in diameter alters the resonance position (the slope of Figure 3c). For a coated sample with $\Lambda = 160$ nm, a 1 nm increase in diameter leads to an approximate redshift of 7 nm whereas for $\Lambda = 240$ nm it only leads to an approximate redshift of 4 nm (see Supporting Information Figure S3). Although the period does not influence the resonance position significantly, it plays an important role in relation to the angular dependence.

The range of colors that may be produced using the proposed method is illustrated in Figure 3d where all experimentally measured spectra (see Supporting Information Figure S2) have been converted to CIE1931 chromaticity coordinates, thereby illustrating the color gamut of the method. It is noteworthy that there are points all around the achromatic point, illustrating the large degree of color tuning ability. There are however some colors that are difficult to produce when the effect is based on a spectral dip originating from resonant absorption. Very chromatic red and green are examples of such colors.

The angle independence of the reflective colors was investigated on larger samples (4×6 mm^2). The specular reflectance was measured with unpolarized light for incident angles at 3−70°, see Figure 4. Data are shown for a coated sample with $\Lambda = 200$ nm and $D = 86 \pm 2$ nm. In the surface plot of Figure 4a, the broad dip in the reflectance is observed around a vacuum wavelength of 580 nm and is slightly red shifted by approximately 20 nm for increasing angle of incidence. This is the diameter-dependent plasmonic absorption resonance described previously. Individual reflectance spectra for four different angles are shown in Figure 4b, and the photographs in Figure 4c illustrate the angle independence of the color appearance. The changes of the CIE1931 chromaticity coordinates due to changing angles have been calculated based on the angle-resolved spectra and are presented in the Supporting Information (Figure S4). As seen in panels a and b, the strength of the resonance dip decreases with increasing angle of incidence. This is due to a decreasing component of

dx.doi.org/10.1021/nl5014986 | Nano Lett. XXXX, XXX, XXX−XXX

the electric field of the TM mode parallel to the dipole axis under consideration. A weak angle-dependent feature is observed at vacuum wavelength below 500 nm, which is caused by grating-assisted excitation of SPPs at the metal−dielectric interfaces. The dashed black lines indicate the calculated dispersion of the odd and even modes for a 20 nm aluminum film embedded in a material of refractive index 1.5. The Rayleigh line, where the first diffraction order appears, is plotted as a dotted line. Of the three anomalies, the even (high loss) SPP mode lies in the center of the angle-dependent dip, and in Figure 4b the circles indicate the position of this mode. It corresponds well with the dips in the measured reflectance spectra and the feature is attributed to this mode. The positions of the SPP anomalies depend on the grating-induced change in momentum parallel to the surface and are therefore highly dependent on the structure period. A longer grating period, Λ, will result in the anomalies appearing at lower angles, implying a higher degree of angle dependence, whereas a shorter period will lead to less impact on the spectra (see Figure S5 in Supporting Information). This implies a trade-off between obtaining low angular dependence and fabrication limitations due to dense structures with small grating period. Properties of the SPP modes have been investigated using near-field scanning optical microscopy (NSOM). The data are presented in the Supporting Information (Figure S6).

While the position of the Rayleigh line only depends on the grating period and the refractive index of the materials surrounding the metal, the dispersion relation for the SPPs also has a strong dependence on the dielectric constant of the metal. Hence, the position of the angle-dependent SPP modes (relative to the localized mode) makes the feasibility of angle-independent plasmonic structural colors strongly material dependent. As an example, we compare aluminum and silver in the Supporting Information (Figure S5). For aluminum, the SPP modes lie very close to the Rayleigh line and may therefore be moved out of the visible spectrum, even for high incident angles by using small periods. On the other hand, for silver films SPPs are excited at normal incidence, even for very short periods whereby the SPP modes spectrally intersect with the localized modes. This leads to phenomena such as avoided crossing between the two intersecting modes resulting in significant angle-dependent behavior of the color-producing mode. Because this is a property originating from the electronic structure of the chosen metal, this promotes aluminum over silver for use in this application.

Because of the subwavelength periodic nature of the structure, the color effect is only seen in the specular reflection. This limits the applicability under certain lighting conditions. For diffuse lighting conditions, an observer will experience uniform color, while illumination by very directional light sources will lead to a more varying color experience. To overcome this problem, one may introduce scattering in the protective film either by particles, surface roughness or by using semicrystalline (translucent) polymers as coating material. This will allow for diffuse reflectance from the surface similar to that of inks.

In conclusion, we demonstrate angle-insensitive scratch-resistant structural colors, where aluminum is used as a cheap and abundant plasmonic material. We utilize a hybrid disk-hole plasmonic mode, which provides angle-independent resonances tunable across the entire visible spectrum. Expensive nano-lithography should only be carried out once due to the subsequent replication-based fabrication and the structure geometry allows for a fast EBL technique to define macroscopic wafer-sized patterns. The functional structures are covered by a protective dielectric coating, causing a redshift of the plasmon resonance. The method holds potential for large scale implementation of structural colors in plastic products for daily use.

■ ASSOCIATED CONTENT

Supporting Information

Details about fabrication process, optical characterization, and simulations as well as supplementary figures (Figures S1−S6). This material is available free of charge via the Internet at http://pubs.acs.org.

■ AUTHOR INFORMATION

Corresponding Authors

*E-mail: (A.K.) anders.kristensen@nanotech.dtu.dk.
*E-mail: (N.A.M.) asger@mailaps.org.

Notes

The authors declare no competing financial interest.

■ ACKNOWLEDGMENTS

The authors thank Cameron Smith and Christoph Vannahme for advice on microscope measurements and Thomas Christensen for fruitful discussions on the data interpretation. The work was supported by the Danish National Advanced Technology Foundation (Contract No.: 007-2010-2) via the NanoPlast project and by the European Commission via the FP7MMP Integrated project PLAST4FUTURE (NMP2-SE-2012-314345). The work was also supported by the Danish Agency for Science, Technology and Innovation (International Network Programme, Israel-Danish international collaboration, Framework Grant 1370-00124A).

■ REFERENCES

(1) Vukusic, P.; Sambles, J. R. *Nature* **2003**, *424*, 852−855.
(2) Kinoshita, S.; Yoshioka, S.; Miyazaki, J. *Rep. Prog. Phys.* **2008**, *71*, 076401.
(3) Saito, A.; Miyamura, Y.; Nakajima, M.; Ishikawa, Y.; Sogo, K.; Kuwahara, Y.; Hirai, Y. *J. Vac. Sci. Technol. B* **2006**, *24*, 3248−3251.
(4) Chung, K.; Yu, S.; Heo, C.-J.; Shim, J. W.; Yang, S.-M.; Han, M. G.; Lee, H.-S.; Jin, Y.; Lee, S. Y.; Park, N.; Shin, J. H. *Adv. Mater.* **2012**, *24*, 2375−2379.
(5) Kats, M. A.; Blanchard, R.; Genevet, P.; Capasso, F. *Nat. Mater.* **2013**, *12*, 20−24.
(6) Ebbesen, T. W.; Lezec, H. J.; Ghaemi, H. F.; Thio, T.; Wolff, P. A. *Nature* **1998**, *391*, 667−669.
(7) Lee, H.-S.; Yoon, Y.-T.; shin Lee, S.; Kim, S.-H.; Lee, K.-D. *Opt. Express* **2007**, *15*, 15457−15463.
(8) Xu, T.; Wu, Y.-K.; Luo, X.; Guo, L. J. *Nat. Commun.* **2010**, *1*, 59.
(9) Inoue, D.; Miura, A.; Nomura, T.; Fujikawa, H.; Sato, K.; Ikeda, N.; Tsuya, D.; Sugimoto, Y.; Koide, Y. *Appl. Phys. Lett.* **2011**, *98*, 093113.
(10) Kumar, K.; Duan, H.; Hegde, R. S.; Koh, S. C. W.; Wei, J. N.; Yang, J. K. W. *Nat. Nanotechnol.* **2012**, *7*, 557−561.
(11) Lochbihler, H. *Opt. Lett.* **2013**, *38*, 1398−1400.
(12) Wu, Y.-K. R.; Hollowell, A. E.; Zhang, C.; Guo, L. J. *Sci. Rep.* **2013**, *3*, 1194.
(13) Si, G.; Zhao, Y.; Lv, J.; Lu, M.; Wang, F.; Liu, H.; Xiang, N.; Huang, T. J.; Danner, A. J.; Teng, J.; Liu, Y. J. *Nanoscale* **2013**, *5*, 6243−6248.
(14) Yan, M.; Dai, J.; Qiu, M. *J. Opt.* **2014**, *16*, 025002.
(15) Roberts, A. S.; Pors, A.; Albrektsen, O.; Bozhevolnyi, S. I. *Nano Lett.* **2014**, *14*, 783−787.

(16) Chu, Y.; Banaee, M. G.; Crozier, K. B. *ACS Nano* **2010**, *4*, 2804−2810.
(17) Caldwell, J. D.; Glembocki, O.; Bezares, F. J.; Bassim, N. D.; Rendell, R. W.; Feygelson, M.; Ukaegbu, M.; Kasica, R.; Shirey, L.; Hosten, C.; Al, C. E. T. *ACS Nano* **2011**, *5*, 4046−4055.
(18) Li, W.; Hu, J.; Chou, S. *Opt. Express* **2011**, *19*, 21098−21108.
(19) Li, W.; Ding, F.; Hu, J.; Chou, S. *Opt. Express* **2011**, *19*, 863−870.
(20) Cheng, C.-W.; Abbas, M. N.; Chiu, C.-W.; Lai, K.-T.; Shih, M.-H.; Chang, Y.-C. *Opt. Express* **2012**, *20*, 10376−10381.
(21) Prodan, E.; Radloff, C.; Halas, N.; Nordlander, P. *Science* **2003**, *302*, 419−422.
(22) Manjavacas, A.; García de Abajo, F. J. *Nat. Commun.* **2014**, *5*, 3548.
(23) Chen, Q.; Cumming, D. R. S. *Opt. Express* **2010**, *18*, 14056−14062.
(24) Langhammer, C.; Schwind, M.; Kasemo, B.; Zorić, I. *Nano Lett.* **2008**, *8*, 1461−1471.
(25) Chan, G. H.; Zhao, J.; Schatz, G. C.; Van Duyne, R. P. *J. Phys. Chem. C* **2008**, *112*, 13958−13963.
(26) Knight, M. W.; Liu, L.; Wang, Y.; Brown, L.; Mukherjee, S.; King, N. S.; Everitt, H. O.; Nordlander, P.; Halas, N. J. *Nano Lett.* **2012**, *12*, 6000−6004.
(27) Knight, M. W.; King, N. S.; Liu, L.; Everitt, H. O.; Nordlander, P.; Halas, N. J. *ACS Nano* **2014**, *8*, 834−840.
(28) Zorić, I.; Zäch, M.; Kasemo, B.; Langhammer, C. *ACS Nano* **2011**, *5*, 2535−2546.
(29) Gadegaard, N.; Thoms, S.; Macintyre, D. S.; Mcghee, K.; Gallagher, J.; Casey, B.; Wilkinson, C. D. W. *Microelectron. Eng.* **2003**, *68*, 162−168.
(30) Højlund-Nielsen, E.; Greibe, T.; Mortensen, N. A.; Kristensen, A. *Microelectron. Eng.* **2014**, *121*, 104−107.
(31) Sanchez, C.; Julin, B.; Belleville, P.; Popall, M. *J. Mater. Chem.* **2005**, *15*, 3559−3592.
(32) Lochbihler, H.; Ye, Y. *Opt. Lett.* **2013**, *38*, 1028−30.

Paper E

Invited Paper

Imprinted and injection-molded nano-structured optical surfaces

Alexander B. Christiansen[a], Emil Højlund-Nielsen[a], Jeppe Clausen[b], Gideon P. Caringal[a], N. Asger Mortensen[b], and Anders Kristensen[a]

[a]Department of Micro and Nanotechnology, Technical University of Denmark, Oersteds Plads, Building 345B, DK-2800 Kgs. Lyngby, Denmark;
[b]Department of Photonics Engineering, Technical University of Denmark, Oersteds Plads, Building 343, DK-2800 Kgs. Lyngby, Denmark

ABSTRACT

Inspired by nature, nano-textured surfaces have attracted much attention as a method to realize optical surface functionality. The moth-eye antireflective structure and the structural colors of Morpho butterflies are well-known examples used for inspiration for such biomimetic research. In this paper, nanostructured polymer surfaces suitable for up-scalable polymer replication methods, such as imprinting/embossing and injection-molding, are discussed. The limiting case of injection-moulding compatible designs is investigated. Anti-reflective polymer surfaces are realized by replication of Black Silicon (BSi) random nanostructure surfaces. The optical transmission at normal incidence is measured for wavelengths from 400 nm to 900 nm. For samples with optimized nanostructures, the reflectance is reduced by 50 % compared to samples with planar surfaces. The specular and diffusive reflection of light from polymer surfaces and their implication for creating structural colors is discussed. In the case of injection-moulding compatible designs, the maximum reflection of nano-scale textured surfaces cannot exceed the Fresnel reflection of a corresponding flat polymer surface, which is approx. 4 % for normal incidence. Diffraction gratings provide strong color reflection defined by the diffraction orders. However, the apperance varies strongly with viewing angles. Three different methods to address the strong angular-dependence of diffraction grating based structural color are discussed.

Keywords: Structural Color, diffraction gratings, anti-reflective coatings, polymer replication

1. INTRODUCTION

Within the past decades, nano-textured surfaces have attracted much attention as a method to realize optical surface functionality. The moth-eye antireflective structure[1] and the structural colors of Morpho butterflyes[2,3] are well-known examples. In this paper, nanostructured polymer surfaces suitable for up-scalable polymer replication methods, such as imprinting/embossing and injection-molding, are discussed. The limiting case of injection-moulding compatible designs is investigated.

This study is motiviated by the need for efficient and large scale recycling, due to an increasing world population and declining natural resources. Much of the waste generated stems from plastic products. Here the base color is given by bulk properties based on pigmentation. Added surface decoration provides additional color effects, for example logos, text decoration or line art, thereby providing cost effective color effects. However, the addition of decoration also makes recycling difficult, because the powerful pigments used for the thin decoration layers tend to pollute the base color of the bulk material in the recycling state. Here we propose functional surfaces for structural colors and other optical effects to produce decoration art, thereby enabling a direct decomposition into raw materials of the consumed product. The vision is multi-functional surfaces, where surface topography added to a material creates new functionalities, such as color, anti-reflective and self-cleaning properties for plastic parts.

The nano-texture anti-reflective surface of moth-eyes was first reported in 1967 by Bernhard,[1] who observed the tapered nano-structure by scanning electron microscopy of slices of the moth-eye lens. The broadband anti-reflective functionality was confirmed by micro-wave experiments. In 1973, Clapham realized the first artificial

Corresponding author: A.K. (anders.kristensen@nanotech.dtu.dk).

Nanostructured Thin Films VI, edited by Tom G. Mackay, Akhlesh Lakhtakia, Yi-Jun Jen, Motofumi Suzuki,
Proc. of SPIE Vol. 8818, 881803 · © 2013 SPIE · CCC code: 0277-786X/13/$18 · doi: 10.1117/12.2025133

anti-reflective moth-eye structure in the visible range by interference lithography in a thin photo resist film on a glass substrate, yielding 200 nm protuberances.[4] Already these first papers clarified the underlying physics; that the structures function as an effective gradient in refractive index of the material reducing reflections from the surface. Furthermore, it was shown by modeling that minimum reflectance can be acheived with $d/\lambda = 0.4$, where d is the height of the tapered protuberances and λ is the vacuum wavelength for glass materials. More general numerical modeling was reported by Stephens and Cody in 1977.[5] The advancement of nano-scale lithography has enabled further research; a few examples are electron beam lithography defined silicon nanocone arrays,[6] silicon and polymer surfaces by plasma etching and replication[7] and anti-reflection anti-fogging silica surfaces.[8]

Structural colors are optical phenomena, where the topography of a surface determines the reflected spectrum of light, although an unambiguous definition has not been settled yet.[9] In recent years, structural coloration has attracted considerable attention within the field of optics.[10–13] The mechanisms of structural colors are categorized into thin-film interference, multi-layer interference, diffraction grating optical effects, and photonic crystal effects.[9] In nature, structural colors are found among butterflies and beetles, such as the Morpho butterfly,[14] reflecting omnidirectional blue light due to a multilayer topography.

The structures found in nature often consist of several layers. Here the focus is on one-layer structures that comply with injection-molding, the industry standard for high volume plastic production. This only allows for simple single-material surface textures, and may not, for example, comprise closed air-filled regions inside the material.

Anti-reflective polymer surfaces are realized by replication of Black Silicon (BSi) random nanostructure surfaces. The specular and diffusive reflection of light from polymer surfaces and their implication for creating structural colors is discussed. In the case of injection-moulding compatible designs, the maximum reflection of nano-scale textured surfaces is discussed. Diffraction gratings provide strong color reflection defined by the diffraction orders. However, the apperance varies strongly with viewing angles. Three different methods to address the strong angular-dependence of diffraction grating based structural color are discussed.

2. REFLECTION FROM A POLYMER SURFACE

In this section, the specular and diffusive reflection of light from polymer surfaces and their implication for creating structural colors is discussed. The limitations imposed by the injection moulding production platform itself is considered. Injection-moulding requires that the parts are able to be separated from the molding tool without damage. Therefore, any topography must consist of one layer only of alteration without closed air-filled regions inside the material. Any structure may only consist of one layer of alteration on top of bulk. All individual structures or combinations may be periodic or semi-periodic. We will refer to these single-material structures of one layer, that have zero or positively sloped sidewalls, as injection-moulding compatible surface textures, because they in general allow for the separation in an injection-molding machine. Examples are given in Fig. 1.

The topography limitations described above generally indicate that the advanced multi-layer structures often found in nature, on butterfly scales and similar,[15] cannot be fabricated using a one-step injection molding process. These limitations have consequences for the optical performance. It has been shown by Bao[16] that the upper limit of surface reflection for all injection-molding compatible periodic structures are given by the reflectance of a plane dielectric interface, where the largest difference in refractive index occurs and thus the largest reflection of energy. The reflection of a planar dielectric interface is also known as Fresnel or specular reflection, often arising from mirror like surfaces. This limitation applies for all values of the bulk refractive index, n_2, larger than that of the surrounding air medium, n_1. The simplest possible case of reflection and transmission is given by of a lossless dielectric interface between two regions, air and material. The reflection and transmission for normal incidence is independent on polarization and can be calculated using the Fresnel coefficients:

$$R_\perp = r^2 = \left(\frac{n_1 - n_2}{n_1 + n_2}\right)^2 = \left(\frac{1 - 1.5}{1 + 1.5}\right)^2 = 0.04,$$

indicating that plastic materials only reflect 4 % of the incoming normal light. The remaining 96 % is transmitted into bulk. It is seen that, as the numerical difference between the two refractive indices becomes smaller, the

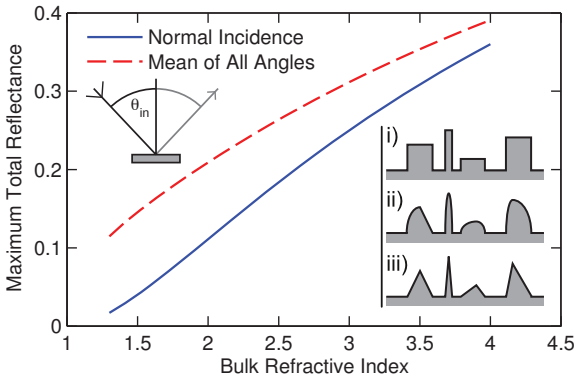

Figure 1: Maximum specular reflectance for Injection-molding compatible topograhies for unpolarized light for normal incidence (blue curve) and averaged over all incoming angles assuming a uniform intensity distribution (red curve), where examples i, ii and iii are defined with respect to an initial flat micro-scale surface.

reflection is reduced. We define the hemispherical reflection W for un-polarized light averaged over all angles: $W(n_1, n_2) = \frac{1}{\pi} \int_{\theta_{\text{in}}=-\frac{\pi}{2}}^{\frac{\pi}{2}} R(n_1, n_2, \theta_{\text{in}})\, \mathrm{d}\theta_{\text{in}}$, describing the total normalized reflection of a dielectric surface equally illuminated at all angles. In Fig. 1, the total reflection is seen as function of refractive index for normal incidence and averaged over all incoming angles (hemispherical reflection). For an air-plastic interface, with $n_2 = 1.5$, we find an accumulated reflection of 8.92 % for p-polarization and 20.2 % for s-polarization. This means, that in normal daylight, meaning uni-directional un-polarized light, we may only alter 14.6 % of the incoming light at maximum. The remaining 85.4 % of the incoming light is transmitted into bulk, where it may be absorbed or scattered. As an rule of thumb, the hemispherical reflection for common plastic materials is around 15 %. These numbers describe the fundamental limit of performance in clear plastic for any structure or design respecting the injection-molding compatibility condition. In general, higher refractive index means higher reflection.

We now consider a periodic nano-texturing of the surface, characterized by a period Λ. If the period of the texture is longer than the wavelength of the incident light, we refer to this periodic alteration as a diffraction grating. We find the grating equation [17, Eq. (1)], here written in the most general case:

$$\begin{aligned} n_1 \sin\theta_m - n_1 \sin\theta_{\text{in}} &= \frac{m\lambda}{\Lambda}, \quad (\text{reflected orders}) \\ n_2 \sin\theta_m - n_1 \sin\theta_{\text{in}} &= \frac{m\lambda}{\Lambda}, \quad (\text{transmitted orders}) \end{aligned} \tag{1}$$

where n_1 and n_2 is the refractive indices of the incident medium and the transmission medium respectively, and θ_{in} is the incident angle of the light with respect to the surface normal. This is a very general formula because Fourier series form the most fundamental solution to any linear differential equation that is subject to periodic boundary conditions. Therefore iridescence arising from diffraction gratings always takes the form of one or more ordered spectra although intensity may vary. Besides the slowly varying intensity of diffracted spectral orders described by the grating equation (1), rapid variations can also be found in certain narrow frequency bands. These abnormally high or low intensities in the diffracted light are referred to as Wood's anomalies.[18] Especially in the case of the first diffraction order appearing parallel to the surface at glancing angle, anomalies in the measured spectra can be found. According to Stewart and Gallaway,[18] the corresponding "Rayleigh" wavelengths can be found in the zero–order specular radiation yielding:

$$\lambda_R(\theta_{\text{in}}) = \frac{\Lambda}{m_\pm}\left(\pm 1 - \sin\theta_{\text{in}}\right). \tag{2}$$

At the Rayleigh wavelengths first order emerges at glancing angle and the redistribution of energy results in a anomaly in the specular reflection. Anomalies have been subject to an intense study. Hessel and Oliner[19] argue that two distinct types of anomalies may exist: A Rayleigh wavelength type due to the emergence of a new

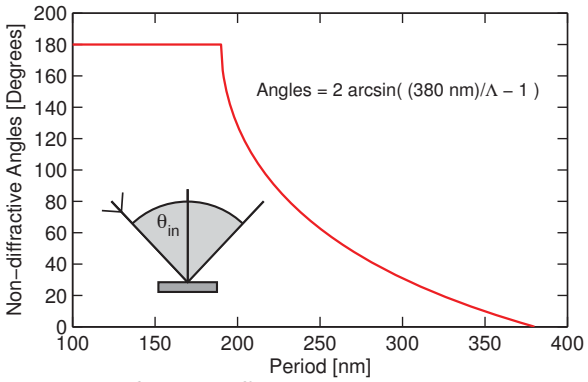

Figure 2: Incident angles causing no reflected diffraction in the visual spectrum as function of nanostructure period. Periods below 190 nm does not lead to diffraction at any angles in the visual spectrum.

spectral order at grazing angle, and a resonance type which is related to the guided complex waves supportable by the grating.

To complete the picture of optical gratings, we also discuss, sub-wavelength, non-diffractive gratings using an argument given by Raguin and Morris.[17] For non-diffractive gratings the period should be small enough that all higher diffraction orders are evanescent. From the grating equation, this requirement sets an upper limit to the period-to-wavelength ratio specified by [17, Eq. (2)]; $\frac{\Lambda}{\lambda} < \frac{1}{\max(n_2,n_1)+n_1 \sin\theta_{\max}}$, where $\theta_{\max}$ is the maximum angle of incidence. Since the denominator of the right-hand side of the above inequality is always larger than unity because $n_1 \geq 1$ and $n_2 \geq 1$, it is seen that the surface must always have a surface period smaller than the dimensions of the incident wavelength, hence the term sub-wavelength. It should be noted that the above argument is normally only given in terms of the reflected orders, leading to an intermediate range of structures that are often anti-reflective, but still scatters light in the transmission. In the case of a period of 250 nm, the first order reflection appears at glazing angle (horizontal along the interface) at 31 degrees incidence, meaning that the perceived specular color is significantly changed for angles bigger than 31 degrees incidence. Therefore, the non-diffractive angle interval is 62 degrees, as seen in Fig. 2. For a period of 200 nm, first order reflection does not occur until 76 degrees. Periodic structures below 250 nm provides basis for angle-independent colors, although diffractions can be seen for angles approaching glazing angle. For structural color effects, the optimum is periods approximately 200 nm in order to avoid diffraction in the visual spectrum. Periods below 190 nm do not lead to diffraction at any angles in the visual spectrum, as seen in Fig. 2, however transmission diffraction effects may still affect the specular reflection.

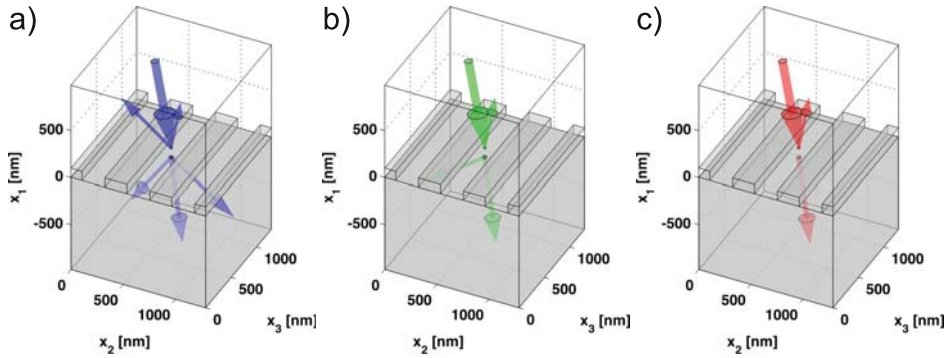

Figure 3: RCWA simulations illustrating the three fundamental grating regimes using 430 nm period, 100 nm height, 10° incident light and $n_2 = 1.4$. Arrows indicate magnitude on logarithmic scale. a) $\lambda = 410$ m (blue light). Several orders in both transmission and reflection. b) $\lambda = 550$ nm (green light). 0'th order in reflection, two orders in transmission. c) $\lambda = 680$ nm (red light). Only 0'th order in both reflection and transmission.

As illustrated in Fig. 3 three optical regimes can be distinguished: 1) For short wavelengths, several orders in both the transmission and reflection exist, 2) for wavelengths longer than the period, only the zero–order in reflection but still several orders in transmission exist, and finally, 3) for long wavelengths only zero–order in both reflection and transmission exist. These three optical regimes are fundamental to the reflection and transmission of optical gratings.

3. ANTIREFLECTIVE STRUCTURES

Anti-reflective coatings, as widely applied in many optical components, is conventionally realized by adding one or more layers of dielectric or metallic thin films on the surface. It is widely known that a single layer can reduce the reflectance of a glass surface to a mean value of approximately 2.5% in the visible spectrum. Multi-layer coatings, typically with 3-6 layers can reduce the reflectance to below 0.5% in the visible spectrum. At 45° incident angle the reflectance of such a coating is approximately 1%.

Antireflective properties can also be obtained by structuring the surface on the nanoscale. In the sub-wavelength regime, light cannot resolve the individual features of the surface. The structures function as a gradient in the effective refractive index of the material, reducing Fresnel reflections from the surface.[1,4] Antireflective structures can be realized in different ways. It can be random structures or periodic structures in one or more dimensions. For fabrication of such such nano-texture by casting or molding, the master structures can be fabricated in a range of different ways. Random textures have been fabricated by anodized aluminium oxide[20] and by so-called black silicon,[7,21] whereas periodic textures have been realized by interference lithography[4] and electron-beam lithography.[6]

In 2008 Ting *et al.* reported antireflective structures in PMMA, fabricated by hot embossing with a Ni-Co stamp.[22] The high aspect ratio structures were fabricated in Si using electron cyclon resonance (ECR) etching, and the Ni-Co shim was subsequently electroplated from the Si master. They report reflectances below 0.5% in the visible spectrum for structures with aspect ratio higher than 2.6. In 2010 Hong *et al.* reported the fabrication of antireflective nanostructures in COC by hot embossing from a black silicon master. After hot embossing, the master was dissolved as it was not possible to release it from the imprinted COC. the transmittance of COC was increased from 90% to 95% by nanostructuring both sides of the COC film. The aspect ratio of the structures was up to 12, and the tip of the structures was below 20 nm. Jang *et al.* reported laser interference patterns in Si hot embossed in polycarbonate. Transmittance increased from 90% to 93.5% (single side)[23] and drops in transmittance are observed when diffraction occurs for small wavelengths. For example, a grating with a period of 227 nm has a cutoff wavelength around 375 nm, whereas a 300 nm period yields a cutoff wavelength of approximately 475 nm.

The black silicon method[24] has been chosen for this study. This is a cheap and fast method to cover large areas with random conical-shape nanostructures. For comparison, the price-per-area for e-beam exposed masters can be four orders of magnitude higher. Black silicon etching is a mask less reactive ion etching (RIE) process, which can form large areas of random tapered nanostructures. Black silicon etches can be performed in many different ways. The simplest one uses just SF_6 and O_2.[25] SF_6 supplies the fluorine atoms that react with silicon to make a volatile SiF_4 gas. The oxygen reacts with fluorine and silicon to make a passivating layer of $Si_xF_yO_z$. Any protrusion that will exist or is formed on the surface will be slightly more protected by the passivation layer compared to the planar regions of the surface. As the etching continues, any roughness will be enhanced

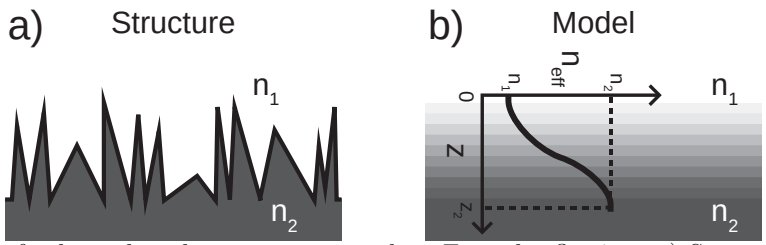

Figure 4: Illustration of subwavelength structures to reduce Fresnel reflection. a) Structure. b) Modeling by a gradient in the effective refractive index of the material.

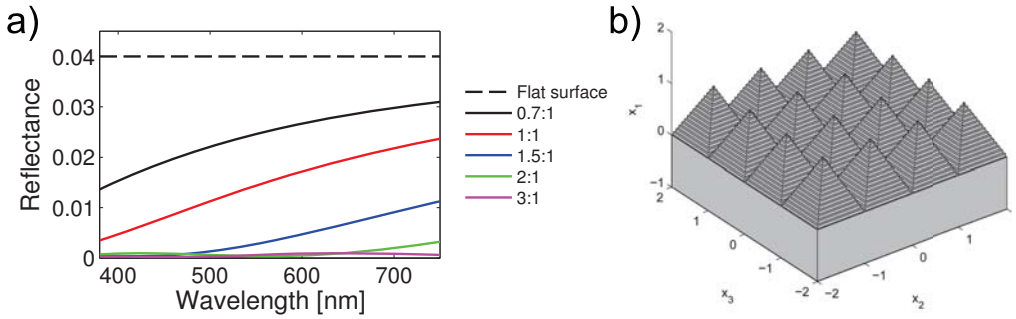

Figure 5: Reflectance of pyramid texture as function of wavelength for various aspect ratios. a) Calculation by 100 layers with transfer matrix approach and effective medium theory. b) Schematic of modelled structure.

and eventually form cone or needle-like structures. The surfaces formed by this method are statistical in nature due to the random formation process. Thus it is not a lithography method. However, by controlling the critical etching parameters[7] such as pressure, platen power, gas flows and temperature, the average lateral sizes and aspect ratios of the structures can be tuned. The black silicon can then be used as a master, for replication in polymer by hot embossing or by UV nano-imprint lithography (UV-NIL).

The antireflective effect can be described by dividing the structured region of the surface in thin layers of increasing refractive index. Instead of a single interface, the surface now consist of a multiple of interfaces, each with a small increment in the refractive index, see Fig. 4. Due to the non-linear dependence on the refractive index of the Fresnel coeffients, the total reflectance from such a system will be smaller than that of a single interface. From this model, the reflectance of a polymer surface can be calculated, using the transfer matrix method.[26] The refractive index of each of the layers can be described from the geometry of the structures, and an effective medium theory. The result of such a model is given in Fig. 5, for a surface with pyramid shaped structures. It is seen that by increasing the height of the structures, the reflectance can effectively be reduced to zero. However, large-aspect-ratio structures can be challenging to fabricate. Thus, significant anti-reflective effect is seen for structures with an aspect ratio of only 1.5:1.

The random nanostructures will inherently scatter light. This is a drawback for our applications. If the structures are too large, they will scatter light in the visible spectrum, rendering the surface of an otherwise clear polymer milky white. As shown by the authors,[27] the scattering properties of black silicon can be tailored to function as color filters in directly transmitted light. Furthermore, the scattering from the randomly textured black silicon can be minimized, as reported by the authors.[21] By controlling the black silicon etching process, the characteristic lateral spatial frequency of the nanostructures can be maximized to minimize scattering. An example of such a surface is shown in Fig. 6. The sample is fabricated using black silicon as a master for a UV-NIL process, using the UV curable resin, Ormocomp (a transparent organic-inorganic hybrid polymer from

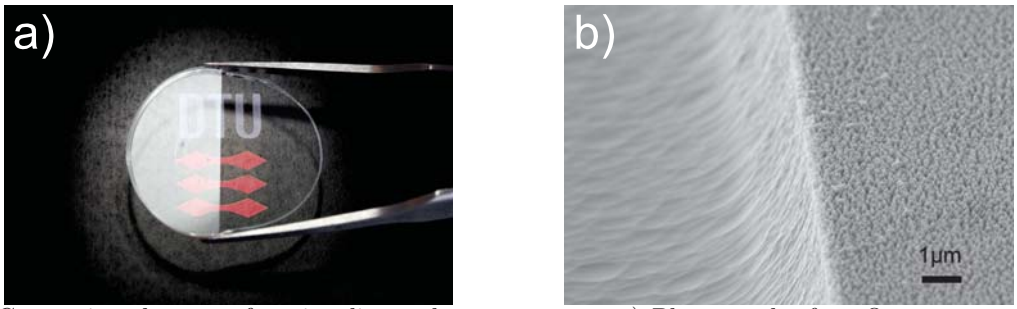

Figure 6: Comparison between functionality and nano-texture. a) Photograph of an Ormocomp sample with antireflective functionality of the nanostructures fabricated by UV-NIL, using black silicon as a master (right part of sample), compared to a non-textured surface (left part of sample). b) SEM image of the interface between the nano-textured and non-textured surface.

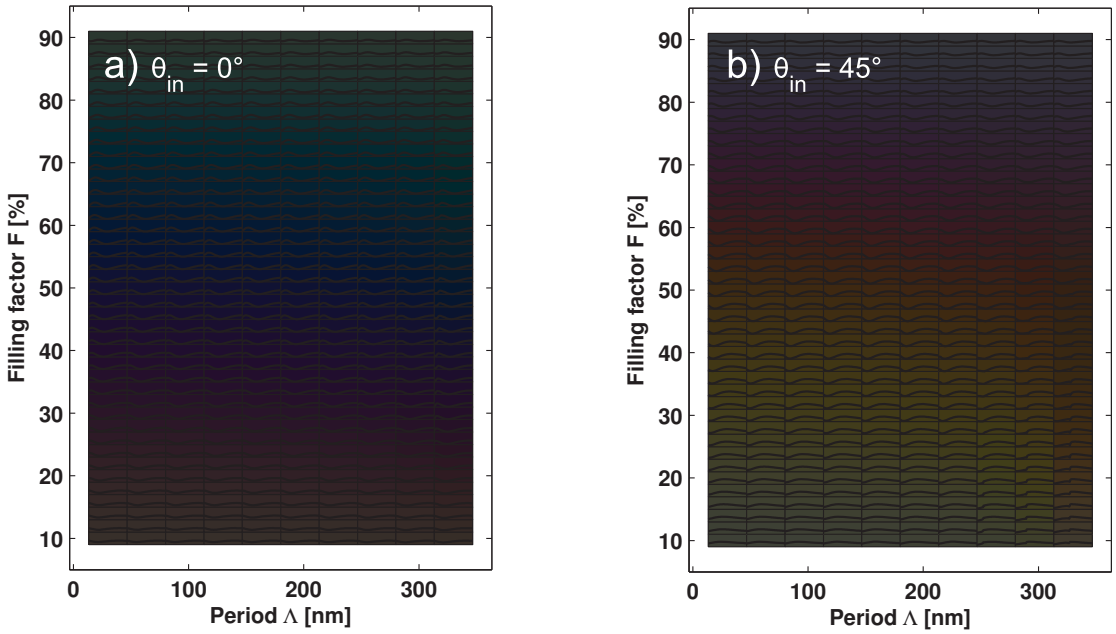

Figure 7: Example of plastic (n=1.5) surface daylight color effects based on a square lattice. a) Normal incidence. b) 45° incidence. Each square shows RCWA simulated specular colors for given parameters.

Micro resist technology Gmbh, Berlin). The left side of the sample is a planar Ormocomp surface on both front and backside, whereas the right side is nanostructured on both front and back. The sample is placed on a paper with a DTU logo printed on a black background and illuminated by a white light source for specular reflection into the camera. It is clearly seen that the nanostructured surface suppress a large part of the specularly reflected light. The nanostructures reduce Fresnel reflection by 50%, even though they only have an aspect ratio of 1.3. The structures are 200 nm tall, and have a characteristic distance between each nanostructure of 160 nm correpsonding to a lateral spatialt frequency of 6 μm^{-1}.

4. ANGLE-INDEPENDENT STRUCTURAL COLORS

Structural colors can originate from nano-textured surfaces. As a first approach to address the strong angular-dependence of diffraction grating based structural color, we discuss the possibilties of strucutral color in the case of polymer surfaces from sub-wavelength diffraction gratings. The grating scattering properties are studied by RCWA,[28] using a commercial solver (GD-Calc, KJ Innovation) for simulating the absolute values of reflection and transmission. Due to the dependence on the exact structural dimensions, each point in the $(\theta_{\mathrm{in}}, \phi_{\mathrm{in}}, \lambda)$ parameter space must be individually assessed for given structural dimensions.

For background, the color of an object is the result of a complex interaction between the light source $S(\lambda)$ incident on the object, the reflection or transmission of the object $R(\lambda)$ or $T(\lambda)$, and the observer modeling the spectral sensitivity of human perception. In the CIE 1931 XYZ-model,[29] colors can be defined on integral form:

$$\begin{bmatrix} X \\ Y \\ Z \end{bmatrix} \equiv C^{-1} \int_0^{\infty} S(\lambda)\, R(\lambda) \begin{bmatrix} \bar{x}_{\mathrm{obs}}(\lambda) \\ \bar{y}_{\mathrm{obs}}(\lambda) \\ \bar{z}_{\mathrm{obs}}(\lambda) \end{bmatrix} \mathrm{d}\lambda, \tag{3}$$

with normalization $C \equiv \int_0^{\infty} S(\lambda)\, \bar{y}_{\mathrm{obs}}(\lambda)\, \mathrm{d}\lambda$. The parameters $(\bar{x}_{\mathrm{obs}}, \bar{y}_{obs}, \bar{z}_{obs})$ describe the spectral sensitivity of the observer and roughly correspond to the sensitivity of the three cones (fovea centralis) of the human eye. Here, we use the 1978 Judd Vos correction[30] of the CIE 1931 2° observer[29] and the ISO/CIE standard illuminant D65.[31] In order to accurately present color values, a conversion between the device-independent CIE-XYZ model

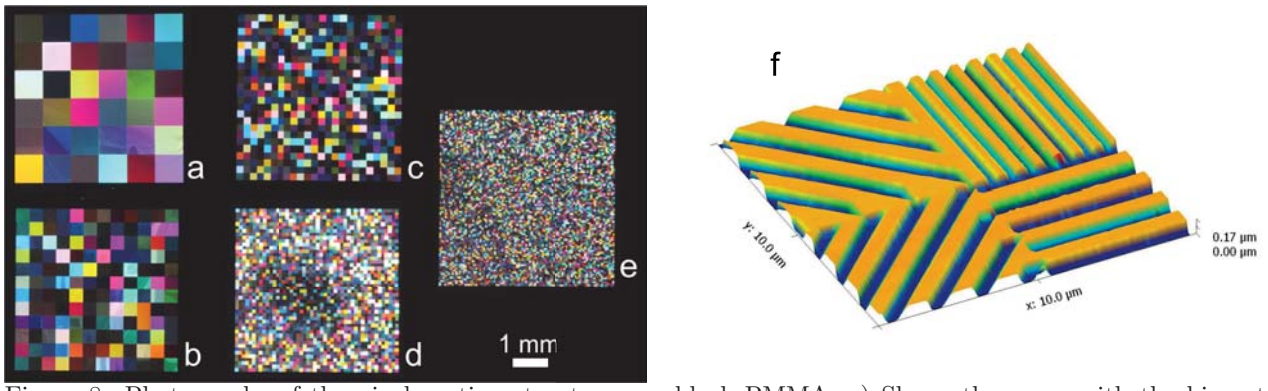

Figure 8: Photographs of the pixel grating structures on black PMMA. a) Shows the array with the biggest pixels, 800 micron. b) 400 micron. c) 200 micron. d) 100 micron. e) Down to 50 micron, barely resolvable with the human eye. f) AFM image of the Si master, showing an intersection between four different pixels. The different orientations and periods of the diffraction gratings give rise to the pseudo angle-independent color effect.

and device-dependent outputs on a display (voltages expressed in RGB) or paper (CMYK) is needed. Here we adopt the sRGB conversion for display.[32]

Given the fabrication platform developed, what possible colors may be produced? An answer to that question is given by the color map in Fig. 7 for normal incidence and 45° incidence. The map is constructed by simulating the reflection of squared two-dimensional silicon gratings converted into a color via Eq. (3). The colors may appear darker due to the overlaying reflection spectra data.

From the figures, it is seems that bright angle in-dependent color effects in polymer material by sub-wavelength diffraction gratings are challeging. The results confirm the basic observation that the total reflectance cannot exceed the Fresnel reflection of the corresponding planar surface.

5. ANGLE-DEPENDENT COLOR EFFECTS BY DIFFRACTION GRATING PIXELS

Even though the reflectance of polymers is low, diffraction gratings can provide bright reflected angular dependent color effects on a black polymer substrate by diffracting light into several beams traveling in different directions. Despite the angular-dependent nature of diffraction, it is possible to obtain what we will refer to as an pseudo-angular independent color effect. This can be achieved by combining multiple gratings of different types in a pixel-array. Each pixel, consisting of a single grating, will be highly angle-dependent, however the overall glitter effect of the entire array will appear homogeneous and independent of viewing angle as a second approach to adress angle-dependence.

The individual gratings are chosen to be one-dimensional line gratings. A 2D-grating would provide more diffraction orders, thereby increasing the chance of an order being seen by the observer, but the individual orders would also be significantly weaker. By choosing 1D gratings there will be fewer orders, but the ones existing will be much stronger. The period of a grating determines the direction of the diffraction orders for light with a given incident angle. Here we use 8 different periods ranging from 700 nm to 1400 nm with 100 nm spacing in a uni-form distribution. This interval is chosen to provide orders for large intervals of solid angles, while still maintaining bright individual orders. To even out the azimuthal angle dependence, the gratings are oriented in four different directions. The height and filling factor are chosen to maximize the diffraction efficiency for a wide range of wavelengths and incident angles. Based on RCWA simulations, it is found that a height of 135 nm and a filling factor of 50 % leads to a optimum of diffraction efficiency, with respect to incident angle and wavelength.

The diffraction gratings were defined using electron beam lithography on a silicon wafer. The structures were transfered to a black PMMA substrate, using hot embossing. An AFM image of the fabricated master is shown in Fig. 8f, where four different pixels can be seen. The fabricated PMMA sample was photographed using a digital single-lens reflex camera with a Canon MP-E 65mm f/2.8 1-5x Macro lens, and a white light source. The

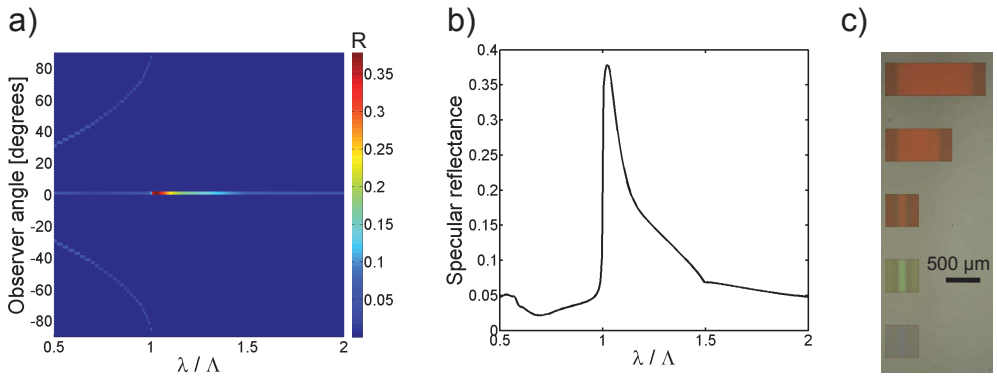

Figure 9: Calculated reflectance values for a thick foil with a grating on the front illuminated at normal incidence. a) Reflectance for a given wavelength and observer angle. For the given wavelength interval 0'th order as well as $\pm$ 1'st order are present b) The 0'th order reflectance showing a large peak just above $\lambda/\Lambda = 1$. c) Microscope image of gratings with three different periods leading to three different colors.

photographs, seen in Fig. 8, were taken directly above the sample, with the light source directed at the sample from the side. The lens can resolve features not visible to the human eye. The 50 micron pixels, for example, are easily seen in the photo with the help of the lens. Each array is 4.8×4.8 mm^2, (a) is the 800 micron pixels, (b) 400 micron; halved each time, down to (e) with 50 microns.

6. DIFFRACTION GRATINGS ON THICK TRANSPARENT FOILS

Until this point the nano-textured polymer surface has been considered as an isolated system with the reflectance of the surface being the only contribution to the observed color. This is for example the case for a black pigmented polymer, where practically all light entering the polymer is absorbed. As a third apporach to overcome angular dependence, we now discuss the inclusion of backside reflections.

Angle-independent color effects can be achieved with a reflectance exceeding the corresponding planar Fresnel surface reflectance, for example in the case of a thick transparent foil. A thick foil can be defined as a slab of material with parallel front and back sides and with a thickness larger than the coherence length of the light under consideration. This implies no interference between reflections on the front and back. Therefore all surface effect calculations can be treated separately using RCWA and Fresnel coefficients for diffraction gratings and flat surfaces respectively.

The system under consideration is a transparent foil, of refractive index n_2, with a diffraction grating of period Λ on the top side. The foil is illuminated by white light at normal incidence. The back side is flat. With the given constraints, it is straight forward to set up a calculation of the efficiency of the reflected and transmitted orders of the full system using ray tracing. First, the incoming light interacts with the grating in the top surface producing both transmitted and reflected orders, of which the efficiencies may be calculated using RCWA. The transmitted orders propagate to the back side where they partly escape into the air and partly reflect back into the substrate. The reflected light from the back will again approach the front surface, now from the inside and it is again reflected and transmitted based to the grating geometry. By tracing all orders the total reflectance and transmittance can be found by summation of the escaped light.

Such a calculation has been made for a binary line grating of which both the protrusion height and width equals half the period. The reflectance as function of wavelength and observer angle is seen in Fig. 9a. The zero'th order reflection is located at 0 degrees, whereas the ± 1 orders are present for wavelengths smaller than the period at varying angles according to the diffraction equation.

In Fig. 9b the 0 order reflectance is seen. Most noticeable is a large peak for wavelengths just higher than the period, reaching a level almost 10 times the Fresnel reflection of a flat surface. At the same time the peak is relatively sharp enabling bright colors to be produced. Three examples of such colors are seen in Fig. 9c, where

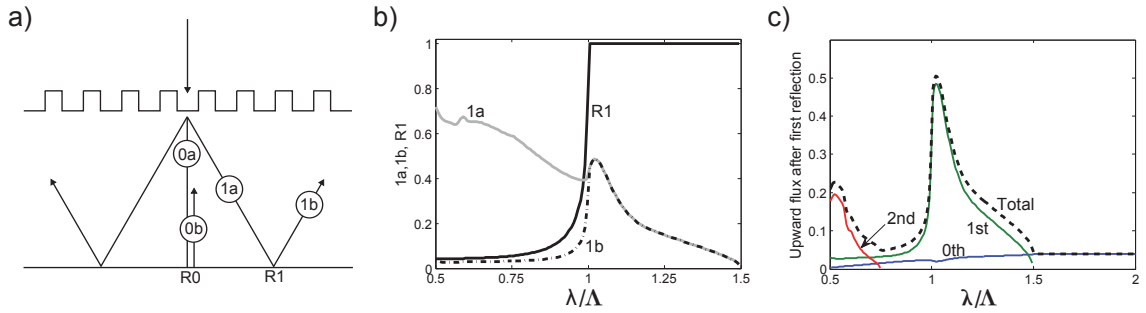

Figure 10: a) Illustration of different orders relevant for the creation of the sharp reflectance peak. b) The 1st order fluxes before (1a) and after (1b) reflection on the back side as well as back side reflectance, R1. c) Contributions to the upwards flux after one reflection on the back.

a 0.1 mm thick topas foil with imprinted gratings of periods 425 nm (blue), 505 nm (green), and 615 nm (red) is seen trough a bright field microscope. The gratings, which are here 350 nm deep, were originally fabricated in a silicon master using e-beam lithography and dry etching and then replicated in the foil using thermal imprint.

The strong peak in the zero'th order reflection is based on total internal reflection on the backside of the transmitted orders of the first interaction with the grating. For wavelengths satisfying $\Lambda < \lambda < n_2\Lambda$ the foil will support three orders (-1,0, and 1) while the air will only support one. This leads to total internal reflection of the ± 1 orders on the backside of the foil. For wavelength satisfying $\lambda < \Lambda$ there exists more orders in the air which the ± 1 can couple to, thereby lowering the Fresnel reflection on the backside. The process producing the strong peak is illustrated in Fig. 11, where the strengths of the first order fluxes are shown after the initial interaction with the grating (1a) and after reflection at the back side (1b). The Fresnel reflectance of the first orders on the back is also shown.

It is clear that two conditions must be fulfilled in order to get high strength of upwards going fluxes. The ± 1 order efficiency must be high and it should be totally reflected on the back. These conditions are only fulfilled for wavelengths just above the period leading to the significant peak. In Fig. 11c are the contributions to the total upwards flux after one reflection on the back shown. Here it is clear that the ± 1 orders are responsible for the existence of the peak.

With the knowledge that the color information is lying in the total internally reflected first order fluxes (1b) it is possible to create a structure which facilitates a diffuse colored reflection upon normal incident light, rather than having the color information only in the specular direction. The principle is illustrated in Fig. 11a. The

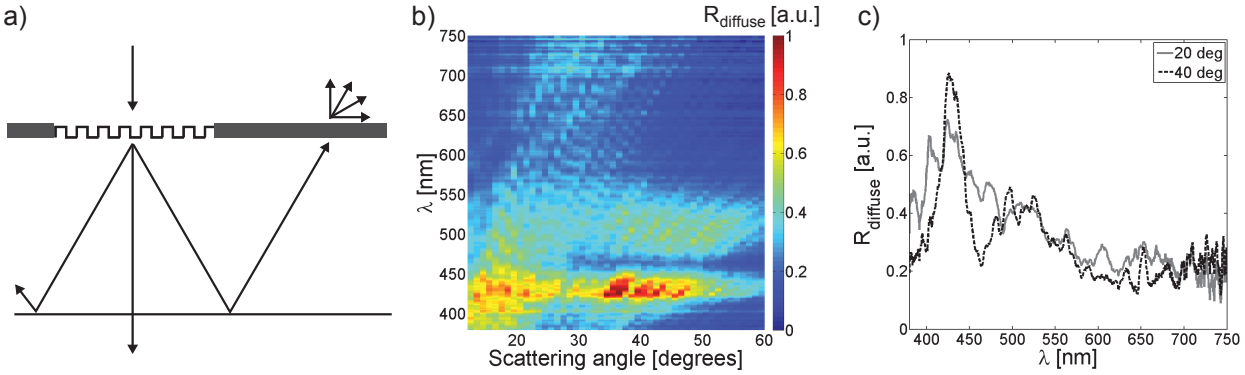

Figure 11: a) Conceptual sketch of alternating grating and diffuser sections. b) Angle resolved measurement of diffuse reflectance from gratings with period 405 nm for normal incident light is used c) Spectra at 20 and 40 degrees observer positions.

surface of the foil is covered by alternating sections of grating and diffuser elements. The diffuser elements, which enables the out coupling of the first order modes in various directions, could be fabricated in several ways. Refractive elements, such as micro lens arrays are effective diffusers,[33] but the structure size of the lenses is not compatible with the design used her. Instead random binary diffusers[34] are used. In this ways the periodic gratings and diffusers may be fabricated in the same fabrication step. The widths of the sections are designed such that all total internal reflected first orders of the peak wavelength hits a diffuser.

Angle resolved measurement of the diffuse reflection for such a surface with a grating period of 405 nm is seen in Fig. 11b. A clear enhancement of the blue light in a wide angle interval is observed as also illustrated by the spectra at 20 and 40 degrees in Fig. 11c. The spectra somewhat noisy character of the spectra originates from the diffractive nature of the diffusers.

ACKNOWLEDGMENTS

We acknowledge J. Scheel, DTU Nanotech, for photography. J. Weirch, Danish Fundamental Metrology, and J. Nørregaard, NIL Technology Aps, are acknowledghed for fruitfull discusions. This work was supported by the Danish National Advanced Technology Foundation (Contract No.: 007-2010-2) and by the European Commision via the FP7 MMP Integrated project PLAST4FUTURE (NMP2-SE-2012-314345).

REFERENCES

[1] Bernhard, C. G., "Structural and functional adaptation in a visual system," *Endeavour* , 79–84 (1967).

[2] Parker, A. R. and Townley, H. E., "Biomimetics of photonic nanostructures," *Nature Nanotechnology* **2**, 347–353 (June 2007).

[3] Vukusic, P., Sambles, J. R., and Lawrence, C. R., "Colour mixing in wing scales of a butterfly," *Nature* **404**, 457 (Mar. 2000).

[4] Clapham, P. B. and Hutley, M. C., "Reduction of Lens Reflexion," *Nature* **244**(281) (1973).

[5] Stephens, R. B. and Cody, G. D., "Optical Reflectance and transmission of a textured surface," *Thin Solid Films* **45**, 19–29 (1977).

[6] Kanamori, Y., Sasaki, M., and Hane, K., "Broadband antireflection gratings fabricated upon silicon substrates," *Optics Letters* **24** (Oct. 1999).

[7] Sainiemi, L., Jokinen, V., Shah, A., Shpak, M., Aura, S., Suvanto, P., and Franssila, S., "Non-reflecting silicon and polymer surfaces by plasma etching and replication.," *Advanced materials* **23**, 122–6 (Jan. 2011).

[8] Park, K.-C., Choi, H. J., Chang, C.-H., Cohen, R. E., McKinley, G. H., and Barbastathis, G., "Nanotextured Silica Surfaces with Robust Superhydrophobicity and Omnidirectional Broadband," *ACS Nano* **6**(5), 3789–3799 (2012).

[9] Kinoshita, S., Yoshioka, S., and Miyazaki, J., "Physics of structural colors," *Rep. Prog. Phys.* **71**, 1 (Jan. 2008).

[10] Chung, K., Yu, S., Heo, C.-J., Shim, J. W., Yang, S.-M., Han, M. G., Lee, H.-S., Jin, Y., Lee, S. Y., Park, N., and Shin, J. H., "Flexible, Angle-Independent, Structural Color Reflectors Inspired by Morpho Butterfly Wings," *Advanced Materials* **24**, 2375–2379 (2012).

[11] Ribot, C., Lee, M.-S. L., Collin, S., Bansropun, S., Plouhinec, P., Thenot, D., Cassette, S., Loiseaux, B., and Lalanne, P., "Broadband and Efficient Diffraction," *Advanced Optical Materials* , n/a–n/a (July 2013).

[12] Cao, L., Fan, P., Barnard, E. S., Brown, A. M., and Brongersma, M. L., "Tuning the color of silicon nanostructures.," *Nano letters* **10**, 2649–54 (July 2010).

[13] Walia, J., Dhindsa, N., Khorasaninejad, M., and Saini, S. S., "Color Generation and Refractive Index Sensing Using Diffraction from 2D Silicon Nanowire Arrays.," *Small (Weinheim an der Bergstrasse, Germany)* , 1–8 (June 2013).

[14] Vukusic, P. and Sambles, J. R., "Photonic structures in biology," *Nature* **424**, 852 (Aug. 2003).

[15] Prum, R. O., Quinn, T., and Torres, R. H., "Anatomically diverse butterfly scales all produce structural colours by coherent scattering.," *The Journal of experimental biology* **209**, 748–65 (Mar. 2006).

[16] Bao, G., Dobson, D. C., and Ramdani, K., "A constraint on the maximum reflectance of rapidly oscillating dielectric gratings," *SIAM J. Control Optim.* **40**, 1858–1866 (Mar. 2002).

[17] Raguin, D. H. and Morris, G. M., "Analysis of antireflection-structured surfaces with continuous one-dimensional surface profiles," *Appl. Optics* **32**, 2582 (May 1993).
[18] Stewart, J. E. and Gallaway, W. S., "Diffraction Anomalies in Grating Spectrophotometers," *Appl. Optics* **1**, 421 (July 1962).
[19] Hessel, A. and Oliner, A. A., "A New Theory of Wood's Anomalies on Optical Gratings," *Appl. Optics* **4**(10), 1275 (1965).
[20] Deniz, H., Khudiyev, T., Buyukserin, F., and Bayindir, M., "Room temperature large-area nanoimprinting for broadband biomimetic antireflection surfaces," *Applied Physics Letters* **99**(18), 183107 (2011).
[21] Christiansen, A. B., Clausen, J., Mortensen, N. A., and Kristensen, A., "Minimizing scattering from antireflective surfaces replicated from low-aspect-ratio black silicon," *Applied Physics Letters* **101**(13), 131902 (2012).
[22] Ting, C.-J., Huang, M.-C., Tsai, H.-Y., Chou, C.-P., and Fu, C.-C., "Low cost fabrication of the large-area anti-reflection films from polymer by nanoimprint/hot-embossing technology.," *Nanotechnology* **19**, 205301 (May 2008).
[23] Jang, H. S., Kim, J. H., Kim, K. S., Jung, G. Y., Lee, J. J., and Kim, G. H., "Improvement of Transmittance by Fabricating Broadband Subwavelength Anti-Reflection Structures for Polycarbonate," *Journal of Nanoscience and Nanotechnology* **11**, 291–295 (Jan. 2011).
[24] Jansen, H., Boer, M. D., Legtenberg, R., and Elwenspoek, M., "The black silicon method: a universal method for determining the parameter setting of a fluorine-based reactive ion etcher in deep silicon trench etching with profile control," *Journal of Micromechanics and Microengineering* **5**, 115–120 (June 1995).
[25] Kumaravelu, G., Alkaisi, M. M., and Bittar, A., "Surface texturing for silicon solar cells using reactive ion etching technique," *Conference Record of the Twenty-Ninth IEEE Photovoltaic Specialists Conference* , 258–261 (2002).
[26] Pedrotti, F. L., Pedrotti, L. S., and Pedrotti, L. M., [*Introduction to Optics*], Pearson Prentice Hall, third ed. (2007).
[27] Clausen, J., Christiansen, A. B., Garnaes, J., Mortensen, N. A., and Kristensen, A., "Color effects from scattering on random surface structures in dielectrics.," *Optics express* **20**, 4376–81 (Feb. 2012).
[28] Nevière, M. N. and Popov, M. N. E., [*Light Propagation in Periodic Media: Differential Theory and Design*], Optical Engineering Series, Marcel Dekker, Inc. New York (2003).
[29] Smith, T. and Guild, J., "The C.I.E. colorimetric standards and their use," *Trans. Opt. Soc.* **33**(3), 73.
[30] Vos, J. J., "Colorimetric and photometric properties of a 2-deg fundamental observer," *Color Res. Appl.* **3**, 125–128 (1978).
[31] Judd, D. B., Macadam, D. L., Wyszecki, G., Budde, H. W., Condit, H. R., Henderson, S. T., and Simonds, J. L., "Spectral Distribution of Typical Daylight as a Function of Correlated Color Temperature," *J. Opt. Soc. Am.* **54**(8), 1031 (1964).
[32] Stokes, M., Anderson, M., Chandrasekar, S., and Motta, R., "A Standard Default Color Space for the Internet - sRGB http://www.w3.org/Graphics/Color/sRGB.html (checked 2012-04-20)," (1995).
[33] Chang, S.-I., Yoon, J.-B., Kim, H., Kim, J.-J., Lee, B.-K., and Shin, D. H., "Microlens array diffuser for a light-emitting diode backlight system," *Optics letters* **31**, 3016–8 (Oct. 2006).
[34] Kurtz, C. N., "Transmittance Characteristics of Surface Diffusers and the Design of Nearly Band-Limited Binary Diffusers*," *JOSA* **62**(8), 982–989 (1972).